

ENTANGLED MANY-BODY STATES
AS RESOURCES OF
QUANTUM INFORMATION
PROCESSING

LI YING

A THESIS SUBMITTED FOR THE
DEGREE OF DOCTOR OF PHILOSOPHY

CENTRE FOR QUANTUM TECHNOLOGIES
NATIONAL UNIVERSITY OF SINGAPORE

2013

DECLARATION

I hereby declare that the thesis is my original work and it has been written by me in its entirety. I have duly acknowledged all the sources of information which have been used in the thesis.

This thesis has also not been submitted for any degree in any university previously.

A handwritten signature in black ink, appearing to read 'liyong', written in a cursive style.

LI YING

23 July 2013

Acknowledgments

I am very grateful to have spent about four years at CQT working with Leong Chuan Kwek. He always brings me new ideas in science and has helped me to establish good collaborative relationships with other scientists. Kwek helped me a lot in my life. I am also very grateful to Simon C. Benjamin. He showed me how to do high quality researches in physics. Simon also helped me to improve my writing and presentation. I hope to have fruitful collaborations in the near future with Kwek and Simon.

For my project about the ground-code MBQC (Chapter 2), I am thankful to Tzu-Chieh Wei, Daniel E. Browne and Robert Raussendorf. In one afternoon, Tzu-Chieh showed me the idea of his recent paper in this topic in the quantum cafe, which encouraged me to think about the ground-code MBQC. Dan and Robert have a high level of comprehension on the subject of the MBQC. And we had some very interesting discussions and communications.

I am grateful to Sean D. Barrett, Thomas M. Stace for their work on my projects of the distributed QIP (Chapter 3 and Chapter 5). Tom showed me how to do error corrections on the surface code when he was visiting CQT. It is a very helpful discussion, and I am still benefiting from that discussion recently. Sean generously shared his code of simulating the surface code error correction with me. It is a very powerful code. I have used his code in my previous three projections (Chapter 4, Chapter 5 and Chapter 6).

I am especially grateful to Leandro Aolita for his great and hard work on my projects on the subject of quantum optics (Chapter 7 and Chapter 8). In my first project in CQT (Chapter 7), we began to work together. After that, we have been in communication and exchange ideas, but somehow we did not have further collaborations until the last year of my Ph.D., when

we have a chance to work together on two more very interesting projects, in which one is presented in this thesis (Chapter 8), while the other, an experimental project is still in progress. I enjoyed working together with Leandro. And I hope that we can have more future collaborations.

For my project about the quantum network (Chapter 6), I am grateful to Daniel Cavalcanti. I am also grateful to Alexia Auffèves, Daniel Valente and Marcelo Franca Santos for their work on my projects about one-dimensional atoms, which are not presented in this thesis. I would like to thank Professor Kerson Huang. We had some very funny discussions at the beginning of my Ph.D., and I appreciate his sharpness. He has made physics more interesting for me.

I give special thanks to Professor Zhi Song. He hosted my visiting in Nankai university. I thank Hu Wenhui and Jin Liang, who helped me a lot during my visiting in Nankai.

During my Ph.D., I received help from many people in CQT. I would like to thank Tan Hui Min Evon and Lim Jeanbean Ethan. I also have to thank people who clean the quantum cafe and my office.

Finally, I would like to thank my parents and especially my wife, Mingxia, for her unconditional help and sacrifice during my graduate studies. I must thank my daughter, Daiyao, who is born on the second year of my Ph.D. She brings me a lot of good luck.

Contents

Acknowledgments	i
Table of Contents	iii
Summary	vii
List of Publications	ix
1 Introduction	1
2 Thermal States as Universal Resources for Quantum Computation with Always-on Interactions	7
2.1 Introduction	7
2.2 Cluster states	9
2.3 Topological fault-tolerance quantum computation	11
2.4 Measurement-based quantum computing	15
2.5 2D System	16
2.5.1 Ground state and energy gap	18
2.5.2 POVM and GHZ state	18
2.5.3 Cluster state and universality of the ground state	19
2.6 3D system and topologically protected cluster state	20
2.7 Thermal computational errors and error correction	22
2.7.1 Errors on GHZ states	23
2.7.2 Measurements on bond particles	26
2.7.3 Erroneous operators on the cluster state	27
2.7.4 Error correction	28
2.8 MBQC with always-on interactions	30

3 Fully fault tolerant quantum computation with non-deterministic gates	33
3.1 Introduction	33
3.2 Non-deterministic entangling operations	38
3.3 Growth of cluster states	42
3.4 Error model	49
3.5 Error propagation	50
3.6 Error accumulation	51
3.7 Final errors on the topologically protected cluster state . . .	53
3.8 Error correction	55
3.9 Phase diagrams of error correction	57
 4 High threshold distributed quantum computing with three-qubit nodes	 61
4.1 Introduction	61
4.2 The states of the art	63
4.3 A review of broker schemes - remote entangling operations on client qubits	65
4.3.1 Effective control-phase gates	67
4.3.2 Effective parity projections	68
4.4 Overview of full noise purification with DQC-3	69
4.5 Purifying the parity projection operation	70
4.6 Building the TPC state within the constraints of DQC-3 . .	74
4.7 Results	76
 5 Long range failure-tolerant entanglement distribution	 79
5.1 Introduction	79
5.2 The scheme	81

Contents

5.3	Cluster state growth	84
5.4	Noise, Imperfections and Error Correction	90
5.5	Performance	94
6	Two dimensional scalable quantum network with general noise	97
6.1	Introduction	97
6.2	Scheme	98
6.3	Error thresholds	104
6.4	Final remote entangled state	105
6.5	Efficiency	107
7	Photonic multiqubit entangled states from a single atom	109
7.1	Introduction	109
7.2	The protocol	111
7.2.1	GHZ and linear cluster states	113
7.3	Implementation with ^{40}Ca	114
7.4	Implementation with ^{87}Rb	116
7.5	Technical details	119
7.6	Feasibility	121
7.7	Efficiencies and fidelities	122
8	Robust-fidelity atom-photon entangling gates in the weak-coupling regime	125
8.1	Introduction	125
8.2	Photons scattering off two-level emitters in 1D	128
8.3	High-fidelity interaction from imperfect processes	131
8.4	Entangling gate for time-bin flying qubits	132
8.5	Entangling gate for polarization flying qubits	133

8.6 Single-emitter quantum memories and sequential measurement-based quantum computations	135
8.7 Feasibility	136
8.8 Heralded losses versus infidelities	137
9 Conclusions and Outlook	139
Bibliography	145

Summary

In this thesis we theoretically discuss some proposals of quantum information processing without precise manipulations of interactions over a large number of qubits. Firstly, we study the measurement-based quantum computation utilizing single-particle operations on the thermal state of a model spin Hamiltonian with always-on interactions. We find computational errors induced by thermal fluctuations can be corrected and thus the computation can be executed fault tolerantly if the temperature is below a threshold value. Next, the fault-tolerant quantum computation on distributed quantum computers is investigated. A distributed quantum computer is composed of many small components, each of which only contains one or few qubits. These small components are networked together by communications of single photons in order to constitute a full scale quantum computer. The distributed architecture can also be used for the long-distance quantum communication. We find that distributed quantum computers composed of single-qubit components can be utilized as quantum repeaters. Moreover, entanglement over arbitrary distances can be generated on a two-dimensional quantum network with a fixed number of (e.g. five) quantum memories in each node. Then, we propose a protocol for the creation of photonic Greenberger-Horne-Zeilinger and linear cluster states emitted from a single atom or ion coupled to an optical cavity field. Finally, we investigate hybrid entangling gates via scattering between a flying photonic qubit and an atomic qubit (an emitter) coupled with a one-dimensional wave guide, which allow for measurement-based quantum computations sequentially distributed among the single-emitter quantum memories.

List of Publications

Publications:

[1] “Fault Tolerant Quantum Computation with Nondeterministic Gates”, Ying Li, Sean D. Barrett, Thomas M. Stace, and Simon Benjamin, *Phys. Rev. Lett.* **105**, 250502 (2010).

[2] “Photonic multiqubit states from a single atom”, Ying Li, Leandro Aolita, and Leong Chuan Kwek, *Phys. Rev. A* **83**, 032313 (2011).

[3] “Thermal States as Universal Resources for Quantum Computation with Always-On Interactions”, Ying Li, Daniel E. Browne, Leong Chuan Kwek, Robert Raussendorf, and Tzu-Chieh Wei, *Phys. Rev. Lett.* **107**, 060501 (2011).

[4] “Long-distance entanglement generation with scalable and robust two-dimensional quantum network”, Ying Li, Daniel Cavalcanti, and Leong Chuan Kwek, *Phys. Rev. A* **85**, 062330 (2012).

[5] “Optimal irreversible stimulated emission”, D. Valente, Y. Li, J. P. Poizat, J. M. Gérard, L.C. Kwek, M.F. Santos, and A. Auffèves, *New J. Phys.* **14**, 083029 (2012).

[6] “Universal optimal broadband photon cloning and entanglement creation in one dimensional atoms”, D. Valente, Y. Li, J. P. Poizat, J. M. Gérard, L.C. Kwek, M.F. Santos, and A. Auffèves, *Phys. Rev. A* **86**, 022333 (2012).

[7] “High threshold distributed quantum computing with three-qubit nodes”, Ying Li and Simon Benjamin, *New J. Phys.* **14**, 093008 (2012).

[8] “Robust-fidelity atom-photon entangling gates in the weak-coupling regime”, Ying Li, Leandro Aolita, Darrick E. Chang, and Leong Chuan Kwek, *Phys. Rev. Lett.* **109**, 160504 (2012).

[9] “Long range failure-tolerant entanglement distribution”, Ying Li, Sean D. Barrett, Thomas M. Stace, and Simon Benjamin, *New J. Phys.* **15**, 023012 (2013).

[10] “Operator Quantum Zeno Effect: Protecting Quantum Information with Noisy Two-qubit Interactions”, Shu-Chao Wang, Ying Li, Xiang-Bin Wang, and Leong Chuan Kwek, *Phys. Rev. Lett.* **110**, 100505 (2013).

[11] “Topological quantum computing with a noisy network and percent-level error rates”, Naomi H. Nickerson, Ying Li, and Simon Benjamin, *Nat. Commun.* **4**, 1756 (2013).

Preprints:

[1] “Photonic polarization gears for ultra-sensitive angular measurements”, Vincenzo D’Ambrosio, Nicolás Spagnolo, Lorenzo Del Re, Sergei Slussarenko, Ying Li, Leong Chuan Kwek, Lorenzo Marrucci, Stephen P. Walborn, Leandro Aolita, and Fabio Sciarrino, arXiv:1306.6685, accepted by *Nature Communications*.

[2] “Operator Quantum Zeno Dynamics”, Ying Li, David Herrera-Martí, and Leong Chuan Kwek, arXiv:1307.5140.

Introduction

For many years, scientists have been working on scalable quantum computing and long distance quantum communication due to their unique advantages[1]. Quantum computers could be able to solve certain problems much faster than any classical computer by using the best currently known algorithms, like integer factorization using quantum Shor's algorithm or the simulation of quantum many-body systems. A useful quantum computer has to be scalable, e.g. the factorization of a 200-digit number requires thousands of qubits [2]. The scalability of quantum computers requires the ability of manipulating a large number of quantum bits (qubits) precisely, and it is critical for quantum computing. Quantum communication is the art of transferring quantum states from one location to another, which is used for quantum cryptography and sharing quantum information between quantum computers. Quantum cryptography can complete some cryptographic tasks that are proven or conjectured to be impossible using only classical communication. Quantum states of light are usually used for transferring quantum bits. City-scale optical quantum communication has been realized, but global quantum communication is still a challenge due to strong losses of photons in optical fibres.

Many candidates of the platform for quantum information processing (QIP) are currently being explored, ranging from isolated atoms to solid

systems. Single ions can be confined in free space by appropriate electric fields [3, 4, 5]. These ions have excellent coherence properties of certain energy levels due to being well isolated from sources of decoherence. Trapped ions can be entangled through a laser-induced coupling mediated by a collective mode of harmonic motion in the trap [6, 7]. Making two neighbouring ions interact controllably requires precise manipulation of their motional degrees of freedom. A lot of work is needed to realize an architecture of QIP with trapped ions in a scalable way [8, 9, 10]. Solid state devices may be easier to assemble and cool. However, most of these systems require very low temperatures, as they are usually strongly coupled to environments. For example, quantum dots operate at the temperature $\sim 1\text{K}$ [11, 12], and thermal effects are depressed at the temperature $\sim 10\text{mK}$ in superconducting qubits [13, 14]. In contrast, nitrogen-vacancy (NV) centres are deep defects in large band gap materials (diamonds) [15], thereby their states are stable even at large temperatures, e.g. the T_1 limit is expected to be of the order of seconds at room temperature [16]. The challenge in using NV centres for quantum computation is that the interaction is extremely short-range [17, 18].

In this thesis we theoretically discuss some proposals of QIP without precise manipulations of interactions over a large number of qubits.

Standard quantum computing uses the unitary evolution as a basic mechanism for QIP. Another paradigm is the measurement-based quantum computing (MBQC), in which one processes quantum information by single-particle operations and measurements on a non-trivial entangled state [19, 20, 21]. Such entangled states serve as universal resources of MBQC [22]. These universal resources can be prepared without a precise control of interactions, even without direct interactions between atoms or

solid qubits. Therefore, the idea of MBQC may simplify scalable quantum computing. In Chapter 2, we describe how to use low-temperature thermal states as universal resources. Usually, it is implicitly assumed that the interactions between qubits can be switched off after universal resources are prepared, so that the dynamics of the measured qubits do not affect the computation. By proposing a model spin Hamiltonian, we demonstrate that MBQC can be achieved on a thermal state with always-on two-body interactions. Moreover, computational errors induced by thermal fluctuations can be corrected and thus the computation can be executed fault-tolerantly if the temperature is below a threshold value. In Chapter 3 and Chapter 4, we discuss the possibility of using a distributed quantum processor to achieve scalability by networking together many small components. Each small component contains one or few trapped ions [23] or a NV center [24] coupled with the optical field. By jointly detecting photons emitted from isolated components, we can entangle them into a universal resource. In such an approach to quantum computing, the operations between qubits are non-deterministic and likely to fail. These entangling operations (EOs) between components should be assumed to be failure prone. In Chapter 3, we focus on the logical limit of this architecture that each component contains only one qubit. We investigate fault-tolerant quantum computation (FTQC) with both large heralded failure rates and other unknown errors of operations. We find that computation is supported for remarkably high failure rates (exceeding 90%) providing that failures are heralded, meanwhile the rate of unknown errors should not exceed 2 in 10^4 operations. In Chapter 4, we consider more general architectures of distributed quantum computing, in which each component contains more than one qubits. We find that with three qubits in each component, the infidelity of remote EOs

may be permitted to approach 10% if the infidelity in local operations is of order 0.1%.

Today, it is possible to transfer quantum states with photons over more than 100km [25, 26, 27, 28]. However, when the distance increases, quantum communication becomes harder, because the success probability of transmitting a qubit and the fidelity of the resulting quantum state decreases exponentially with distance by using direct transmission. One of the most celebrated solutions to this problem is the use of quantum-repeaters [29]. The distance between two neighbouring repeaters is usually short, and entanglements between them can be prepared by transmitting photons. With quantum operations inside each repeater, a long distance entanglement can be generated by consuming these short distance entanglements. As a drawback, this strategy consumes an amount of quantum memories per repeater that grows with the distance for establishing entanglement, even when error-correction is used [30, 31]. Therefore, we meet the same challenge of scalable quantum computing in quantum communication. In Chapter 5, we show how to distribute entanglements with quantum repeaters on the distributed quantum computing architecture, on which it is believed that achieving scalability is easier.

The distribution of entanglement in quantum networks has been the focus of intense research. Non-trivial geometry of the quantum network can be used, for instance, in entanglement percolation [32] or error correction strategies [33, 34, 35, 36]. However, all the known results in this direction relies on unrealistic quantum states [32, 37, 38, 39, 40, 41, 42] or networks with an impractical geometry (e.g. three-dimensional) [33, 35, 36] or the consumption of a growing amount of local resources [34, 43]. Entanglement distribution in a noisy two-dimensional network with a fixed local

resources is believed to be possible through one-dimensional fault-tolerant quantum computation schemes [34, 36]. However such a scheme often requires quantum communications and operations with a very small error rate (approximately 10^{-5}) [44, 45]. In Chapter 6, we show that it is possible to entangle two distant sites in a two-dimensional network involving realistic quantum channels. In the present proposal, the number of quantum memories per node needed is fixed and it does not scale with the communication distance. So, the scalability of the two-dimensional quantum network does not rely on the scalability of quantum processors. Moreover quantum communication error rates of up to 1.67% can be tolerated.

Interfaces of photonic qubits and materiel qubits are important for both distributed quantum information computation and quantum networking. Atom-cavity systems make excellent single-photon-single-atom interfaces [46, 47, 48, 49, 50, 51, 52]. In Chapter 7, we propose a family of protocols for the creation of photonic Greenberger-Horne-Zeilinger (GHZ) [53] and linear cluster [19] states emitted from a single atom or ion coupled to an optical cavity field. Recently, another interface was proposed, in which optical fields are tightly concentrated by a one-dimensional waveguide coupled with an optical emitter [54]. In Chapter 8, we investigate how to achieve a high-fidelity matter-photon universal entangling gate via the scattering between atomic qubits (emitters) and travelling photonic qubits in the waveguide. We show that the fidelity of such a scattering gate can be unit in spite of the linewidth of the incident photon and the coupling strength of the emitter and the wave guide.

Thermal States as Universal Resources for Quantum Computation with Always-on Interactions

2.1 Introduction

Universal resources of MBQC are needed for one-way quantum computers, on which any quantum algorithm can be simulated via single-particle operations and measurements [19, 20]. The first identified universal resource of MBQC was the cluster state [55]. The cluster state can be obtained as the unique ground state of a Hamiltonian with five-body interactions [33, 56, 57], but can never occur as the unique ground state of any two-body Hamiltonian [58]. Fortunately, there exist universal resources that are the unique ground states of two-body Hamiltonians, albeit with particles of local Hilbert space larger than that of a qubit. These two-body Hamiltonians include the tricluster model [59], an Affleck-Kennedy-Lieb-Tasaki(AKLT)-like model [60], the two-dimensional AKLT model [61, 62, 63] and a quadratic Hamiltonian of continuous variables [64]. However, in order to use the ground state of a system as a universal resource, one usually needs

Chapter 2. Thermal States as Universal Resources for Quantum Computation with Always-on Interactions

to switch off interactions of the system sequentially [59, 62, 63, 60, 65]. Otherwise, the desirable quantum correlations could be destroyed due to the time evolution of the state via interactions. Therefore, in previous proposals, MBQC based on ground states requires not only single-particle operations and measurements but also a good control of interactions. In this chapter, we show that it is possible to remove this extra requirement, i.e., MBQC can be performed with always-on interactions.

To this end, we propose a two-dimensional (2D) system and a three-dimensional (3D) system, whose ground states are universal resources for MBQC. We show that 2D and 3D systems can be generalized to a family of similar models. These spin models may be realized in physical systems such as cold atoms [66, 67, 68], polar molecules [69], trapped ions [70, 71] and Josephson junction array [72]. We construct a ground state as a universal resource for MBQC by showing that the ground state can be converted into a cluster state by single-particle operations and measurements [62, 63, 73, 74]. In practice, one obtains a thermal state instead of the ground state as a universal resource for MBQC. Thus an energy gap is needed to protect the state from thermal fluctuations, which is indeed the case in our model. However, it is not clear how high a temperature can be suffered before ruining the state as a universal resource of MBQC. Therefore, we investigate their thermal states and find that computational errors in MBQC induced by thermal fluctuations can be corrected as long as the temperature is below a certain value.

This chapter is organized as follows. We give an introduction of cluster states in Sec. 2.2. Some results of the topological FTQC are reviewed in Sec. 2.3. The 2D system and the 3D system are described in Sec. 2.5 and Sec. 2.6 respectively. We discuss computational errors induced by thermal

2.2. Cluster states

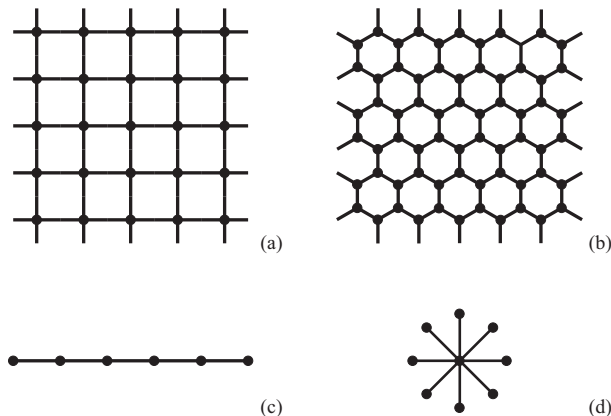


Figure 2.1: Some examples of cluster states and graph states. Square cluster states [subfigure (a)] and hexagonal cluster states [subfigure (b)] are universal resources of measurement-based quantum computing (MBQC), while linear cluster states [subfigure (c)] and star graph states [subfigure (d)] can not be used for universal MBQC.

fluctuations and the threshold of the temperature for FTQC in Sec. 2.7. Then, we show MBQC can be performed with always-on interactions in Sec. 2.8.

2.2 Cluster states

Cluster states are many-body entangled states [55], which are universal resources of MBQC [22]. The MBQC can utilize the entanglement of a universal resource state to simulate any quantum computing by single-qubit operations and measurements. Each kind of cluster states is associated with a lattice, see Fig. 2.1 (a) and (b) for examples. Cluster states are defined as follows: (i) there is one qubit located at each vertex; (ii) each qubit is initialized in the state $|+\rangle = (|0\rangle + |1\rangle)/\sqrt{2}$; and (iii) each edge denotes a controlled-phase gate on two connected qubits [55]. The controlled-phase gate on the qubit- a and the qubit- b reads

$$\Lambda_Z = (1 + Z_a + Z_b - Z_a Z_b)/2, \quad (2.1)$$

Chapter 2. Thermal States as Universal Resources for Quantum Computation with Always-on Interactions

where X, Y and Z are Pauli matrices σ^x , σ^y and σ^z respectively. The matrix representation of the controlled-phase gate is

$$\Lambda_Z = \begin{pmatrix} 1 & 0 & 0 & 0 \\ 0 & 1 & 0 & 0 \\ 0 & 0 & 1 & 0 \\ 0 & 0 & 0 & -1 \end{pmatrix}, \quad (2.2)$$

where basis are $|00\rangle$, $|01\rangle$, $|10\rangle$ and $|11\rangle$. Cluster states can also be defined by stabilizers [75],

$$K_a = X_a \prod_{b \in N_a} Z_b, \quad (2.3)$$

where N_a is the set of qubits containing all neighbours of qubit- a . A cluster state is an eigenstate with eigenvalue +1 of all the stabilizers. One can also define a state on a general graph, which is called a graph state [75]. All cluster states and graph states are entangled states, but not all of them are universal resources of MBQC, see Fig. 2.1 (c) and (d) for examples.

The square cluster state can be obtained as the unique ground state of the Hamiltonian

$$H = -J \sum_a K_a, \quad (2.4)$$

where J is the coupling constant and K_a are stabilizers [33]. These five-body interactions involved in this Hamiltonian are not natural and can only be obtained by perturbation from two-body interactions [56].

The explicit expression of a linear cluster state is (omitting normalization)

$$|\text{LCS}\rangle = \sum_{\mu_1, \mu_2, \mu_3, \dots = 0, 1} (-1)^{\mu_1 \mu_2 + \mu_2 \mu_3 + \dots} |\mu_1, \mu_2, \mu_3, \dots\rangle, \quad (2.5)$$

2.3. Topological fault-tolerance quantum computation

where $|\mu_a\rangle$ is the state of the qubit- a and the phase $(-1)^{\mu_a\mu_b}$ is a result of the controlled-phase gate on qubit- a and qubit- b . The explicitly expression of a star graph state is

$$|\text{SGS}\rangle = \frac{1}{\sqrt{2}}(|0_1, +_2, +_3, \dots\rangle + |1_1, -_2, -_3, \dots\rangle), \quad (2.6)$$

where the first qubit is the central qubit, while other qubits are flipped from $|+\rangle$ to $|-\rangle$ if the state of the central qubit is $|1\rangle$ due to controlled-phase gates. Here, $|-\rangle = (|0\rangle - |1\rangle)/\sqrt{2}$. Therefore, a star graph state is a GHZ state [53].

2.3 Topological fault-tolerance quantum computation

Topological FTQC was first proposed by R. Raussendorf and his collaborators in Refs. [76, 77, 78]. It is a scheme based on three-dimensional cluster states, but it can be implemented on a two-dimensional physical architecture. We are interested in the topological FTQC, because it not only tolerates computational errors but also qubit loss [79].

As described in R. Raussendorf's papers, the three-dimensional cluster state is defined on a cubic lattice. The elementary cell of the cubic lattice is shown in Fig. 2.2. There is one qubit on each face and each edge of the elementary cubic. Each qubit on a face is connected with its four neighboring qubits on edges. By shifting the lattice, one can transfer qubits on faces to edges while transfer qubits on edges to faces. The new lattice is called the dual lattice of the original primal lattice. We would like to call this three-dimensional cluster state as the topologically protected cluster (TPC) state. On the TPC state, after the error correction, whether errors

Chapter 2. Thermal States as Universal Resources for Quantum Computation with Always-on Interactions

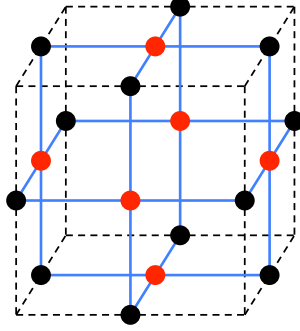


Figure 2.2: The elementary cell of the topologically protected cluster state. There is one qubit (a black or red round) on each face and edge of the cubic. Each qubit on a face is connected with its four neighboring qubits on edges.

induce a logical error only depends on their topology property.

Like cluster states, the TPC state is stabilized by $K_a = X_a \prod_{b \in N_a} Z_b$, where $N(a)$ is the set of four qubits on primal (dual) edges of the primal (dual) face with the qubit- a . The TPC state is also stabilized by $K(c) = \prod_{a \in c} X_a \prod_{b \in \partial c} Z_b$, where c is an arbitrary primal (dual) surface and ∂c is the primal (dual) chain as the boundary of c . Qubits in the set c (∂c) are located on faces (edges) composing the surface (chain) c (∂c). Here, $K(c)$ is the product of stabilizers K_a corresponding to primal (dual) faces on the primal (dual) surface c .

On the TPC state, any error is equivalent to a phase error or a correlated phase error. Because the TPC state is the eigenstate of stabilizers K_a , a flip error is equivalent to a product of phase errors as $[X_a] = \prod_{b \in N_a} [Z_b]$, where $[X]$ is the superoperator of a flip error and $[Z]$ is the superoperator of a phase error. Here, $[E](\Psi) = E\Psi E^\dagger$, where Ψ is the density matrix of a state.

Most of the qubits on the TPC state are measured in the X basis $\{|+\rangle, |-\rangle\}$. The outcome of a measurement in the X basis is wrong if there is a phase error on the measured qubit. One can detect phase errors

2.3. Topological fault-tolerance quantum computation

by using stabilizers corresponding to closed surfaces. For a closed surface, the corresponding stabilizer is a product of X , $K(c_c) = \prod_{a \in c_c} X_a$, where c_c denotes the closed surface. Therefore, the product of measurement outcomes of these X should be $+1$. If the product is -1 rather than $+1$, there should be odd phase errors on the corresponding qubits. In this way, one uses stabilizers of closed surfaces of elementary cubics to detect phase errors, which are called parity check operators. An error chain, which is a sequence of phase errors on primal (dual) faces, going through an elementary cubic puts two phase errors on the elementary cubic, i.e. the outcome of the corresponding parity check operator is $+1$. Only at the end of an error chain, the corresponding parity check operator is -1 . Therefore, parity check operators reveal the endpoints of error chains. One can correct errors by pairing error syndromes to find error chains, which are parity check operators with -1 outcomes.

Phase errors do not affect measurements in the Z basis. With measurement in the X basis and Z basis, we can execute Clifford gates. There may be some errors on qubits measured in other bases, which are corrected via Clifford gates.

If the probability of errors are lower than a threshold, one can reduce the probability of errors after correction to any low value by increasing redundancy. The error threshold depends on the classical algorithm for pairing syndromes. If phase errors occur independently on the cluster state, the probability threshold of phase errors on each qubit is 3.20% by using the random plaquette Z_2 -gauge model [80] and 2.93% by using the minimum-weight perfect matching algorithm [81]. An imperfect operation with depolarized errors can be described as a combination of a perfect operation

Chapter 2. Thermal States as Universal Resources for Quantum Computation with Always-on Interactions

and an erroneous superoperation,

$$\begin{aligned} E_1 &= (1 - p_1) + \frac{p_1}{3}([X] + [Y] + [Z]) \\ &= \left(1 - \frac{4}{3}p_1\right)[1] + \frac{p_1}{3}([1] + [Z])([1] + [X]) \end{aligned} \quad (2.7)$$

for single-qubit operations (initialization, single-qubit gates and measurements) and

$$\begin{aligned} E_2 &= (1 - p_2) + \frac{p_2}{15}([I_1 X_2] + \dots + [Z_1 I_2] + \dots + [X_1 Y_2] + \dots) \\ &\quad \left(1 - \frac{16}{15}p_2\right) + \frac{p_2}{15}([1] + [Z_1])([1] + [X_1])([1] + [Z_2])([1] + [X_2]) \end{aligned} \quad (2.8)$$

for two-qubit operations (e.g. controlled-phase gates), where p_1 and p_2 are corresponding error rates. We have assumed here that errors are all depolarized. If $p_1 = p_2$, the threshold of error rate is 0.75% by using the random plaquette Z_2 -gauge model [77] and 0.58% by using the minimum-weight perfect matching algorithm [76].

In the topological FTQC, some of phase errors can be correlated. By using parity check operators to detect phase errors, error corrections of qubits on the faces (primal qubits, red qubits in Fig. 2.2) and qubits on the edges (dual qubits, blue qubits in Fig. 2.2) are performed independently. Therefore, correlations between two sets of qubits can be neglected.

The topological FTQC can tolerate not only computational errors but also qubit loss. Numerical evidence suggests that, by using the minimum-weight perfect matching algorithm the error threshold decreases approximately linearly with the probability of qubit loss and qubit loss less than 24.9% is tolerable [79]. Then, for independent phase errors, we can estimate

2.4. Measurement-based quantum computing

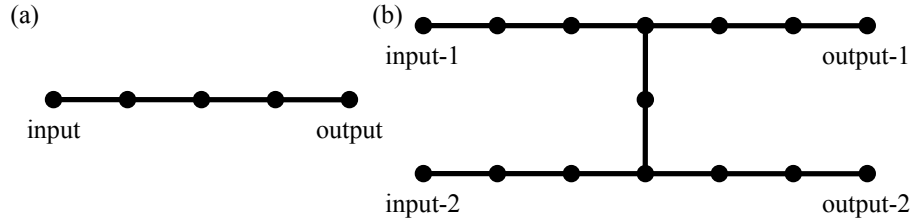


Figure 2.3: Structures used for implementing (a) single-qubit operations and (b) two-qubit operations.

error thresholds with

$$\varepsilon_t = 2.93\% - \frac{2.93\%}{24.9\%} p_{\text{loss}}, \quad (2.9)$$

where ε_t is the probability threshold of phase errors on each qubit of the TPC state, p_{loss} is the loss rate.

2.4 Measurement-based quantum computing

To process quantum information with universal resources, particles are measured in a certain order and in a certain basis. The strategies of MBQC are different for different universal resources. In order to simulate a full scale quantum computer, a 2D cluster state [Fig. 2.1 (a)] is first reshaped into a network of some fundamental structures due to the simulated quantum circuit [19, 20]. This task is done by measurements on redundant qubits in the computational basis. There are two kinds of fundamental structures as shown in Fig. 2.3, (a) a linear structure used to propagate the quantum information and simulate single-qubit rotations, (b) an H-structure is used to simulate a two-qubit operation, e.g. a controlled-NOT gate. Qubits are measured from left to right in bases according to simulated operations in order to simulate corresponding quantum operations.

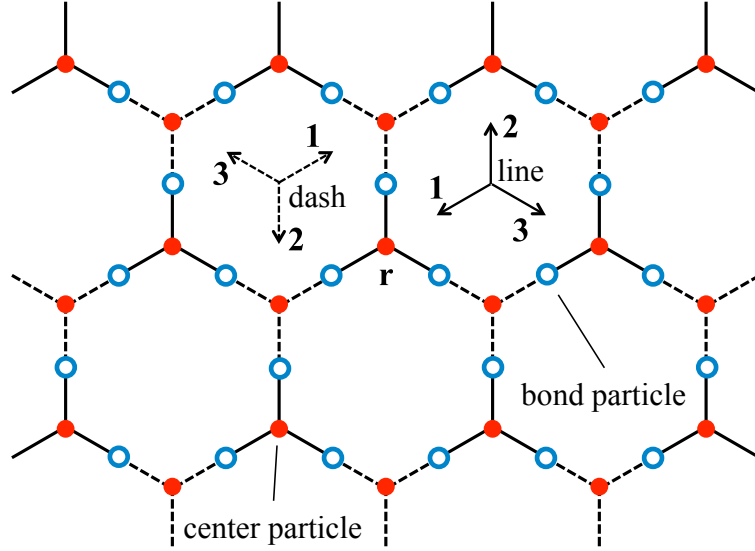


Figure 2.4: The two-dimensional system composed of spin-3/2 particles. The system is a hexagonal lattice, where center particles (red round) are located on vertices, while bond particles (blue ring) are located on edges. There are two kinds of interactions between center particles and bond particles, V_{line} (line) and V_{dash} (dash line). \mathbf{r} denotes the position of a center particle, and the vectors between the center particle and its three interacting bond particles are $\mathbf{1}$, $\mathbf{2}$, $\mathbf{3}$ respectively.

2.5 2D System

The 2D system shown in Fig. 2.4 is a hexagonal lattice with one more particle on each edge. The system is composed of spin-3/2 particles, in which particles on edges are called bond particles, while others are called center particles. Particles are combined by two types of interactions

$$V_{\text{line}} = \Delta(S_c^x A_b^x + S_c^y A_b^y + S_c^z A_b^z), \quad (2.10)$$

$$V_{\text{dash}} = \Delta(S_c^x B_b^x + S_c^y B_b^y + S_c^z B_b^z), \quad (2.11)$$

2.5. 2D System

where S_c^α is the spin operator of the corresponding center particle, and A_b^α, B_b^α are operators of the corresponding bond particle. Here,

$$A_b^x = (S_b^{-2} + S_b^{+2})/4\sqrt{3}, \quad (2.12)$$

$$A_b^y = i(S_b^{-2} - S_b^{+2})/4\sqrt{3}, \quad (2.13)$$

$$A_b^z = S_b^z(13 - 4S_b^{z2})/12 \quad (2.14)$$

and

$$B_b^x = (S_b^x + 4S_b^z S_b^x S_b^z)/4\sqrt{3}, \quad (2.15)$$

$$B_b^y = (S_b^y + 4S_b^z S_b^y S_b^z)/4\sqrt{3}, \quad (2.16)$$

$$B_b^z = S_b^z(4S_b^{z2} - 7)/6. \quad (2.17)$$

The four states of a bond particle are

$$|3/2\rangle = |\uparrow\rangle_A \otimes |\uparrow\rangle_B, \quad (2.18)$$

$$|1/2\rangle = |\uparrow\rangle_A \otimes |\downarrow\rangle_B, \quad (2.19)$$

$$|-1/2\rangle = |\downarrow\rangle_A \otimes |\uparrow\rangle_B, \quad (2.20)$$

$$|-3/2\rangle = |\downarrow\rangle_A \otimes |\downarrow\rangle_B, \quad (2.21)$$

where, $|m\rangle$ is the eigenstate of S_b^z with eigenvalue m , and $|\uparrow\rangle_I$ ($|\downarrow\rangle_I$) is the eigenstate of I_b^z with eigenvalue $1/2$ ($-1/2$). Operators of bond particles satisfy commutation relations $[I_b^\alpha, J_b^\beta] = i\delta_{IJ}\varepsilon_{\alpha\beta\gamma}I_b^\gamma$ and $\vec{I}_b^2 = 3/4$, where $I, J = A, B$, and $\alpha, \beta, \gamma = x, y, z$. Therefore, A_b^α and B_b^α are two sets of independent spin-1/2 operators. We would like to remark that there are other choices of A_b^α and B_b^α that satisfy conditions of spin-1/2 operators.

The Hamiltonian of the system is $H = \sum_{\mathbf{r}} h_{\mathbf{r}}$, where $h_{\mathbf{r}} = \Delta \vec{S}_{\mathbf{r}} \cdot \vec{I}_{\mathbf{r}}$, $\vec{I}_{\mathbf{r}} = \vec{I}_{\mathbf{r}+1} + \vec{I}_{\mathbf{r}+2} + \vec{I}_{\mathbf{r}+3}$, and \mathbf{r} denotes the position of a center particle,

$\mathbf{r} + \mathbf{a}$ denotes the position of one bond particle interacting with the center particle \mathbf{r} , where, $\{\mathbf{a}\}$ depends on $I \in \{A, B\}$ as shown in Fig. 2.4.

2.5.1 Ground state and energy gap

We can rewrite $h_{\mathbf{r}}$ as $h_{\mathbf{r}} = \Delta(\vec{T}_{\mathbf{r}}^2 - \vec{S}_{\mathbf{r}}^2 - \vec{I}_{\mathbf{r}}^2)/2$, where $\vec{T}_{\mathbf{r}} = \vec{S}_{\mathbf{r}} + \vec{I}_{\mathbf{r}}$. Here, $\vec{S}_{\mathbf{r}}$, $\vec{I}_{\mathbf{r}}$ and $\vec{T}_{\mathbf{r}}$ all satisfy commutation relations of spin operators. Therefore,

$$h_{\mathbf{r}} = \frac{\Delta}{2}[T_{\mathbf{r}}(T_{\mathbf{r}} + 1) - S_{\mathbf{r}}(S_{\mathbf{r}} + 1) - I_{\mathbf{r}}(I_{\mathbf{r}} + 1)], \quad (2.22)$$

where $S_{\mathbf{r}} = 3/2$ and $I_{\mathbf{r}} = 1/2$ or $3/2$. When $I_{\mathbf{r}} = 1/2$, $T_{\mathbf{r}} = 1, 2$. When $I_{\mathbf{r}} = 3/2$, $T_{\mathbf{r}} = 0, 1, 2, 3$. One gets the minimum energy by taking $I_{\mathbf{r}} = 3/2$ and $T_{\mathbf{r}} = 0$, which gives the ground state, $|g\rangle_{\mathbf{r}}$, of $h_{\mathbf{r}}$ with a total spin of zero. The energy difference between the ground state and the first excited state is Δ . Because these $h_{\mathbf{r}}$ are independent of each other, the ground state of the whole system is $|G\rangle = \bigotimes_{\mathbf{r}} |g\rangle_{\mathbf{r}}$ and protected by an energy gap Δ . The energy gap only depends on the interaction constant, and does not vanish in the thermodynamic limit.

2.5.2 POVM and GHZ state

As a preliminary step of MBQC on the ground state, we consider the POVM (Positive Operator Valued Measure) $F^{\alpha} = (S_{\mathbf{r}}^{\alpha 2} - 1/4)/\sqrt{6}$ with $\mathbf{I} = \sum_{\alpha=x,y,z} F^{\alpha\dagger} F^{\alpha}$. The POVM is performed on center particles, and projects the center spin into the subspace spanned by two states with maximum spin component in the α direction. Since the ground state $|g\rangle_{\mathbf{r}}$ has a total spin 0, all three spin- $I_{\mathbf{r}+\mathbf{a}}$ are antiparallel with the center spin- $S_{\mathbf{r}}$. Therefore, the POVM projects the state $|g\rangle_{\mathbf{r}}$ into a GHZ state, e.g., for the outcome

2.5. 2D System

z , the output state is $|\text{ghz}\rangle_{\mathbf{r}} = (|\tilde{0}000\rangle + |\tilde{1}111\rangle)/\sqrt{2}$, where $|\tilde{0}\rangle = -|3/2\rangle$, $|\tilde{1}\rangle = |-3/2\rangle$ are the state of the center spin- $S_{\mathbf{r}}$, and $|0\rangle = |\uparrow\rangle$, $|1\rangle = |\downarrow\rangle$ are states of bound particles. The state $|g\rangle_{\mathbf{r}}$ is an isotropic state. Therefore, all outcomes are equivalent to the outcome z up to a set of single-particle operations $U(\hat{\alpha}) = \exp[i\vec{T} \cdot \vec{n}(\hat{\alpha})]$, where α is the outcome and $\vec{n}(\hat{\alpha}) = \hat{\alpha} \times \hat{z} \arcsin(|\hat{\alpha} \times \hat{z}|)/|\hat{\alpha} \times \hat{z}|$. The state of the whole system after POVMs and single-particle operations is $|\{\text{ghz}\}\rangle = \bigotimes_{\mathbf{r}} |\text{ghz}\rangle_{\mathbf{r}}$, which can also be described by a set of stabilizers, $W_{\mathbf{r}} = X_{\mathbf{r}} \prod_{\mathbf{a}=1,2,3} 2I_{\mathbf{r}+\mathbf{a}}^x$ and $W_{\mathbf{r},\mathbf{r}+\mathbf{a}} = 2Z_{\mathbf{r}} I_{\mathbf{r}+\mathbf{a}}^z$ for all \mathbf{r} and \mathbf{a} . $|\{\text{ghz}\}\rangle$ is the eigenstate with eigenvalue 1 of all of these stabilizers, where, X , Y and Z are Pauli operators of the qubit $\{|\tilde{0}\rangle, |\tilde{1}\rangle\}$.

2.5.3 Cluster state and universality of the ground state

By measuring physical quantities $A_{\mathbf{b}}^x B_{\mathbf{b}}^z$ and $A_{\mathbf{b}}^z B_{\mathbf{b}}^x$ on the bond particles, the state $|\{\text{ghz}\}\rangle$ can be projected [82, 83, 84] (or “fused”) into a hexagonal cluster state, which has the same lattice as the center particles. The eigenstate with $A_{\mathbf{b}}^x B_{\mathbf{b}}^z = (1 - 2\mu)/4$ and $A_{\mathbf{b}}^z B_{\mathbf{b}}^x = (1 - 2\nu)/4$ is

$$|\mu, \nu\rangle = (|3/2\rangle + i^{2\nu} |1/2\rangle + i^{2\mu} |-1/2\rangle - i^{2\mu} i^{2\nu} |-3/2\rangle)/2, \quad (2.23)$$

where $\mu, \nu = 0, 1$. $|\mu, \nu\rangle$ are the measurement basis. By considering a product of stabilizers

$$W_{\mathbf{r}} \prod_{\mathbf{a}=1,2,3} W_{\mathbf{r}+2\mathbf{a},\mathbf{r}+\mathbf{a}} = X_{\mathbf{r}} \prod_{\mathbf{a}=1,2,3} Z_{\mathbf{r}+2\mathbf{a}} (4A_{\mathbf{r}+\mathbf{a}}^x B_{\mathbf{r}+\mathbf{a}}^z), \quad (2.24)$$

one can get a new stabilizer by replacing $A_{\mathbf{b}}^x B_{\mathbf{b}}^z$ with the appropriate outcomes. In Eq. (2.24), we have taken the case $I_{\mathbf{r}+\mathbf{a}}^x = A_{\mathbf{r}+\mathbf{a}}^x$ as an example,

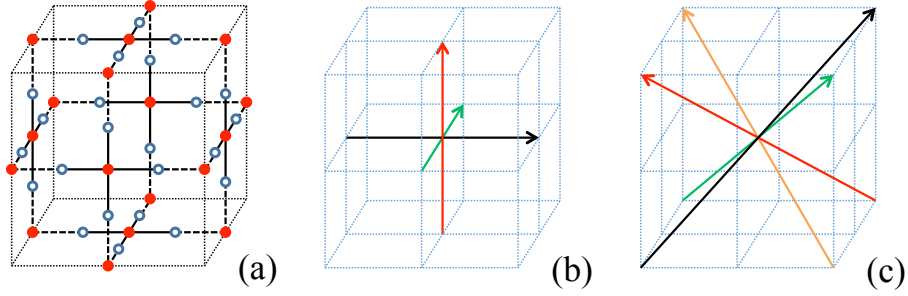


Figure 2.5: The three-dimensional system. (a) The elementary cell of the system. The system is composed of spin-2 particles and spin-3/2 particles. Spin-2 particles are center particles (red round), and spin-3/2 particles are bond particles (blue ring). (b) Three directions for $k \leq 3$ of the POVM on spin-2 particles, which are orthogonal with each other and passing face centers of a cube. (c) Four directions for $k \geq 4$ of the POVM on spin-2 particles, which are along body diagonals of the same cube.

and the result is the same for $I_{\mathbf{r}+\mathbf{a}}^x = B_{\mathbf{r}+\mathbf{a}}^x$. The new stabilizers define a hexagonal cluster state on center particles up to a Pauli frame, and then can be corrected by single-particle operations [19, 20, 21]. Since the hexagonal cluster state is a universal resource for MBQC [22], universal MBQC can be performed on center particles.

2.6 3D system and topologically protected cluster state

Following the idea of the 2D system, we propose a 3D system whose ground state is also a universal resource for MBQC. The system shown in Fig. 2.5 (a) is composed of spin-2 particles and spin-3/2 particles, where center particles are spin-2 particles and bond particles are spin-3/2 particles. The interactions between particles are the same as in Eq. (2.10) and (2.11). Therefore, the Hamiltonian of the 3D system has the same form as 2D system, $H = \sum_{\mathbf{r}} h_{\mathbf{r}}$, $h_{\mathbf{r}} = \Delta \vec{S}_{\mathbf{r}} \cdot \vec{T}_{\mathbf{r}}$, where $\vec{T}_{\mathbf{r}} = \vec{T}_{\mathbf{r}+\mathbf{1}} + \vec{T}_{\mathbf{r}+\mathbf{2}} + \vec{T}_{\mathbf{r}+\mathbf{3}} + \vec{T}_{\mathbf{r}+\mathbf{4}}$, where $\{\mathbf{r}+\mathbf{a}\}$ denote four bond particles interacting with the center

2.6. 3D system and topologically protected cluster state

particle \mathbf{r} .

In the 3D system, one can get the minimum energy of $h_{\mathbf{r}}$ by taking $I_{\mathbf{r}} = 2$ and $T_{\mathbf{r}} = 0$ in Eq. (2.22). Therefore, in the 3D system, the ground state of each $h_{\mathbf{r}}$ is an isotropic state with a total spin 0. The energy difference between the ground state and the first excited state is Δ , which means the 3D system is also gapped.

The ground state of the 3D system can be reduced to a 3D cluster state, a TPC state as shown in Fig. 2.2. Firstly, center particles are measured using a POVM with seven outcomes, $F(\hat{\alpha}_k) = \sqrt{N_k}P(\hat{\alpha}_k)$ such that $\mathbf{I} = \sum_{k=1}^7 F^\dagger(\hat{\alpha}_k)F(\hat{\alpha}_k)$. Here,

$$P(\hat{\alpha}) = |\hat{\alpha}; 2\rangle \langle \hat{\alpha}; 2| + |\hat{\alpha}; -2\rangle \langle \hat{\alpha}; -2| \quad (2.25)$$

projects the center spin into the subspace spanned by two states with maximum spin component in the $\hat{\alpha}$ direction, and $|\hat{\alpha}; m\rangle$ is the eigenstate of $\hat{\alpha} \cdot \vec{S}_{\mathbf{c}}$ with eigenvalue m . $N_k = 1/3$ for $k \leq 3$ and $N_k = 3/8$ for $k \geq 4$. The seven directions are shown in Fig. 2.5 (b) and (c). Because four spins $\{I_{\mathbf{r}+\mathbf{a}}\}$ are all antiparallel with the center spin- $S_{\mathbf{r}}$, the output states of the POVM are all GHZ states. These GHZ states are equivalent to the GHZ state with outcome z , up to single-particle operations $U(\hat{\alpha})$. Therefore, POVMs on the center particles, with $U(\hat{\alpha})$ together, can transform the ground state to a state stabilized by $W_{\mathbf{r}} = X_{\mathbf{r}} \prod_{\mathbf{a}} 2I_{\mathbf{r}+\mathbf{a}}^x$ and $W_{\mathbf{r},\mathbf{r}+\mathbf{a}} = 2Z_{\mathbf{r}}I_{\mathbf{r}+\mathbf{a}}^z$, where $\mathbf{a} = \mathbf{1}, \mathbf{2}, \mathbf{3}, \mathbf{4}$.

Measuring physical quantities $A_{\mathbf{b}}^x B_{\mathbf{b}}^z$ and $A_{\mathbf{b}}^z B_{\mathbf{b}}^x$, one can generate a new set of stabilizers $X_{\mathbf{r}} \prod_{\mathbf{a}} Z_{\mathbf{r}+2\mathbf{a}}$, which defines a TPC state on center particles, as shown in Fig. 2.2. On the TPC state, quantum correlations are protected topologically and fault tolerant quantum computing can be simulated using topological error correction [76, 77].

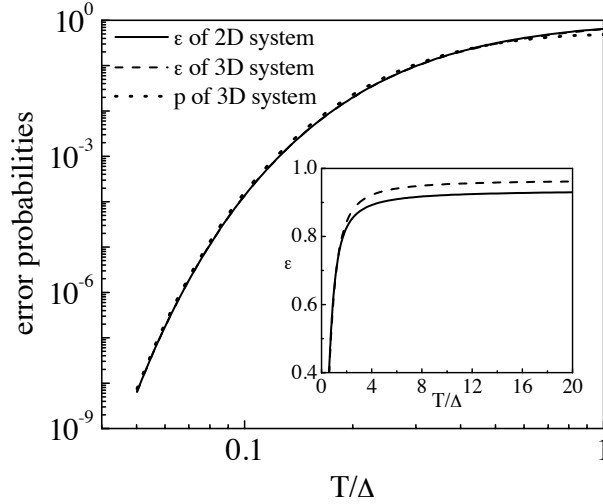


Figure 2.6: Error probabilities ε on a GHZ state and p on the cluster state as functions of the temperature. For 2D system the GHZ state is a four-qubit state, and for 3D system the GHZ state is a five-qubit state. ε are almost the same for 2D and 3D systems when the temperature $T < \Delta$. When $T/\Delta = 0.2$, $p = 3\%$, which means errors induced by a lower temperature are tolerable by using the topological error correction algorithm on the 3D system.

2.7 Thermal computational errors and error correction

We have proved the ground states of 2D and 3D systems are universal resources for MBQC. However, in practice, a system cannot reach the exact ground state, but rather a thermal state at finite temperature. Thermal fluctuations can reduce the quantum correlations on ground states and induce computational errors on the cluster state, which will be used for MBQC. The thermal state considered is the Gibbs state

$$\rho = Z^{-1}e^{-\beta H}, \quad (2.26)$$

where

$$Z = \text{tr}(e^{-\beta H}), \quad (2.27)$$

2.7. Thermal computational errors and error correction

$\beta = 1/T$ is the temperature, and ρ can be rewritten as $\rho = \prod_{\mathbf{r}} \rho_{\mathbf{r}}$. Here $\rho_{\mathbf{r}} = Z_{\mathbf{r}}^{-1} e^{-\beta h_{\mathbf{r}}}$ is the Gibbs state of $h_{\mathbf{r}}$. After the POVM and $U(\hat{\alpha})$, the state $\rho_{\mathbf{r}}$ is transformed into

$$\sigma_{\mathbf{r}} = \frac{F \rho_{\mathbf{r}} F^\dagger}{\text{tr}(F \rho_{\mathbf{r}} F^\dagger)}, \quad (2.28)$$

where $F = F^z$ for the 2D system and $F = F(\hat{z})$ for the 3D system. At an absolute zero temperature, $\sigma_{\mathbf{r}} = |\text{ghz}\rangle \langle \text{ghz}|_{\mathbf{r}}$ is the desired GHZ state. Here, $|\text{ghz}\rangle_{\mathbf{r}}$ is a GHZ state of four qubits for the 2D system and five qubits for the 3D system. The post-POVM state $\sigma_{\mathbf{r}}$ at finite T is only approximately a GHZ state, i.e., is equivalent to a perfect GHZ state affected by errors. The probability of an error occurring on the post-POVM state is $\varepsilon = 1 - \mathcal{F}$, where $\mathcal{F} = \text{tr}(\sigma_{\mathbf{r}} |\text{ghz}\rangle \langle \text{ghz}|_{\mathbf{r}})$ is the fidelity of the GHZ state., as shown in Fig. 2.6.

In the following section, we will study the errors on the GHZ states and how these errors propagate to errors on the cluster state. We will take the 3D system as an example, and the result for the 2D system is similar.

2.7.1 Errors on GHZ states

We denote eigenstates of $(S_{\mathbf{r}}^z, \vec{I}_{\mathbf{r}}^2, I_{\mathbf{r}}^z)$ as $|S^z; I, q, I^z\rangle$. When $I = 0, 1$, eigenstates are degenerate and we label these degenerate states by q . The state $|S^z; I, q, I^z\rangle$ can be written as

$$|S^z; I, q, I^z\rangle = \Xi_{I,q,I^z} |S^z; \downarrow\downarrow\downarrow\downarrow\rangle, \quad (2.29)$$

Chapter 2. Thermal States as Universal Resources for Quantum Computation with Always-on Interactions

where

$$\Xi_{I,q,I^z=-2} = 1, \quad (2.30)$$

$$\Xi_{I,q,I^z=-1} = \sum_{\mathbf{a}} C_{I,q,\mathbf{a}} 2I_{\mathbf{r}+\mathbf{a}}^x, \quad (2.31)$$

$$\Xi_{I,q,I^z=0} = \sum_{\mathbf{a}} \sum_{\mathbf{a}' \neq \mathbf{a}} C_{I,q,\mathbf{a},\mathbf{a}'} 4I_{\mathbf{r}+\mathbf{a}}^x I_{\mathbf{r}+\mathbf{a}'}^x, \quad (2.32)$$

$$\Xi_{I,q,I^z>0} = \Pi \Xi_{I,q,-I^z}, \quad (2.33)$$

$C_{I,q,\mathbf{a}}$ and $C_{I,q,\mathbf{a},\mathbf{a}'}$ are some coefficients and $\Pi = \prod_{\mathbf{a}} 2I_{\mathbf{r}+\mathbf{a}}^x$ flips all spin- $I_{\mathbf{r}+\mathbf{a}}$.

The eigenstates of $h_{\mathbf{r}}$ are $|I, q; T, T^z\rangle$, which are eigenstates of $(\vec{T}_{\mathbf{r}}^2, \vec{T}_{\mathbf{r}}^z, T_{\mathbf{r}}^z)$.

We write the thermal state as

$$\rho_{\mathbf{r}} = \sum_{I,q,T,T^z} p_{I,T} |I, q; T, T^z\rangle \langle I, q; T, T^z|, \quad (2.34)$$

where $|I, q; T, T^z\rangle$ is written in the basis $\{|S^z; I, q, I^z\rangle\}$ using Clebsch-Gordan coefficients. After performing the POVM, we get

$$\sigma_{\mathbf{r}} \propto \sum_{I,q,T,T^z} p_{I,T} F |I, q; T, T^z\rangle \langle I, q; T, T^z| F^\dagger, \quad (2.35)$$

where

$$\begin{aligned} F |I, q; T, T^z\rangle &= \alpha |S^z = 2; I, q, I^z = T^z - 2\rangle \\ &+ \beta |S^z = -2; I, q, I^z = T^z + 2\rangle. \end{aligned} \quad (2.36)$$

2.7. Thermal computational errors and error correction

We have assumed here the outcome is $F = P(\hat{z})$. Because $I \leq 2$, these two components never exist at the same time except when $T^z = 0$. Therefore,

$$F |I, q; T, T^z\rangle \propto \begin{cases} |S^z = 2; I, q, I^z = T^z - 2\rangle, & T^z > 0; \\ \delta_{I,S} Z_{\mathbf{r}}^\eta |\text{ghz}\rangle, & T^z = 0; \\ |S^z = -2; I, q, I^z = T^z + 2\rangle, & T^z < 0, \end{cases} \quad (2.37)$$

where $|\text{ghz}\rangle = (|S^z = 2; \downarrow\downarrow\downarrow\downarrow\rangle + |S^z = -2; \uparrow\uparrow\uparrow\uparrow\rangle)/\sqrt{2}$. When $T^z = 0$, the state $F |I, \delta; T, T^z\rangle$ is a GHZ state. Here $\eta = 0, 1$ depends on T . Using the symmetry property of Clebsch-Gordan coefficients $\langle S, S^z; I, I^z | T, T^z\rangle = (-1)^{S+I-T} \langle I, I^z; S, S^z | T, T^z\rangle$, we know that $\eta = [1 - (-1)^T]/2$. Therefore, we can write the state after the POVM as

$$\begin{aligned} \sigma_{\mathbf{r}} &= \mathcal{F} |\text{ghz}\rangle \langle \text{ghz}| + p_z Z_{\mathbf{r}} |\text{ghz}\rangle \langle \text{ghz}| Z_{\mathbf{r}} \\ &+ \sum_{I, q, I^z \neq -2} p_{I, q, I^z} (|S^z = 2; I, q, I^z\rangle \langle S^z = 2; I, q, I^z| \\ &+ |S^z = -2; I, q, -I^z\rangle \langle S^z = -2; I, q, -I^z|), \end{aligned} \quad (2.38)$$

where p_{I, q, I^z} is the probability of $|S^z = \pm 2; I, q, \pm I^z\rangle$, which is independent of the sign of S^z and I^z due to the symmetry of the state.

Using

$$|S^z = 2; I, q, I^z\rangle = \Xi_{I, q, I^z} \frac{1 - Z_{\mathbf{r}}}{\sqrt{2}} |\text{ghz}\rangle, \quad (2.39)$$

$$|S^z = -2; I, q, -I^z\rangle = \Xi_{I, q, I^z} \frac{1 + Z_{\mathbf{r}}}{\sqrt{2}} |\text{ghz}\rangle \quad (2.40)$$

we write $\sigma_{\mathbf{r}}$ as $\sigma_{\mathbf{r}} = \mathcal{E}_{\mathbf{r}}^{\text{ghz}}(|\text{ghz}\rangle \langle \text{ghz}|)$, where the erroneous operator

$$\begin{aligned} \mathcal{E}_{\mathbf{r}}^{\text{ghz}} &= \mathcal{F}[1] + p_z [Z_{\mathbf{r}}] \\ &+ \sum_{I, q, I^z \neq -2} p_{I, q, I^z} ([\Xi_{I, q, I^z}] + [Z_{\mathbf{r}}] \circ [\Xi_{I, q, I^z}]). \end{aligned} \quad (2.41)$$

2.7.2 Measurements on bond particles

The measurements of $A_{\mathbf{r}+\mathbf{a}}^x B_{\mathbf{r}+\mathbf{a}}^z$ and $A_{\mathbf{r}+\mathbf{a}}^z B_{\mathbf{r}+\mathbf{a}}^x$ on bond particles and single-particle operations based on measurement outcomes can be described by

$$\Lambda(\Psi) = \sum_{o_A=0}^1 \sum_{o_B=0}^1 O_{o_A, o_B} P_{o_A, o_B} \Psi P_{o_A, o_B}^\dagger O_{o_A, o_B}^\dagger, \quad (2.42)$$

where $(-1)^{o_A}$ is the outcome of $4A_{\mathbf{r}+\mathbf{a}}^x B_{\mathbf{r}+\mathbf{a}}^z$ and $(-1)^{o_B}$ is the outcome of $4A_{\mathbf{r}+\mathbf{a}}^z B_{\mathbf{r}+\mathbf{a}}^x$. Here,

$$P_{o_A, o_B} = \frac{1}{4} [1 + (-1)^{o_A} 4A_{\mathbf{r}+\mathbf{a}}^x B_{\mathbf{r}+\mathbf{a}}^z] \times [1 + (-1)^{o_B} 4A_{\mathbf{r}+\mathbf{a}}^z B_{\mathbf{r}+\mathbf{a}}^x], \quad (2.43)$$

$$O_{o_A, o_B} = Z_{\mathbf{r}}^{o_A} Z_{\mathbf{r}+2\mathbf{a}}^{o_B} (2A_{\mathbf{r}+\mathbf{a}}^z)^{o_A} (2B_{\mathbf{r}+\mathbf{a}}^x)^{o_B}. \quad (2.44)$$

We have taken $I = A$ for the center particle \mathbf{r} . P_{o_A, o_B} is the projector due to the measurement and the operation O_{o_A, o_B} are used to correct Pauli frame of center particles and initialize the bound particle. It is not needed to initialize the bond particle in application, but it can simplify the calculation.

If there is no error, we assume that the state before Λ is $|\psi\rangle$ and the state after Λ is $|\varphi\rangle$, $O_{o_A, o_B} P_{o_A, o_B} |\psi\rangle = 1/2 |\varphi\rangle$. With errors, the state before Λ can be written as $\rho_\psi = \sum_k p_k E_k |\psi\rangle \langle \psi| E_k^\dagger$. We consider one of the component, and E_k can be generally written as $E_k = (2aA_{\mathbf{r}+\mathbf{a}}^x + A')(2bB_{\mathbf{r}+\mathbf{a}}^x + B')Z_{\mathbf{r}}^\mu Z_{\mathbf{r}+2\mathbf{a}}^\nu E'$, where a, A', b, B' and E' are operators on other particles. Then,

$$\begin{aligned} & O_{o_A, o_B} P_{o_A, o_B} (2aA_{\mathbf{r}+\mathbf{a}}^x + A') \times (2bB_{\mathbf{r}+\mathbf{a}}^x + B') Z_{\mathbf{r}}^\mu Z_{\mathbf{r}+2\mathbf{a}}^\nu E' |\psi\rangle \\ &= \frac{1}{2} [(-1)^{1+o_A+o_B} ab Z_{\mathbf{r}+2\mathbf{a}} Z_{\mathbf{r}} + (-1)^{o_A} b Z_{\mathbf{r}+2\mathbf{a}} B' \\ & \quad + (-1)^{o_B} a A' Z_{\mathbf{r}} + A' B'] Z_{\mathbf{r}}^\mu Z_{\mathbf{r}+2\mathbf{a}}^\nu E' |\varphi\rangle. \end{aligned} \quad (2.45)$$

2.7. Thermal computational errors and error correction

Thus, $2A_{\mathbf{r}+\mathbf{a}}^x$ ($2B_{\mathbf{r}+\mathbf{a}}^x$) will be propagated to $Z_{\mathbf{r}+2\mathbf{a}}$ ($Z_{\mathbf{r}}$) and all off-diagonal contributions are zero after the sum over o_A and o_B .

Therefore, after measurements on the bond particles, errors on the GHZ states are propagated to errors on the cluster state as

$$[\Xi_{I,q,I^z}] \rightarrow \sum_{\mathbf{a}} |C_{I,q,\mathbf{a}}|^2 [Z_{\mathbf{r}+2\mathbf{a}}], \quad (2.46)$$

$$[\Xi_{I,q,I^z=0}] \rightarrow \sum_{\mathbf{a}} \sum_{\mathbf{a}' \neq \mathbf{a}} |C_{I,q,\mathbf{a},\mathbf{a}'}|^2 [Z_{\mathbf{r}+2\mathbf{a}} Z_{\mathbf{r}+2\mathbf{a}'}], \quad (2.47)$$

$$[\Pi] \rightarrow \left[\prod_{\mathbf{a}} Z_{\mathbf{r}+2\mathbf{a}} \right] = [X_{\mathbf{r}}], \quad (2.48)$$

where we have used that $X_{\mathbf{r}} \prod_{\mathbf{a}} Z_{\mathbf{r}+2\mathbf{a}}$ is the stabilizer of the cluster state.

2.7.3 Erroneous operators on the cluster state

Open measurements on the bond particles, we get

$$\begin{aligned} \mathcal{E}_{\mathbf{r}}^{\text{ghz}} \rightarrow \mathcal{E}_{\mathbf{r}} = & \mathcal{F}[1] + p_z [Z_{\mathbf{r}}] + p_a \sum_{\mathbf{a}} ([Z_{\mathbf{r}+2\mathbf{a}}] + [Z_{\mathbf{r}} Z_{\mathbf{r}+2\mathbf{a}}]) \\ & + p_b \sum_{\mathbf{a}} \sum_{\mathbf{a}' \neq \mathbf{a}} ([Z_{\mathbf{r}+2\mathbf{a}} Z_{\mathbf{r}+2\mathbf{a}'}] + [Z_{\mathbf{r}} Z_{\mathbf{r}+2\mathbf{a}} Z_{\mathbf{r}+2\mathbf{a}'}]) \\ & + p_c \sum_{\mathbf{a}} ([X_{\mathbf{r}} Z_{\mathbf{r}+2\mathbf{a}}] + [X_{\mathbf{r}} Z_{\mathbf{r}} Z_{\mathbf{r}+2\mathbf{a}}]) + p_d ([X_{\mathbf{r}}] + [X_{\mathbf{r}} Z_{\mathbf{r}}]) \end{aligned} \quad (2.49)$$

where similar errors occur with the same probability due to the symmetry of the state.

Because most of qubits in the topological FTQC are measured in the

Chapter 2. Thermal States as Universal Resources for Quantum Computation with Always-on Interactions

X basis, we can neglect X errors. Then,

$$\begin{aligned} \mathcal{E}_{\mathbf{r}} &= (\mathcal{F} + p_d)[1] + (p_z + p_d)[Z_{\mathbf{r}}] \\ &\quad + (p_a + p_c) \sum_{\mathbf{a}} ([Z_{\mathbf{r}+2\mathbf{a}}] + [Z_{\mathbf{r}} Z_{\mathbf{r}+2\mathbf{a}}]) \\ &\quad + p_b \sum_{\mathbf{a}} \sum_{\mathbf{a}' \neq \mathbf{a}} ([Z_{\mathbf{r}+2\mathbf{a}} Z_{\mathbf{r}+2\mathbf{a}'}] + [Z_{\mathbf{r}} Z_{\mathbf{r}+2\mathbf{a}} Z_{\mathbf{r}+2\mathbf{a}'}]). \end{aligned} \quad (2.50)$$

The correlation between qubit- \mathbf{r} and qubit- $(\mathbf{r}+2\mathbf{a})$ can be discarded. Then, $\mathcal{E}_{\mathbf{r}} \cong E_1 \circ E_2$, where

$$E_1 = (1 - p_1)[1] + p_1[Z_{\mathbf{r}}], \quad (2.51)$$

$$E_2 = (1 - p_2 - p_3)[1] + p_2/4 \sum_{\mathbf{a}} [Z_{\mathbf{r}+2\mathbf{a}}] + p_3/6 \sum_{\mathbf{a}, \mathbf{a}'} [Z_{\mathbf{r}+2\mathbf{a}} Z_{\mathbf{r}+2\mathbf{a}'}] \quad (2.52)$$

and $p_1 = p_z + p_a + p_b + p_c + p_d$, $p_2 = 2(p_a + p_c)$, $p_3 = 2p_b$.

2.7.4 Error correction

The resulting error superoperators acting on the yet unmeasured center particles have the following properties: (1) there is one independent error superoperator $\mathcal{E}_{\mathbf{r}}$ for every \mathbf{r} , (2) $\mathcal{E}_{\mathbf{r}}$ acts at the locations \mathbf{r} and $\{\mathbf{r}+2\mathbf{a}, \forall \mathbf{a}\}$, where the center particles are measured in the X -basis for the purpose of topological error correction on the 3D cluster state (in most of the cluster), there arise two further simplifications: (3) All errors are equivalent to Z -errors or the identity, and (4) Correlations between errors on neighbouring center particles can be discarded. The latter arises because errors at \mathbf{r} and at $\mathbf{r}+2\mathbf{a}$ are corrected by different error-correction procedures running independently of another [76, 77].

On the 3D cluster state, for each \mathbf{r} , the resulting error is $\mathcal{E}_{\mathbf{r}} = E_1 \circ E_2$, with $E_1 = (1 - p_1) + p_1[Z_{\mathbf{r}}]$ and $E_2 = (1 - p_2 - p_3) + p_2/4 \sum_{\mathbf{a}} [Z_{\mathbf{r}+2\mathbf{a}}] +$

2.8. MBQC with always-on interactions

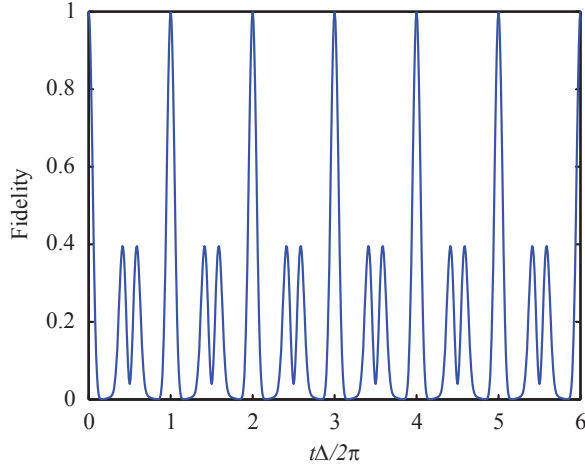


Figure 2.7: The fidelity of the time evolution with always-on interactions for the 3D system. The revival of the fidelity for 6 times, which is required for the MBQC, is demonstrated.

$p_3/6 \sum_{\mathbf{a}, \mathbf{a}'} [Z_{\mathbf{r}+2\mathbf{a}} Z_{\mathbf{r}+2\mathbf{a}'}]$. The error probabilities p_1 , p_2 and p_3 depend on the temperature T . If $p_3 \ll p_1, p_2 \ll 1$, then the local errors are almost independent and the error level is described by an effective local error probability $p \simeq p_1 + p_2 + 2p_3$. Error-correction is possible if $p < 3\%$ [80], which translates into a threshold temperature $T_t = 0.2\Delta$; See Fig. 2.6. At that point, $p_1, p_2 \sim 10^{-2}$ and $p_3 = 10^{-6}$, justifying the assumption of uncorrelated local errors.

On the 2D cluster state, the MBQC is similar to the quantum computing on a one-dimensional architecture [19, 20]. A direct implementation of quantum error correction codes with the MBQC may reduce the threshold with a factor ~ 10 [85, 86]. Error thresholds of the FTQC on one-dimensional architectures are approximately 10^{-5} [87, 45]. Therefore, a reasonable threshold temperature for the 2D system is $T_t \sim 0.06\Delta$.

2.8 MBQC with always-on interactions

For practical application, one can convert the initial state, usually a thermal state, to a cluster state one qubit at a time. Once we need the qubit \mathbf{r} , we can apply POVMs on the center particle \mathbf{r} and its neighbouring center particles $\{\mathbf{r}+2\mathbf{a}\}$. Based on outcomes of POVMs, single-particle operations $U(\hat{\alpha})$ are chosen. Then, bond particles $\{\mathbf{r}+\mathbf{a}\}$ are measured, and outcomes are used to correct the Pauli frame of qubit \mathbf{r} . No further operation is needed on any other particle in order to convert the center particle \mathbf{r} to a qubit on the cluster state.

With always-on interactions, we need to consider the time evolution driven by the time-independent Hamiltonian. Since the initial state is not converted into the cluster state simultaneously, there are some untouched particles. They remain in the initial thermal state, which is close to the ground state due to the existence of the energy gap. Other particles evolve with the Hamiltonian, and their quantum correlations will be changed under time evolution. Fortunately, the time evolution is periodic with a period $4\pi/\Delta$ for the 2D system and $2\pi/\Delta$ for the 3D system. Then, one can perform operations on these particles at the revival time of quantum correlations, $t = 4n\pi/\Delta$ and $t = 2n\pi/\Delta$ for 2D and 3D systems respectively, where $t = 0$ is the time of the first operation on the particle and its interaction particles, and $n = 0, 1, 2, \dots$. If we assume only one operation can be performed on each particle at one revival time, particles can be measured out before $n = 6$. Therefore, the MBQC can be performed on our proposed systems with always-on interactions. Here, operations are required to occur precisely. We remark that errors due to timing imprecision can also be analysed in a similar manner to thermal errors.

In order to validate the periodic revival of the quantum state, we

2.8. MBQC with always-on interactions

consider the time evolution of a subsystem driven by the Hamiltonian $h_{\mathbf{r}}$ in the 3D system. The initial state is supposed to be $|\Psi(0)\rangle = (1/\sqrt{80}) \sum_{l=1}^{80} |\psi_l\rangle \otimes |\bar{\psi}_l\rangle$, where $\{|\psi_l\rangle\}$ is a set of orthonormal states that spans the subsystem corresponding to $h_{\mathbf{r}}$, and $\{|\bar{\psi}_l\rangle\}$ is a set of orthonormal state of an ancillary virtual system. Here, we introduce the ancillary virtual system to investigate the evolution of all possible initial states of the subsystem by considering the evolution of one maximally entangled state. The time evolution of the state reads $|\Psi(t)\rangle = \exp(-ih_{\mathbf{r}} \otimes \bar{\mathbf{I}}t)|\Psi(0)\rangle$, and the fidelity is defined as $f(t) = |\langle\Psi(0)|\Psi(t)\rangle|^2$. Here, $\bar{\mathbf{I}}$ is the identity operator of the ancillary virtual system. At the moment of the recovering of the fidelity, i.e., $f(t) = 1$, the subsystem always evolves back to the initial state independent of what the initial state is. The periodic recovering of the fidelity $f(t)$ is shown in Fig. 2.7.

Fully fault tolerant quantum computation with non-deterministic gates

3.1 Introduction

The field of QIP has witnessed many experimental successes, but the challenge of scaling from a few qubits to large scale devices remains unsolved. One can argue that the issue is so crucial that it may even dictate the choice of fundamental architecture for the machine. In the concept of *distributed* QIP a plurality of small components, each similar in complexity to systems already realised experimentally, are networked together to constitute a full scale machine. The components may be trapped atoms or ions, or solid state nanostructures such as quantum dots or NV centres [24, 88, 89]. Each component can be assumed to be under good control, and it is understood that the key task is then to entangle the physically remote components. An attractive method of achieving this entangling operation (EO) is to arrange for each component to emit a photon that is correlated with the internal state of the component, before performing a joint measurement (with the aid of simple linear optical elements) of the photons. A considerable number of such entanglement schemes have been

Chapter 3. Fully fault tolerant quantum computation with non-deterministic gates

advanced since the initial ideas in 1999 [90, 91]. An important step was the realisation that photon loss can be detected, or heralded, within such a protocol [92, 93]. Generally in these remote entanglement protocols, one is supposed to employ optical measurements that simultaneously observe two, or even four [94], components simultaneously. This principle for generating entanglement has in fact been demonstrated experimentally: first with ensemble systems [95] and subsequently with individual atoms [96]. More about remote EOs can be found in Sec. 3.2.

It is understood that the remote EOs may be failure prone. However, these failures are assumed to be *heralded*: the experimentalist is aware when a failure occurs. The appropriate strategy for dealing with such failures depends on the level of complexity within each component. In the case in which each component incorporates multiple qubits, we can nominate one ‘logical qubit’ and use the rest to make repeated attempts at remote entanglement: if we are eventually successful, we can transfer the entanglement to the logical qubits [97, 98]. However, many physical systems may only have very limited complexity, and moreover it is always desirable to minimise the required complexity. Therefore, it is interesting to consider the case of simply just one qubit in each component. This may be regarded as the extreme limit of the distributed paradigm. If we suppose that the probability p_h of a heralded error is high, perhaps well above 50%, then it is clear that we cannot perform quantum computation by implementing directly a standard circuit model approach. However, it has been shown that even in such heralded failures, arbitrary quantum algorithms can be implemented [93, 92, 99, 100, 101, 102, 103]. These insights are related to earlier ideas on photonic QIP [104, 83]. While such schemes demonstrated that large heralded failure rates can be tolerated,

3.1. Introduction

this was not shown in a fully fault-tolerant manner. In particular, it was not known if large heralded failure rates can be tolerated in the presence of realistic error rates for all other elementary operations.

Fortunately, other studies have developed an approach which can be adapted to present purposes. Recently a series of beautiful results by Raussendorf, Harrington and others described a method for QIP which involves creating a large scale cluster state with a regular three dimensional lattice structure [77, 78]. Defect regions within the 3D lattice are braided together, yielding topologically protected Clifford gates. QIP implemented using this TPC state has a remarkably large tolerance against elementary errors (at rates $\lesssim 1\%$) during preparation, entangling operations and single qubit measurement. Subsequently, two of us have extended this idea to incorporate the possibility that the lattice contains a significant proportion of missing qubits at known locations (nearly 25% can be missing) [79, 105, 106].

In this Chapter, we consider the generation of a TPC state when the entangling operations are themselves subject to heralded failures during the cluster state growth process. The result is a lattice with a certain proportion of known failed entanglement relations (missing ‘edges’ in the graph state). The task of determining a threshold for universal QIP depends on proper choice of growth strategy together with a careful audit of the accumulation of unknown errors in that process. We show how to map this cluster state with missing ‘edges’ to one with missing qubits, thereby making contact with the loss-tolerant thresholds quoted in the prior literature [79, 105, 106].

Several previous papers have considered the task of creating large entangled states when the elementary EO is failure prone (see Fig. 3.1 and

caption). In principle a ‘divide and conquer’ approach can permit the entangled state to have positive growth *on average* for any nonzero success probability $p_s = 1 - p_h$ [92, 93, 99, 100, 101, 102, 103]. Generally the solution involves generating relatively small resource states and subsequently connecting them. As shown in Fig. 3.1(a) the possible ‘building block’ resources include stars [100], linear clusters [92, 99] which in turn give rise to cross structures [101], and tree topologies [107]. The last of these, also called the ‘snowflake’, has been proposed as a optimal choice for minimizing errors [103].

In the present chapter our aim is to synthesise the TPC state (Fig. 3.1b, inset top left). This structure has the property that each node has four neighbours. Therefore we attempt to entangle together each resource with four others, as depicted in Fig. 3.1b). In the particular example illustrated, we see that there will be $N = 4$ attempts to connect to each of the surrounding snowflakes. If one or more of these attempts succeeds, then we have successfully connected the snowflakes, while with probability p_h^N all attempts will fail and the resulting TPC state will have a missing ‘edge’ at that point. These missing edges are known, and are therefore not really regarded as errors but rather as defects which we must allow for in the subsequent computation. Obviously, it will be necessary to create resource objects which are sufficiently large so that this net failure probability is below the threshold for fault tolerant QIP, which we presently discuss. For high values of p_h we will see that the resource states must be considerably larger than those illustrated in Fig. 3.1. We discuss details of generating TPC state in Subsec. 3.3.

3.2. Non-deterministic entangling operations

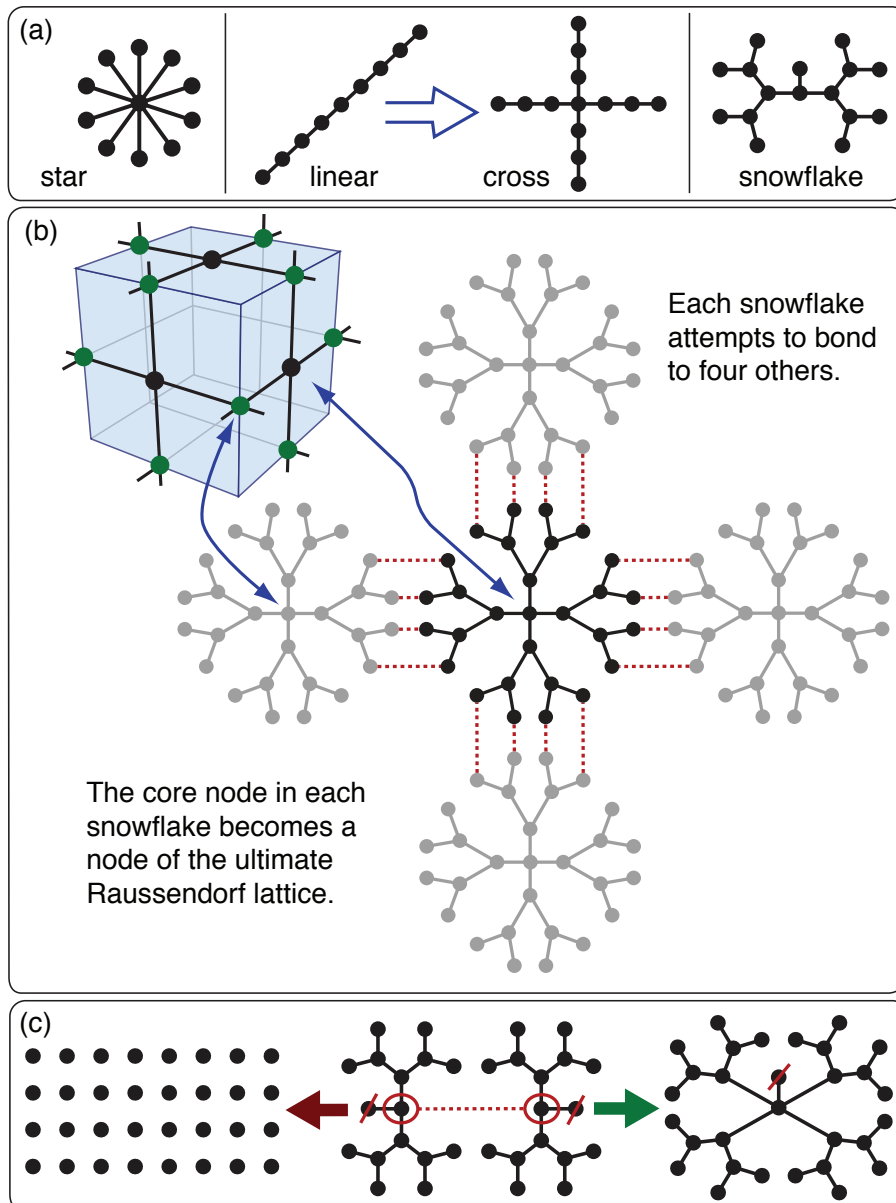


Figure 3.1: The figure shows *graph states*: nodes correspond to qubits, and connections (‘edges’) correspond to phase entanglement. (a) The ‘building block’ resources that have been considered by previous authors. (b) Illustration of how one would synthesise the topologically protected cluster (TPC) state (depicted in upper left) by fusing together snowflake resource objects. One would use a quarter of the structure to bond with each of four adjacent objects; basically the same approach applies for the star or the cross geometries. After the bonding stage, there must be a ‘pruning’ phase where we remove all but the core nodes and thus simplify down to the target lattice. (c) One minor revision in the case of the snowflake is that the final round involves fusing qubits that are one step from the ‘core’ in order to generate a 4-node.

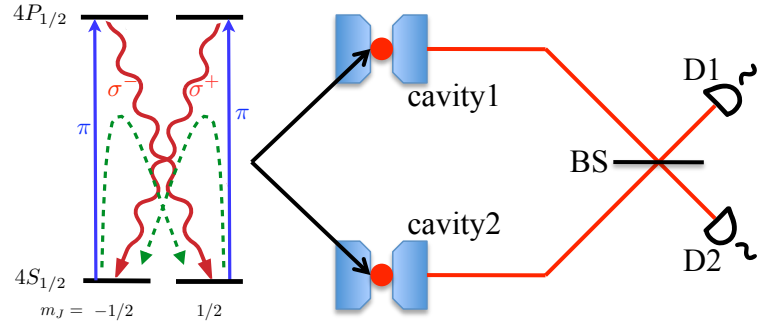


Figure 3.2: An example of probabilistic entangling operations. There is one $^{40}\text{Ca}^+$ atom located in each cavity. Only photons (red wavy lines) with σ^+ or σ^- circular polarizations can decay into the cavity (resonant with $4S_{1/2} \leftrightarrow 4P_{1/2}$). Qubits are encoded in ground-state sublevels $|4S_{1/2}, m_J = \pm 1/2\rangle$. A π -polarized laser (blue lines) resonantly excites both ground-state sublevels $|4S_{1/2}, m_J = \pm 1/2\rangle$ to the $4P_{1/2}$ manifold. The emitted photons (red lines) are entangled with atoms. After a 50/50 beam splitter (BS), photons are detected by single-photon detectors (D1 and D2) to implement the Bell measurement.

3.2 Non-deterministic entangling operations

We are interested in non-deterministic entangling operations, because it can be much easier to implement in a scalable way. Entangling gates are the fundamental of quantum information processing. Usually, an entangling gate corresponds to a unitary evolution driven by interactions between qubits, e.g. entangling gates of two trapped ion qubits can be done through a laser-induced coupling of the spins mediated by a collective mode of harmonic motion in the trap, which is first proposed by I. Cirac and P. Zoller in 1995 [6] and demonstrated in the laboratory later that year [4]. In such a kind of entangling gates, once all operations have been done, one regards that the gate have been done on two qubits successively. Thus, these gates mediated by direct interactions can be called deterministic gates. However, it is hard to coherently control interactions between qubits when they are numerous in order to switch on and off gates. An alternative choice is utilizing entanglements between matter qubits and photonic qubits to

3.2. Non-deterministic entangling operations

achieve an EO between two remote matter qubits. In such cases, one usually performs Bell measurements on two photonic qubits by linear-optic setups [92, 93, 94, 95, 96] (see Fig. 3.2). Bell measurements of photonic qubits with linear optics are intrinsically probabilistic. The maximum success probability of these Bell measurements is $1/2$, due to the maximally probability of distinguishing Bell states with linear optics [108]. Photon loss and inefficiency of photon detectors can further reduce the success probability. The failure of a remote EO can be heralded, which is usually corresponding to an undesired measurement outcome. Therefore, these EOs are non-deterministic. By using non-deterministic EOs, we do not have to coherently control interactions between a lot of qubits, but switch optical connections. On the non-deterministic-EO architecture, each small component can be a trapped ion [23] or a NV center [24].

Non-deterministic EOs can also be non-unitary operations, e.g. the so called parity projection (PP) [98]. The PP can be used to implement universal quantum computation together with single-qubit gates by means of generating a cluster state.

One can entangle a matter qubit with a photonic qubit by exciting the matter qubit to emit a single photon, where the state of the single photon is correlated with the final state of the matter qubit (see Fig. 3.2). We describe the process of entangling a matter qubit with a photonic qubit as

$$|0\rangle_{\text{m}} \rightarrow |0\rangle_{\text{m}} |0\rangle_{\text{p}}, \quad (3.1)$$

$$|1\rangle_{\text{m}} \rightarrow |1\rangle_{\text{m}} |1\rangle_{\text{p}}. \quad (3.2)$$

where $|\psi\rangle_{\text{m}}$ ($|\psi\rangle_{\text{p}}$) is the state of the matter (photonic) qubit. If the initial

state of the matter qubit is $|+\rangle_m$, one gets

$$|+\rangle_m \rightarrow \frac{1}{\sqrt{2}}(|0\rangle_m |0\rangle_p + |1\rangle_m |1\rangle_p), \quad (3.3)$$

where the output state is one of the Bell states, i.e. two qubits are maximally entangled. The process of entangling a matter qubit with a photonic qubit is equivalent to the process of initializing the photonic state in $|0\rangle_p$ followed by a controlled-NOT gate

$$\Lambda_X = \frac{1 + Z_m}{2} + \frac{1 - Z_m}{2} X_p. \quad (3.4)$$

The matrix representation of the controlled-NOT gate is

$$\Lambda_X = \begin{pmatrix} 1 & 0 & 0 & 0 \\ 0 & 1 & 0 & 0 \\ 0 & 0 & 0 & 1 \\ 0 & 0 & 1 & 0 \end{pmatrix} \quad (3.5)$$

in the basis $\{|0\rangle_m |0\rangle_p, |0\rangle_m |1\rangle_p, |1\rangle_m |0\rangle_p, |1\rangle_m |1\rangle_p\}$.

In general, the initial state of two matter qubits can be written as $|\psi\rangle_{m1} |\phi\rangle_{m2}$. After emitting photons, we get the state

$$\sum_{\rho, \sigma=0,1} \frac{1 + i^{2\rho} Z_{m1}}{2} \frac{1 + i^{2\sigma} Z_{m2}}{2} |\psi\rangle_{m1} |\phi\rangle_{m2} |\rho\rangle_{p1} |\sigma\rangle_{p2}. \quad (3.6)$$

One can perform Bell measurement on two photonic qubits. We write Bell states as

$$|\mu, \nu\rangle_{p1, p2} = \frac{1}{\sqrt{2}}(|0\rangle_{p1} |\mu\rangle_{p2} + i^{2\nu} |1\rangle_{p1} |1 \oplus \mu\rangle_{p2}), \quad (3.7)$$

3.2. Non-deterministic entangling operations

where $x \oplus y = (x + y) \bmod 2$. If the outcome of the Bell measurement is $|\mu, \nu\rangle_{p1, p2}$, the output state of two matter qubits is

$$\begin{aligned} & \frac{1}{\sqrt{2}} \sum_{\rho=0,1} \frac{1 + i^{2\rho} Z_{m1}}{2} \frac{1 + i^{2\rho \oplus \mu} Z_{m2}}{2} i^{2\nu\rho} |\psi\rangle_{m1} |\phi\rangle_{m2} \\ &= \frac{1}{\sqrt{2}} Z_{m1}^\nu \left(\frac{1 + Z_{m1}}{2} \frac{1 + i^{2\mu} Z_{m2}}{2} + \frac{1 - Z_{m1}}{2} \frac{1 - i^{2\mu} Z_{m2}}{2} \right) |\psi\rangle_{m1} |\phi\rangle_{m2}. \end{aligned} \quad (3.8)$$

After a single-qubit operation Z_{m1}^ν , one can obtain the operation

$$P_\mu = \frac{1 + Z_{m1}}{2} \frac{1 + i^{2\mu} Z_{m2}}{2} + \frac{1 - Z_{m1}}{2} \frac{1 - i^{2\mu} Z_{m2}}{2}, \quad (3.9)$$

which is a parity projection (PP). Note that, P_0 projects the state into the subspace $\{|0\rangle_{m1} |0\rangle_{m2}, |1\rangle_{m1} |1\rangle_{m2}\}$ and P_1 projects the state into the subspace $\{|0\rangle_{m1} |1\rangle_{m2}, |1\rangle_{m1} |0\rangle_{m2}\}$.

In order to obtain a remote controlled-phase gate, one has to perform a single-qubit gate $e^{-iY_{p2}\pi/4}$ prior to the Bell measurement, i.e. perform the Bell measurement in the basis

$$|\widetilde{\mu}, \widetilde{\nu}\rangle_{p1, p2} = \frac{1}{2} \sum_{\rho, \sigma=0,1} i^{2\nu\rho} i^{2\mu\sigma} i^{2\rho\sigma} |\rho\rangle_{p1} |\sigma\rangle_{p2}. \quad (3.10)$$

If the outcome of the Bell measurement is $|\widetilde{\mu}, \widetilde{\nu}\rangle_{p1, p2}$, the output state of the two matter qubits is

$$\begin{aligned} & \frac{1}{2} \sum_{\rho, \sigma=0,1} \frac{1 + i^{2\rho} Z_{m1}}{2} \frac{1 + i^{2\sigma} Z_{m2}}{2} i^{2\nu\rho} i^{2\mu\sigma} i^{2\rho\sigma} |\psi\rangle_{m1} |\phi\rangle_{m2} \\ &= \frac{1}{2} Z_{m1}^\nu Z_{m2}^\mu \sum_{\rho, \sigma=0,1} \frac{1 + i^{2\rho} Z_{m1}}{2} \frac{1 + i^{2\sigma} Z_{m2}}{2} i^{2\rho\sigma} |\psi\rangle_{m1} |\phi\rangle_{m2} \\ &= \frac{1}{4} Z_{m1}^\nu Z_{m2}^\mu (1 + Z_{m1} + Z_{m2} - Z_{m1} Z_{m2}) |\psi\rangle_{m1} |\phi\rangle_{m2}. \end{aligned} \quad (3.11)$$

After the single-qubit operation $Z_{m1}^\nu Z_{m2}^\mu$ and neglecting a factor $1/2$, one

obtains the controlled-phase gate

$$\Lambda_Z = \frac{1}{2}(1 + Z_{m1} + Z_{m2} - Z_{m1}Z_{m2}). \quad (3.12)$$

If the measurement outcome of two photons is not one of Bell states or if one of two photons is missing, the EO is failed. In this case, the matter qubits are projected into a wrong state, losing their information into the environment. If the EO failed, one has to initialize the two matter qubits in order to protect other qubits that are entangled with these two qubits.

3.3 Growth of cluster states

Non-deterministic EOs can be used to perform universal quantum computing. However, it is not a good idea to replace entangling gates with non-deterministic EOs directly. The overall success probability may decrease exponentially with the total number of EOs if they are non-deterministic. Another idea is the generation of a cluster state with non-deterministic EOs and utilizing the cluster state subsequently to perform MBQC. In this section, we will review how to grow such a cluster state with non-deterministic EOs.

One can use non-deterministic controlled-phase gates to generate a cluster state directly, in which some of qubits and edges may be missing due to the failure of some EOs. If the success probability is high enough, even if the cluster state is not perfect, it is sufficiently connected and can be used for universal MBQC. The threshold success probability is given by percolation theory [109, 110], which depends on the geometry of the lattice of the cluster state. However, the threshold is usually too high for non-deterministic EOs. A possible solution to this problem is to prepare some

3.3. Growth of cluster states

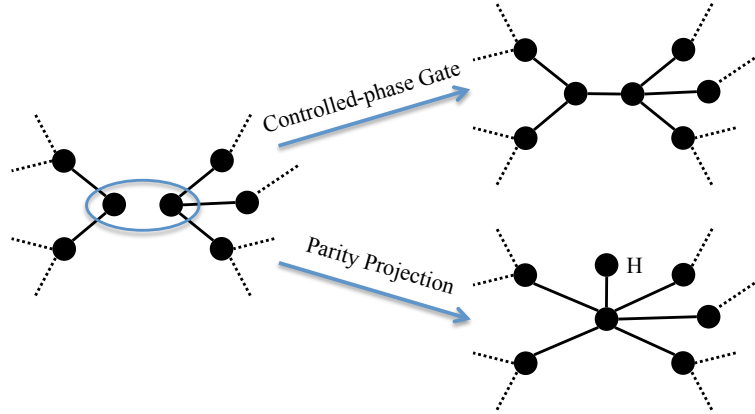


Figure 3.3: Entangling operations (EOs) on a graph state. The EO is performed on two qubits in the circle. A controlled-phase gate adds a new edge on the graph state. A parity projection as well as a Hadamard gate on one of those two qubits in the circle change the graph state as the following: qubits which are used to be connected with one of those two qubits and the qubit with a Hadamard gate are all connected with the qubit without a Hadamard gate in the new graph state.

resource graph states initially, and then connect the resource graph states into a well-connected cluster state for universal MBQC.

Before we show proposals of generating these resource graph states and how to connect them together, we would like to discuss how to manipulate graph states with EOs. We focus on two kinds of EOs, the PP and the controlled-phase gate. A successful non-deterministic controlled-phase gate acts like a normal controlled-phase gate adding an edge on a graph state as shown in Fig. 3.3. A successful PP, e.g. P_0 , projects two qubits into one qubit encoded as $\{|00\rangle, |11\rangle\}$. Then, we perform a Hadamard gate on one of these two qubits. As a result, the two qubits are entangled as a part of the new graph state in the form, $\{|0+\rangle, |1-\rangle\}$. All qubits connected with one of those two qubits on the original graph state and the qubit with a Hadamard gate are connected to the qubit without a Hadamard gate [24], as shown in Fig. 3.3. In the following sections, we would like to use ‘PP’ to represent the PP as well as the Hadamard gate. The P_1 is equivalent

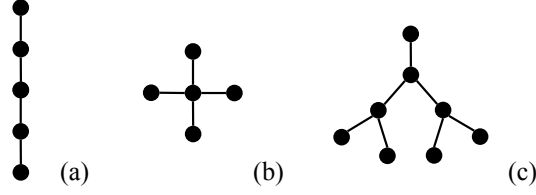


Figure 3.4: Resource graph states with (a) the line structure, (b) the star structure and (c) the tree structure.

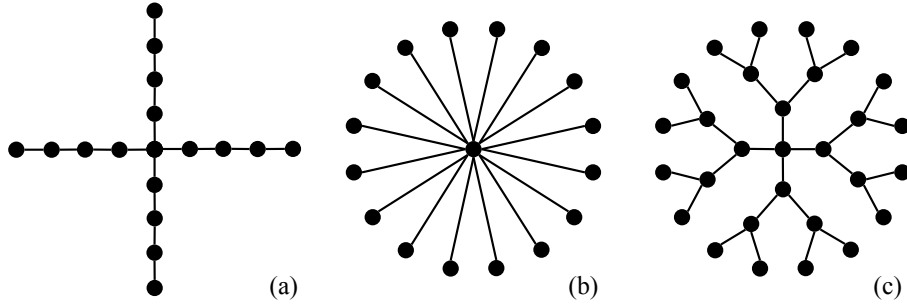


Figure 3.5: Building-block graph states with (a) the cross structure, (b) the star structure and (c) the snowflake structure.

to the P_0 up to a local gate. If an EO failed, the two corresponding qubits need to be initialized.

Resource graph states may have a line structure [101, 92, 99], a star structure [100] or a tree structure [107, 103, 111] as shown in the Fig. 3.4. Line graph states are prepared using controlled-phase gates efficiently, while star graph states and tree graph states are prepared using PP efficiently. These resource graph states are then connected into some building-block graph states, which can be used for growing a cluster state directly. In Fig. 3.5, we show examples of cross graph states, bigger star graph states and snowflake graph states respectively. In each case, the intent is to create a four-fold symmetric object, with a common core attached to each quarter of the structure.

For the cross geometry, we form large linear sections by repeatedly joining two matched pairs of smaller linear units. The long sections will

3.3. Growth of cluster states

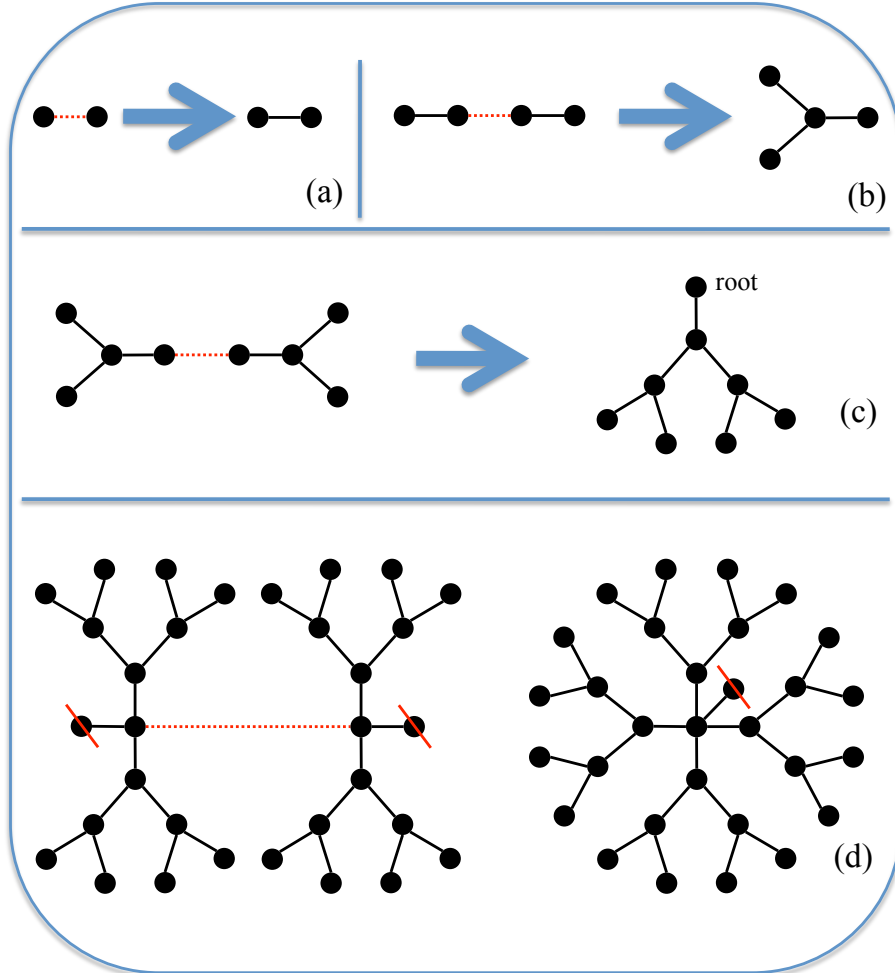


Figure 3.6: The strategy for generating tree graph states and connecting them into snowflake graph states. Each red dot line represents a parity projection (PP). (a) Two qubits initialized in $|+\rangle$ can be entangled after a PP. (b) A PP between two pairs of entangled qubit can merge them into a star graph states. (c) After a PP on edge qubits of two four-qubit star graph states, one can get a tree graph state. The qubit with the Hadamard gate is called the root qubit. By PPs on root qubits, one can grow tree graph states into bigger tree graph states, and the size of tree graph states goes up exponentially with the generation of these trees. (d) By a PP on two qubits connected with root qubits, one can merge two tree graph states into a snowflake graph state, after removing unwanted qubits by measurements in the Z basis. Once a PP fails, the corresponding graph states have to be abandoned and all qubits have to be initialized.

therefore be a power of two in total number of qubits. Two linear sections can be combined into a cross as described in Ref[101]. Finally we remove two further qubits so that the graph is four-fold symmetric.

For the case of the star geometry, it is more straightforward: whenever a pair of small stars are fused by a successful parity projection operation, the result is a new star. The total number of qubits in any star is a power of two. Since one qubit must act as the core, the number of satellites are not divisible by four. Therefore in the final step we remove three satellite qubits with Z measurements, and achieve the required four-fold symmetry (this is a convenience for the calculation and need not be performed in practice; the result would be a very slight improvement to the threshold).

We illustrate how to generate a tree graph state, and how to connect them into a snowflake as an example in Fig. 3.6. Tree graph states can also be used for other kind of building-block graph states [103, 107].

Making a building-block graph state requires all operations to be successful, even if the probability may be quite small. Therefore, building-block graph states are produced with a post selection strategy: if an operation is heralded as failed, the corresponding graph state is abandoned with the qubits re-initialized. One can always obtain enough building-blocks with enough trials since these building blocks are executed in parallel.

Each building-block graph state is corresponding to a qubit on the final graph state. After building-block graph states are prepared, these graph states are assembled by EOs as shown in Fig. 3.7 for example. If the total number of EOs used for connecting two building-block graph states is N , and the failure probability of EOs is p_f , then the probability of connecting two building-block graph states is $1 - p_f^N$. As soon as a connection (a success path) is established successfully between two central qubits of building-

3.3. Growth of cluster states

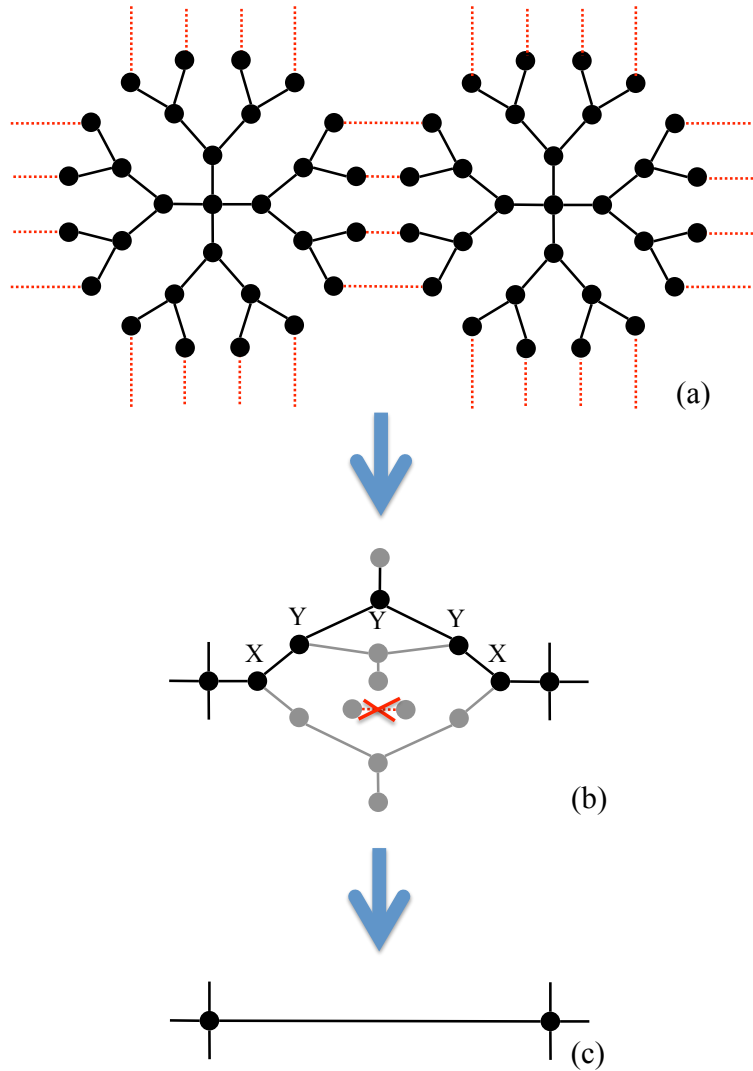


Figure 3.7: The strategy for assembling building-block graph states, e.g. snowflake graph states, into a universal resource of MBQC. (a) Building-block graph states are connected by EOs, e.g. PPs denoted as red dot lines. (b) Once two building-block graph states are connected, we chose one success path between two central qubits (two cores), and other qubits (gray) are measured in the Z basis. (c) Qubits on the success path are measured in basis as shown in the figure (b). Then, a direct connection is established between two central qubits. Some of EOs for connecting two building-block graph states may be failed (the red cross), but it is unlikely to happen that all EOs are failed if building-block graph states are big enough. If all EOs for connecting two building-block graph states are failed, two building-block graph states are failed to be connected, which is corresponding to a missing connection between two corresponding qubits on the final cluster state.

block graph states, we transform such a path to a direct connection between two central qubits by performing measurements on the redundant qubits. As a result, one obtains a cluster state with missing connections, and the probability of missing connections is p_f^N . The missing connections can be mapped to missing qubits by measuring qubits with missing connections in the computational basis. Because cluster states can tolerate qubit loss with a probability up to a threshold value predicted by the percolation theory [109, 110], the obtained cluster state is a universal resource state of the MBQC if building-block graph states are big enough.

The protocol of growing a cluster state with building-block graph states is efficient in the sense that the cost of time and the cost of qubits for generating one building block are independent of the size of the cluster state. We suppose that $T(N)$ steps are required for preparing a building block if EOs are performed in parallel and all successful, $Q(N)$ is the number of qubits in one building block, and $E(N)$ is the number of EOs that have to be performed for generating one building block. Here, $T(N)$, $Q(N)$, and $E(N)$ depend on the size of the building block N , which is independent of the size of the cluster state. Then, the time cost for growing the cluster state is $\sim T(N)$, the probability of successfully preparing one snowflake is $(1 - p)^{E(N)}$, and on average one can generate one snowflake with $\sim (1 - p)^{-E(N)}Q(N)$ qubits, which means $\sim (1 - p)^{-E(N)}$ trials are executed in parallel. Because the overhead $\sim T(N)$ and $\sim (1 - p)^{-E(N)}Q(N)$ are independent of the size of the cluster state, the speedup of the quantum computing is still valid in the scaling limit.

3.4 Error model

To evaluate the error in the scheme, it is essential to determine the accumulation of *unknown* errors when we use the star, cross, and snowflake graph states. These errors will inevitably occur during the growth process of the resource, the fusion of resources, and also the removal of redundant qubits to the TPC state. In order to minimise error accumulation during the growth process we make the aggressive choice that *whenever* there is a known failure during the growth of the resource object, the entire resource object is abandoned. Fortunately all three of the resources considered – star, cross, snowflake – can be grown through a series of steps each of which (on success) doubles the entity’s size. Thus the process is quick in the sense that it requires a number of successful steps that is merely a logarithmic function of the target resource size. Both operations are known to be possible through suitable measurements on emitted photons [93, 92, 99].

We consider various forms of errors. Single-qubit errors may occur during preparation, or while performing a single-qubit rotation, or during the measurement process (see Eq. 2.8). Moreover these errors may also occur passively in memory, i.e. there is a rate at which qubits decohere even when they are not part of any active operation. Meanwhile two-qubit errors may occur when we perform entanglement operations (see Eq. 2.9). We also need to account for imperfections both in the emission of photons (e.g. from an imperfect selection rule in an atomic system, say) and errors arising from imperfect measurement of emitted photons. Different probabilities are assigned to the various errors, however, for simplicity in generating the diagrams here we set the rates for all forms of the active ‘gate’ errors to be equal and we denote their probability p_G . Memory errors are considered separately later in the paper.

Noisy single-qubit operations are perfect operations combined with single-qubit errors. The probabilities of a preparation error, a single-qubit gate error and a single-qubit measurement error are p_P , p_S and p_M respectively. Entangling operations (EOs) are used to entangle two separate graph states into a new graph state. We decompose an EO as: (1) each qubit emits a photon; (2) suitable measurement is performed on the two photons. After the emission of a photon, both the pair of photon and the pair of matter qubits may suffer a two-qubit error. Before the Bell measurement, a two-qubit error may occur on the two photons. The total probability of a two-qubit error occurring during the EO is p_E .

In this chapter, we have assumed that all active errors (that is, errors resulting from a deliberate operation on the system) are equally probable, i.e. $p_P = p_S = p_M = p_E = p_A$.

Separately, we consider passive errors: each qubit bears a single-qubit error with probability $p_{P.E.}$ during the period of one operation.

3.5 Error propagation

In order to calculate the rate at which unknown errors occur on the final TPC state, we have to trace carefully the propagation of original low level errors. First, we transform all errors on a graph state to Z errors by

$$X_a \longrightarrow \prod_{b \in N(a)} Z_b, \quad Y_a \longrightarrow Z_a \prod_{b \in N(a)} Z_b. \quad (3.13)$$

After a single-qubit measurement, we need some single-qubit gates to return the remaining entangled state to the graph state form [75]. While these gates may be postponed they must eventually be accounted for. An error in the original measurement leading to a wrongly recorded outcome, means

3.6. Error accumulation

basis	error propagation
Z_a	$Z_a \rightarrow Z_a, Z_{c \neq a} \rightarrow Z_c$
X_a	$Z_a \rightarrow Z_{b_0} \prod_{d \in N(b_0) - a} Z_d, Z_{b_0} \rightarrow \prod_{d \in N(a) - b_0} Z_d, Z_{c \neq a, b_0} \rightarrow Z_c$
Y_a	$Z_a \rightarrow \prod_{b \in N(a)} Z_b, Z_{c \neq a} \rightarrow Z_c$

Table 3.1: Error propagation of single-qubit measurements. Single-qubit measurements are performed on the qubit- a . b_0 is a qubit in the set $N(a)$.

CPG	$Z_1 \rightarrow Z_1, Z_2 \rightarrow Z_2,$
PP	$Z_1 \rightarrow Z_1, Z_2 \rightarrow Z_1,$

Table 3.2: Error propagation of EOs. EOs, which may be controlled-phase gates (CPGs) or PPs, are performed on the qubit-1 and qubit-2, where $N(1) \cap N(2) = \emptyset$.

subsequent incorrect single-qubit gate(s). Moreover the single-qubit gate itself can transform errors. Generally single-qubit measurements propagate errors as shown in Table 3.1. We consider both phase gate (PG) and parity projection (PP), as shown in Fig 3.3. EOs propagate errors as shown in Table 3.2.

3.6 Error accumulation

We can rewrite erroneous operations as

$$\begin{aligned}
 e_1 &= (1 - q_1 + q_1[X]) \circ (1 - q_1 + q_1[Y]) \\
 &\quad \circ (1 - q_1 + q_1[Z])
 \end{aligned} \tag{3.14}$$

and

$$\begin{aligned}
 e_2 &= (1 - q_2 + q_2[IX]) \circ \cdots \circ (1 - q_2 + q_2[ZI]) \\
 &\quad \circ \cdots \circ (1 - q_2 + q_2[XY]).
 \end{aligned} \tag{3.15}$$

Chapter 3. Fully fault tolerant quantum computation with non-deterministic gates

When $p_1, p_2 \ll 1$,

$$q_1 \simeq \frac{p_1}{3}, q_2 \simeq \frac{p_2}{15}. \quad (3.16)$$

An error generated on qubit- x at time t , which will be propagated to a final error Σ , is an error channel of Σ . Then, the final error operation can be written as

$$E = \prod_c (1 - q_c + q_c[\Sigma]) = (1 - P) + P[\Sigma], \quad (3.17)$$

where $c = (x, t)$ are error channels and q_c are corresponding probabilities. Here, $\Sigma^2 = 1$. Therefore,

$$E = \left[\prod_c (1 - q_c) + O(q^2) \right] + \left[\sum_{c_1} q_{c_1} \prod_{c \neq c_1} (1 - q_c) + O(q^3) \right] [\Sigma]. \quad (3.18)$$

Then,

$$P = \sum_{c_1} q_{c_1} - \sum_{c_1} \sum_{c \neq c_1} q_{c_1} q_c + O(q^3). \quad (3.19)$$

When $q_c \ll C^{-1}$, where C is the number of error channels,

$$P \simeq \sum_c q_c. \quad (3.20)$$

For the star scheme and the cross scheme, the final error probability associated with the bond between two qubits on the final TPC state depends on details of how that successful connection was accomplished. For example in the cross strategy, if a bond between two ‘arms’ is accomplished early, this leads to a different error probability from a late success (each failure shortens the arm sections). To obtain a single error rate we must average over the possible success scenarios. We set p_j is the probability of

3.7. Final errors on the topologically protected cluster state

scenario- j . If the final error corresponding to scenario- j is

$$E_j = 1 - P_j + P_j[\Sigma], \quad (3.21)$$

the average final error

$$\bar{E} = \sum_j p_j E_j = 1 - \bar{P} + \bar{P}[\Sigma], \quad (3.22)$$

where

$$\bar{P} = \sum_j p_j P_j. \quad (3.23)$$

3.7 Final errors on the topologically protected cluster state

The numbers of error channels depend on missing bonds between qubits on the TPC state. However, we will delete qubits with missing bonds. Therefore, we will only consider final errors on qubits without missing bond. Table 3.3 shows the various kinds of low-level error along with the resulting high level error on the TPC state, along with the number of channels by which this may occur.

The TPC state consists of two interlaced sublattices, i.e. the primal qubits and dual qubits (see Sec. 2.3). Because error corrections in the two sublattices are separable [76], we can neglect error correlations *between* the two sublattices. As an example, an error channel of $Z_0 Z_i$ is equivalent to an error channel of Z_0 , for the error correction of sublattice containing qubit-0.

We must still consider the possibility of correlated errors *within* a given sublattice, but these are rare. On the final TPC state, if we neglect passive

**Chapter 3. Fully fault tolerant quantum computation with
non-deterministic gates**

Error source	Final error	Channel number
preparation, single-qubit gate and measurement	Z_0	$24n + 16$
	$X_0 \& Y_0$	2
EO	Z_0	$192n + 134$
	$X_0 \& Y_0$	2
	$Z_0 Z_i$	$16n + 32$
	$Z_1 Z_2 \& Z_0 Z_1 Z_2$	4
	$Z_3 Z_4 \& Z_0 Z_3 Z_4$	12
passive errors	Z_0	$8n^2 + 80n - 13$
	$X_0 \& Y_0$	3
	$Z_0 Z_i$	$4n + 4$
	$Z_1 Z_2 \& Z_0 Z_1 Z_2$	1
	$Z_3 Z_4 \& Z_0 Z_3 Z_4$	1

Table 3.3: Relating low level errors in the snowflake approach to the resulting high level errors on the TPC state, and tracking the number of channels by which such errors can occur. The qubit-0 is connected with qubit- i , where $i = 1, 2, 3, 4$. Here $n = \log_2(\text{quarter of size})$.

errors, the probability of $Z_1 Z_2$ is $8p_A/15$, the probability of $Z_3 Z_4$ is $8p_A/5$, the probability of X_0 is $8p_A/5$, and the probability of Z_0 is $P = Rp_A$, where the ratio R depends on the size of original graph states. For the snowflake scheme, after counting the number of error channels as shown in Table 3.3, we have

$$R = \frac{376}{15}n + \frac{74}{3}. \quad (3.24)$$

Here $n = \log_2(\text{quarter of size})$. The ratio R of star and cross schemes were found numerically and are shown in Fig. 3.8. Note that for all schemes, $R \gg 1$, i.e. Z_0 errors are overwhelmingly more probable than the harmful forms of correlated error. This is because all errors generated during the preparation of one quarter of building blocks are propagated to single-qubit errors on nodes.

The thresholds of topological error correction scheme are characterized by a contour in (p_{loss}, p_{comp}) parameter space [105, 79, 106]. The computational error threshold of a graph state without missing bond is 2.93%

3.8. Error correction

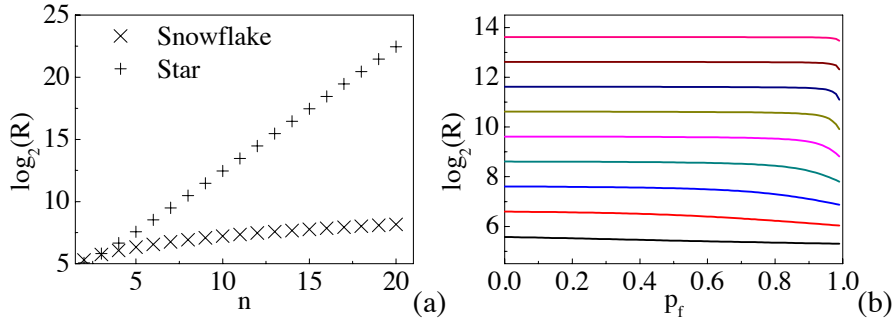


Figure 3.8: Ratio R of (a) snowflake and star schemes, (b) cross scheme, where $n = 2, 3, \dots, 10$ from bottom to top.

for single-qubit errors [76]. Therefore, the critical line is almost a straight line between $(0, 2.93\%)$ and $(24.9\%, 0)$ (Eq. 2.9). The relation between the probability of qubit loss and the probability of missing bond (failure probability) is $p_{loss} = 1 - (1 - P_F)^4$.

3.8 Error correction

A principle conclusion from our analysis of error propagation is that two-qubit errors occurring during the growth and fusion of resource objects (e.g. snowflakes) typically appear as single qubit errors in the eventual TPC state. While there are instances where a two-qubit error can affect the final lattice, the majority of these involve one qubit from the prime lattice and one from the dual, i.e. the black and green qubits in Fig. 3.1b. Such correlations do not affect the fault tolerance threshold, because errors on two sublattices are corrected independently. There will be occasional instances of errors between two qubits both within the prime lattice, or both within the dual. However these are rare – for example in the case where one uses the snowflake strategy with $p_h = 0.9$, the rate for these errors is two orders of magnitude lower than the corresponding rate of single-qubit errors on the TPC state (given equal rates for the various forms of error during

growth). In this case, two qubit errors only weakly affect the threshold, so as an approximation we can ignore such events and assume that all gate errors affect at most one qubit in each sub lattice. Thus we consider a lattice with a (low) rate of random single qubit errors, and a (relatively high) portion of missing ‘edges’ which are known. We need to determine the threshold for such a lattice to support computation. Fortunately, our previous work has considered the closely related case of a lattice with a significant number of missing *nodes*. We need only map the case of missing edges to that of missing nodes in order to make contact with that analysis and thus obtain thresholds in the present case.

We consider the standard TPC state, specifically neighbouring qubits i (in the primal lattice) and j (in the dual lattice). Each qubit is centred on a face of its respective sublattice, and each qubit is a member of two cubic unit cells of the sublattice. In the ideal case where no bonds are missing, the product of cluster stabilisers associated with the faces of each cubic unit cell is simply the product of X operators acting on the respective face-centred qubits, yielding two parity-check operators associated with each qubit: $P_i^{1,2}$ for qubit i and $P_j^{1,2}$ for qubit j . Since these ideal parity check operators are just products of X operators on each face of the corresponding cube, they commute point wise, which enables the error syndrome to be determined by single particle X measurements [77, 78].

In the case where the bond between qubits i and j is missing, the cluster stabilisers associated with the missing bond are modified. Then, the product of cluster stabilisers centered on the cubic unit cell faces yields damaged parity check operators $\hat{P}_i^{1,2} = P_i^{1,2} Z_j$ and $\hat{P}_j^{1,2} = P_j^{1,2} Z_i$. Whilst $\hat{P}_i^{1,2}$ and $\hat{P}_j^{1,2}$ commute, they do not commute point-wise (since $[X_i, Z_j] \neq 0$). In contrast to the ideal case, this means that determining the syndrome

3.9. Phase diagrams of error correction

on the primal and dual lattices apparently requires measurement of the two-qubit operators $X_i Z_j$ and $Z_i X_j$.

Fortunately, by simply treating the qubits i and j at each end of the missing bond as though they were lost, and adopting the strategy in [105, 79, 106], we form products of the damaged parity check operators, yielding *super-check* operators $\tilde{P}_i = \hat{P}_i^1 \hat{P}_i^2 = P_i^1 P_i^2$ and $\tilde{P}_j = \hat{P}_j^1 \hat{P}_j^2 = P_j^1 P_j^2$. These new operators are independent of the qubits i and j , so they are unaffected by the missing bond between them. Furthermore each super-check operator involves only products of X operators from a single sublattice, so a missing bond manifests itself as a single missing qubit on each sublattice. This establishes a correspondence between missing bonds and correlated losses of neighbouring qubits. Error correction is then realised by implementing the loss-tolerant, error-correcting protocol of two each sublattice independently.

3.9 Phase diagrams of error correction

Having made the connection to prior work on thresholds for the TPC state, we can now take any set of parameters for the low-level operations on qubits in the distributed machine, compute the effective qubit loss rate, and determine whether quantum computation is possible. In Fig. 3.9 we show this phase diagram under the assumption that all gate error rates are equal. We see that very high rates of heralded error can be tolerated, provided that the rate for unknown errors is below 2×10^{-4} . This is certainly a difficult number to achieve but might be possible in some implementations, e.g. trapped ions for which multi-qubit measurements with fidelity around this rate have already been demonstrated [112].

It remains to consider memory errors, which we assume happen at a lower rate than gate errors. In Fig. 3.10a we show the effect of ‘switching

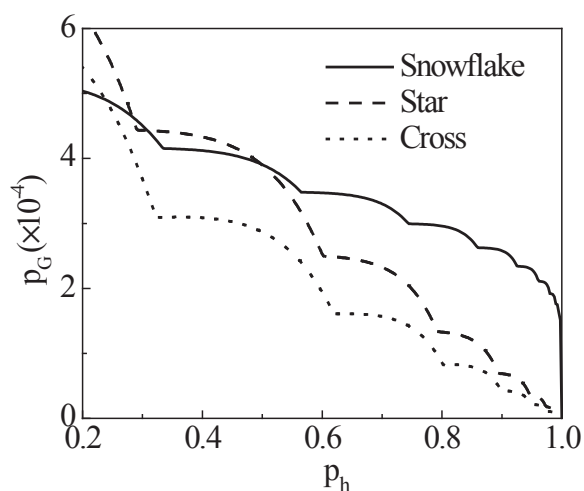


Figure 3.9: The principle results of our analysis. The lines define the parameter regimes where fault tolerant QIP is possible. Here for simplicity we set all gate errors, including both single-qubit and two-qubit errors, to be equally likely. This probability is denoted p_G and is plotted on the vertical axis. (Memory errors due to gradual decoherence are excluded, and are shown in Fig. 3.10). Meanwhile, the probability p_h of an entanglement operation failing in a heralded fashion is plotted on the horizontal axis. Note that p_h can be very high, exceeding 90% if the snowflake strategy is employed.

3.9. Phase diagrams of error correction

on' memory errors at a level equal to one tenth of the gate error rate. As one might expect, this lowers the overall threshold, but not dramatically.

Finally we consider the question of physical resource scaling. From Fig. 3.9 one might be tempted to conclude that QIP is possible with *extremely* high rates of heralded error, perhaps reaching 99% or more. However, such a conclusion would neglect the ever increasing costs of preparing the resource objects. These objects become very large as p_h approaches unity. In Fig. 3.10b we see that if p_h exceeds 0.98, the size of each snowflake must be several thousand qubits. Recall that each snowflake ultimately corresponds to a single qubit in the TPC state, and therefore this factor would multiply the overhead already implicit in that approach. However, values in the range of $p_h \approx 0.9$ may be tenable for technologies where the individual components of the distributed computer can be mass produced.

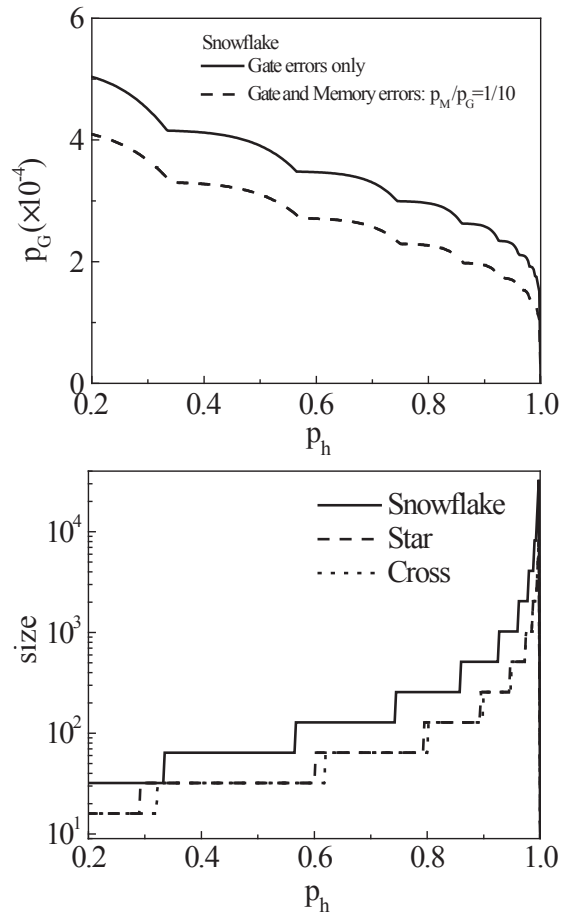


Figure 3.10: (a) The effect of introducing memory errors, i.e. finite gradual decoherence. (b) The size of the resource objects required to achieve the thresholds.

High threshold distributed quantum computing with three-qubit nodes

4.1 Introduction

Over the last two decades a remarkable range of physical systems have been shown to support the key elements required for quantum computation: robust qubits, controlled single qubit gates and measurements, and entangling operations. However these successes have involved relatively few qubits in any given device. It remains to be seen whether the high fidelity operations and low decoherence rates that have been achieved in small systems can be replicated in vastly more complex arrays of thousands, or millions of qubits. There is however an attractive alternative approach to creating monolithic arrays, namely *distributed quantum computing* (DQC): one can form a network of small devices or ‘nodes’, such that nodes are well separated and therefore each can have dedicated control and measurement systems similar to those that have already been achieved. The challenge is to entangle the ‘remote’ systems (remote here meaning well separated but still part of the same physical device). Experiments with atoms [96] and atomic ensembles [95] have shown that two remote quantum entities

Chapter 4. High threshold distributed quantum computing with three-qubit nodes

can undergo an EO when light emitted (or potentially emitted) from the structures is suitably measured, and solid state demonstrations may soon follow [113]. Generally the network EO may be of low fidelity and may fail outright much of the time, and this must be accounted for in practical DQC schemes.

All DQC schemes of which we are aware, and certainly the schemes in this Chapter, make the assumption that (at least) one qubit in each node is directly operated upon by the network EO. Typically it is presumed that the basic EO involves only two nodes at a time (although schemes for entangling multiple nodes in one step have been advanced [94, 114]). However one assumes that multiple such pairings can be attempted simultaneously, i.e. there is parallelism in the overall architecture. When a network EO fails, the corresponding qubit in each of the two nodes will be corrupted. Here we will not need to specify further physical details of the EO process; it may involve ‘path erasure’ techniques [92, 93, 23] or alternatively continuous variable mediators as in the ‘qubus’ [115] approach, or other alternatives. We require only that there is a channel by which entanglement, possibly of low quality, can be generated between nodes.

The robustness to errors in DQC architectures is highly dependent on the size of the nodes: nodes with a higher number of qubits can support more complex error suppression techniques. On the other hand, it is desirable to minimise the number of qubits per node in order to reduce the experimental challenge and support the widest range of physical implementations. In the following we will write DQC- N to refer to schemes for distributed QIP involving nodes with N qubits. Note that the acronym DQC1 has been used in the literature relating to the ‘power of one pure qubit’ but this is not the meaning intended here.

4.2 The states of the art

DQC-1, i.e. networked QIP with only one qubit per node, is in principle possible. In that case one finds that the rate of unknown errors in the network EO must be low if the overall device is to support scalable QIP, however one can at least tolerate a high rate of known (‘heralded’) failures: 90% according to Refs. [111] (see Chapter 3) and [116] given resource overhead of the order of a factor of a thousand. This overhead is required because each EO failure damages the effort to create large scale entanglement, necessitating massive redundancy.

In DQC-2, the two qubits can be purposed for different tasks: one qubit in each node to be used in the network EO, and one qubit to build up multi-qubit entanglement with other nodes. By separating these tasks, we at least gain the advantage that heralded failures in the EO can simply be repeated without the cost of losing previously achieved entanglement. The term “broker” has been used for the qubit that is involved in the raw network EO, while “client” refers to the qubit that receives the successful entanglement from the broker [98]. While the broker/client model allows one to absorb heralded failures without the massive overhead of DQC-1, the node size is still too small to be useful in removing general noise (i.e. unknown errors) on the internode entanglement. Thus, the fidelity of successful EOs must still be high in order to support full scale QIP (strictly speaking, we cannot handle *full rank* noise, however if for example the noise is primarily phase noise, then strategies are available – we return to this point later).

While DQC-1 and DQC-2 can support full scale QIP, practically is desirable to have a sufficiently complex node to purify arbitrary noise on the network EO. One can then support physical systems where the EO fidelity

is far below the levels required for conventional fault tolerant QIP. In 2003 Briegel and Dür showed that entanglement purification can be efficiently performed with a limited number of ancilla qubits; they considered DQC-3, DQC-4 and DQC-5 [97]. This seminal work established ‘the bar’ for distributed QIP with different node sizes, and until the present paper it remained the best approach for DQC-3. However for larger nodes there has been subsequent progress: for example, DQC-5 was examined in considerable detail in 2007 by Jiang *et al* [117], where the authors demonstrated that errors in the EO, *and* in both measurement and preparation can reach 5%. Very recently a preprint from Fujii has again raised the bar for DQC performance: they detail a DQC-4 scheme which supports fully fault tolerant QIP given a local gate error rate of 0.1% and a network EO fidelity as low as 70% [118]. The authors neglect memory errors (i.e. decoherence from sources other than gate operations) but note that this will have a limited impact.

To our knowledge, no previous study has developed a DQC-3 scheme capable of tolerating general noise in the network EO. It is not immediately obvious that this is even possible; one might imagine DQC-4 is the minimum, according to the following logic: Assume we wish to entangle the client qubits in two particular nodes (the client is sometimes referred to as the ‘data’ qubit – basically the qubit in each node that has the role of gaining/holding multiple high fidelity entanglement relations, and should be protected from low fidelity operations). We allocate one qubit per node to the role of holding newly created ‘raw’ entanglement (i.e. the broker role). Then, there remain two intermediate qubits per node. We pair these up between the two nodes, and purify bit errors from the broker pair onto the first intermediate pair. We then purify phase errors from the first interme-

4.3. A review of broker schemes - remote entangling operations on client qubits

mediate pair to the second intermediate pair. The second intermediate pair now holds high fidelity entanglement which can be teleported onto their clients using only the high fidelity local operations. (The authors of Ref. [118] perform a process analogous to this, except that they sometimes employ a step involving the broker and both intermediates, which they term double selection, and which boosts the overall purification performance). A scheme along these lines indeed seems necessary if one aims to have the capacity to perform arbitrary high fidelity entanglement operations on pairs of client qubits in different nodes. However, fortunately arbitrary gates are not required and in fact one particular kind of operation, the parity projection, can suffice. This is the key insight for the novel DQC-3 protocol we describe below.

4.3 A review of broker schemes - remote entangling operations on client qubits

We wish to perform an EO on the client qubits in each of two separate nodes. Each node contains a qubit which is directly associated with the (noisy) entanglement channel, i.e. the broker qubit – for example, an electron spin with an associated conditional optical transition which therefore permits non-local entanglement via ‘path erasure’ type schemes [92, 93, 23]. We assume that the primal network EO on the two broker qubits should ideally result in one of the four Bell states

$$|\text{bell}\rangle = \frac{1}{\sqrt{2}}[|0, \mu\rangle + (-1)^\nu |1, \mu \oplus 1\rangle], \quad (4.1)$$

Chapter 4. High threshold distributed quantum computing with three-qubit nodes

where $\mu, \nu = 0, 1$, but that in practice this state may be affected by errors. Without loss of generality we may write the erroneous superoperation as

$$E_{\text{ent.}} = A[1] + B[Z] + C[X] + D[Y]. \quad (4.2)$$

where $A + B + C + D = 1$, A is the fidelity of the entanglement and Pauli errors are acting on arbitrary one of the two qubits.

Two kinds of effective EOs can be implemented on client qubits as shown in Fig. 4.1. They are controlled-phase gates [119] and parity projections [98]. For an effective EO, a deterministic controlled-phase gate is performed locally in each node, which is performed on the client qubit and the broker qubit entangled with the other node. Then, two broker qubits are measured in appropriate bases. For an effective controlled-phase gate, one of two broker qubits is measured in the X basis while the other is measured in the Y basis. For an effective parity projection, two broker qubits are both measured in the X basis. In order to complete an effective EO, some single-qubit gates have to be performed on client qubits. These single-qubit gates are chosen depending on the initial Bell state of broker qubits and measurement outcomes. We call the client (broker) qubit in node i as qubit Ci (Bi). Two measurement outcomes of $B1$ and $B2$ are ρ and σ , where $\rho, \sigma = 0, 1$. Then, for effective controlled-phase gates, single-qubit gates are $[1 + i(-1)^\delta Z_{C1}][1 + i(-1)^\delta Z_{C2}]Z_{C2}^\mu$. For parity projection on client qubits, single-qubit gates are Z_{C2}^μ , and the obtained parity projection should be

$$\frac{1}{2}[1 + (-1)^\delta Z_{C1}Z_{C2}]. \quad (4.3)$$

Here, $\delta = \nu \oplus \rho \oplus \sigma$.

4.3. A review of broker schemes - remote entangling operations on client qubits

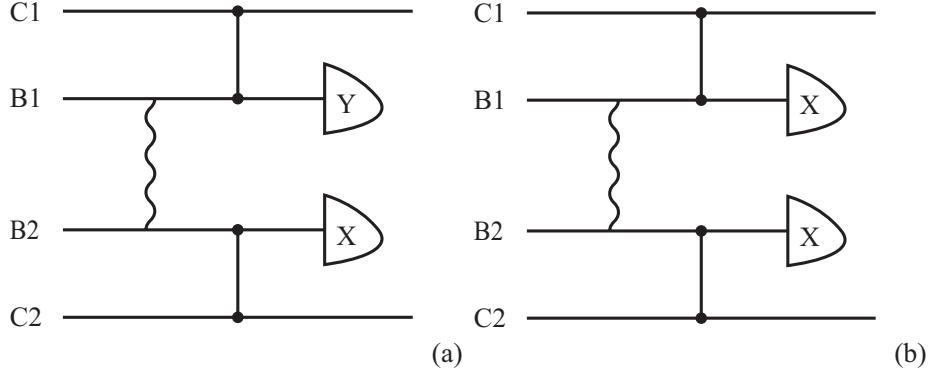


Figure 4.1: Circuits of (a) the effective control-phase gate and (b) the effective parity projection on client qubits. Qubit C_i (B_i) is the client (broker) qubit in the node i .

4.3.1 Effective control-phase gates

The initial state of two client qubits is $|\alpha\rangle|\beta\rangle$. The initial state of two broker qubits is

$$|0, \mu\rangle + (-1)^\nu |1, \mu \oplus 1\rangle. \quad (4.4)$$

The outcomes of measurements in the X basis and in the Y basis are $|x\rho\rangle$ and $|y\sigma\rangle$ respectively. Here, $\alpha, \beta, \mu, \nu, \rho, \sigma = 0, 1$.

The state after two control-phase gates is

$$[|0, \mu\rangle + (-1)^\nu |1, \mu \oplus 1\rangle Z_{C_1} Z_{C_2}] Z_{C_2}^\mu |\alpha\rangle |\beta\rangle. \quad (4.5)$$

Here, the order of qubits is B_1, B_2, C_1, C_2 . The state after the measurement in the X basis is

$$[(-1)^{\rho\mu} |0\rangle + (-1)^{\nu \oplus \rho(\mu \oplus 1)} |1\rangle Z_{C_1} Z_{C_2}] Z_{C_2}^\mu |\alpha\rangle |\beta\rangle. \quad (4.6)$$

The state after the measurement in the Y basis is

$$[(-1)^{\rho\mu} - i(-1)^{\nu \oplus \rho(\mu \oplus 1) \oplus \sigma} Z_{C_1} Z_{C_2}] Z_{C_2}^\mu |\alpha\rangle |\beta\rangle, \quad (4.7)$$

which can be rewritten as

$$(-1)^{\rho\mu}[1 - i(-1)^\delta Z_{C1}Z_{C2}]Z_{C2}^\mu |\alpha\rangle |\beta\rangle, \quad (4.8)$$

where $\delta = \nu \oplus \rho \oplus \sigma$. Phase gates

$$\exp[i\frac{\pi}{4}(2\delta-1)Z_{C1}] \exp[i\frac{\pi}{4}(2\mu+2\delta-1)Z_{C2}] = i[1+i(-1)^\delta Z_{C1}][1+i(-1)^\delta Z_{C2}]Z_{C2}^\mu. \quad (4.9)$$

is performed on two client qubits to get the state

$$i(-1)^{\rho\mu}[1 + i(-1)^\delta](1 + Z_{C1} + Z_{C2} - Z_{C1}Z_{C2}) |\alpha\rangle |\beta\rangle, \quad (4.10)$$

where the overall factor $2i(-1)^{\rho\mu}[1 + i(-1)^\delta]$ can be neglected, and Here, $\Lambda_{C1,C1} = (1 + Z_{C1} + Z_{C2} - Z_{C1}Z_{C2})/2$ is a control-phase gate on two client qubits.

4.3.2 Effective parity projections

The initial state of two client qubits is $|\alpha\rangle |\beta\rangle$. The initial state of two broker qubits is

$$|0, \mu\rangle + (-1)^\nu |1, \mu \oplus 1\rangle. \quad (4.11)$$

The outcomes of measurements in the X basis are $|x\rho\rangle$ and $|x\sigma\rangle$ respectively. Here, $\alpha, \beta, \mu, \nu, \rho, \sigma = 0, 1$.

The state after two control-phase gates is

$$[|0, \mu\rangle + (-1)^\nu |1, \mu \oplus 1\rangle Z_{C1}Z_{C2}]Z_{C2}^\mu |\alpha\rangle |\beta\rangle. \quad (4.12)$$

Here, the order of qubits is $B1, B2, C1, C2$. The state after the measure-

4.4. Overview of full noise purification with DQC-3

ment on $B2$ in the X basis is

$$[(-1)^{\rho\mu} |0\rangle + (-1)^{\nu\oplus\rho(\mu\oplus 1)} |1\rangle Z_{C1}Z_{C2}]Z_{C2}^\mu |\alpha\rangle |\beta\rangle. \quad (4.13)$$

The state after the measurement on $B1$ in the X basis is

$$[(-1)^{\rho\mu} + (-1)^{\nu\oplus\rho(\mu\oplus 1)\oplus\sigma} Z_{C1}Z_{C2}]Z_{C2}^\mu |\alpha\rangle |\beta\rangle, \quad (4.14)$$

which can be rewritten as

$$(-1)^{\rho\mu}[1 + (-1)^\delta Z_{C1}Z_{C2}]Z_{C2}^\mu |\alpha\rangle |\beta\rangle, \quad (4.15)$$

where $\delta = \nu \oplus \rho \oplus \sigma$. After a phase gate Z_{C2}^μ and neglecting the overall factor $2(-1)^{\rho\mu}$, we get

$$\frac{1}{2}[1 + (-1)^\delta Z_{C1}Z_{C2}] |\alpha\rangle |\beta\rangle, \quad (4.16)$$

where $P_{C1,C2}^\delta = [1 + (-1)^\delta Z_{C1}Z_{C2}]/2$ is a parity projection on two client qubits.

4.4 Overview of full noise purification with DQC-3

Here we establish that three qubits per node can suffice to enable distributed quantum computing with very noisy network EOs. The possibility of fully purifying network noise using only DQC-3 was mentioned by Campbell in 2007, when he developed the concept of purifying a parity projection *operation* rather than purifying a quantum state [120]. Campbell showed that, given a source of entangled pairs whose infidelity is largely

phase noise (i.e. bit noise is low), one can directly perform a high fidelity parity projection (PP) on two client qubits in an unknown state. Here we incorporate Campbell’s approach to effectively cut out one of the intermediate qubits in the description of DQC-4 above: We pair up the single intermediate qubit in each of two nodes, purify bit errors from the brokers onto this pair, and since this pair now exhibits principally phase noise it can be used to directly apply a PP to the clients.

In effect Campbell’s technique repeatedly performs a PP until one gains sufficient confidence that it has occurred with outcome either ‘odd’ or ‘even’ – this exploits the fact that once a PP has occurred, successive PPs have no new effect on the qubits (in contrast to, say, a controlled-phase gate negating the effect of a prior application). We show here how to use such gates to build a particular large scale entangled state between our nodes: namely Raussendorf’s TPC state [76, 77, 78]. This is the same state that is the target of Refs. [111, 116, 118]. It is a convenient target since one need only show that the state can be built (and measured) with a certain fidelity in order to assert that universal QIP is then possible. Here, we need to find a route to generating the TPC state with the fewest possible parity projections in order to minimise the accumulation of errors. The route we employ is discussed below; in obtaining our threshold we also benefit from work by Barrett and Stace [79] which shows that the TPSC need not be perfect in order to retain its fault tolerance (up to 25% of the structure can be deleted provided of course that one knows which parts are absent).

4.5 Purifying the parity projection operation

We wish to perform a high fidelity parity projection operation on the client qubits in each of two separate nodes of our DQC-3 machine. Each node

4.5. Purifying the parity projection operation

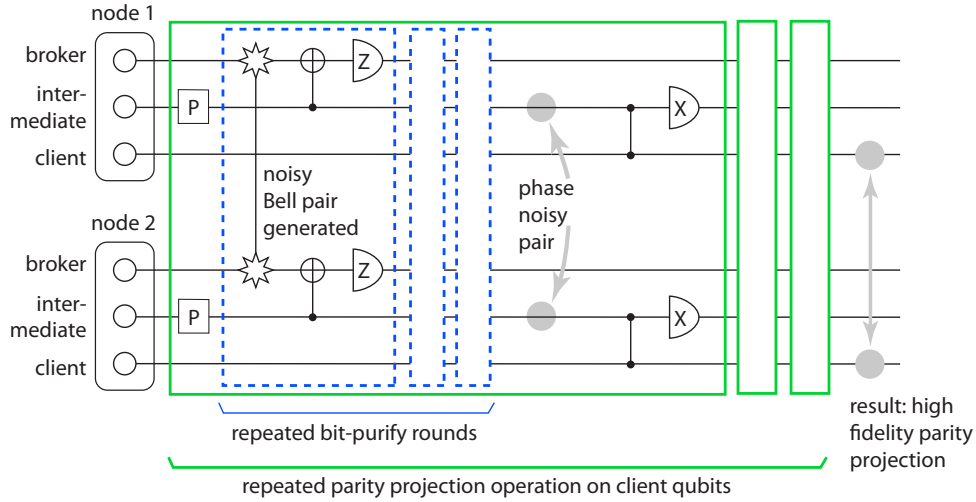


Figure 4.2: The full protocol for implementing a high fidelity parity projection on the clients. Note that only the brokers are involved in an operation spanning the two nodes: this is the network EO which generates a noisy Bell pair. The box marked P denotes preparation of each intermediate qubit into a state such as $|+\rangle$. In a typical physical implementation the broker qubit is an optically active system whereas the other two qubits in each node need not be (they might be realised as nuclear spins, for example). Preparation and measurement of the intermediate qubit could in practice be achieved by transferring the state to/from the broker for optical readout. The client qubits of course never undergo preparation or measurement in this process: the parity projection applies to an arbitrary incoming client state.

contains a qubit which is directly associated with the (noisy) entanglement channel, i.e. the broker qubit. Additionally each node contains one intermediate qubit. We assume that the primal network EO on the two broker qubits should ideally result in one of the four Bell states, but that in practice this state may be affected by errors.

We employ a flip-error entanglement pumping scheme according to which we generate a succession of ‘raw’ Bell states on the broker pair, and via local gates and measurements we progressively generate a state on the intermediate qubit pair with an improved noise profile: flip errors are heavily suppressed, although phase errors will have increased [117].

Chapter 4. High threshold distributed quantum computing with three-qubit nodes

We now use this intermediate pair to perform a parity projection on the client qubits (see Fig. 4.2, outer level of nesting). For a moment, let us neglect the significance of residual flip errors on the intermediate qubit pair, and local gate errors. Consider the consequence of the substantial phase error probability p_P : in the event of such an error one finds that a PP is nevertheless performed successfully on the clients, but we have an incorrect record of whether the outcome was ‘odd’ or ‘even’ (P_{C_1, C_2}^0 or P_{C_1, C_2}^1). However the intermediate qubits are now available again, and we are free to repeat the previous pumping procedure and generate a new bit-flip-corrected pair, and so perform a second parity projection on the clients. Indeed we can repeat this as many times as we wish. Campbell’s observation is that we can then deduce the likely true parity from looking at the relative frequency with which ‘odd’ and ‘even’ are reported.

After $h = m + 2l$ parity projections on a pair of client qubits, where $m + l$ measurement outcomes indicate the same parity while l indicate the other parity, the probability of a wrong parity is reduced to

$$P_P = \frac{\alpha^{-m}}{\alpha^m + \alpha^{-m}}, \quad (4.17)$$

where $\alpha = \sqrt{p_P^{-1} - 1}$. The next effective parity projection increases the difference m with a probability

$$h_m = \frac{\alpha^m(1 - p_P) + \alpha^{-m}p_P}{\alpha^m + \alpha^{-m}}. \quad (4.18)$$

If there were no types of error other than phase errors on the source, then one could continue this process to produce an arbitrarily high fidelity parity projection (i.e. continue until difference m is very large). In practice, there are residual flips errors on the source, errors on local operations within

4.5. Purifying the parity projection operation

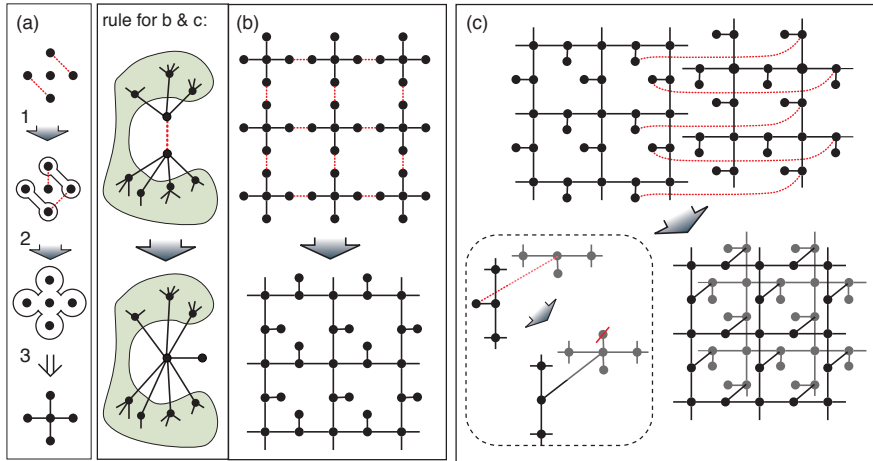


Figure 4.3: The strategy we adopt for generating the full TPC state. The graph state notation is employed. Red dashed lines indicate pairs of qubits that will be subject to a PP in the next step. The wide, shaded arrow indicates that PPs are applied, and possibly local operations (often these can be omitted or subsumed over several steps). In (a) we show how to generate a ‘cross’ graph: the first two steps each involve two parallel PPs, the third step is simply a set of local rotations. In the next panel we show a general graphical rule for applying a PP plus local gate(s) on two qubits that are already part of a graph state: after the PP we rewrite the graph with an arbitrary one of the two qubits inheriting all their prior connections, and the other as a ‘dangling bond’. In (b) we connect a grid of cross graphs into a lattice (unterminated lines indicate the lattice can continue to arbitrary size with the same pattern). In (c) we take two such lattices and connect them so that they become two planes of the TPC state. The inset shows that each PP is followed by removing one qubit in the z basis. Note that the final object has dangling bonds in the more distant plane, and these are exactly as required to repeat the process and connect another lattice sheet (and in fact multiple sheets may be fused in one time step).

each node, and memory errors. The effect of these errors increases with the number of effective parity projections h . Therefore, it is useful to truncate m and h . We introduce the rule that if the difference m is at least some target M after at most as H parity projections on the same pair of client qubits, then the parity projection is deemed successful. Otherwise the protocol is deemed a failure. This means that we will have (known) imperfections in the TPC state that we are trying to generate; but the work of Barrett and Stace [79] allows us to translate this damage rate into an lowered threshold at which the TPC state achieves fault tolerance. This tradeoff between PP fidelity and the threshold of the TPC state gives us an opportunity numerical optimisation which we exploit in obtaining our results.

4.6 Building the TPC state within the constraints of DQC-3

In Section 4.5 we described how DQC-3 enables high fidelity parity projection (PP) between nodes of the computer. We must now harness this entangling operation for generating the target TPC state. It is essential to use as few operations as possible since each PP will introduce some risk of errors to the structure. The procedure we employ is depicted in Figure 4.3.

The process is quite efficient: We require only five time steps in order to generate a two dimensional lattice as shown in panel (b): Specifically one step to prepare client qubits, three further steps in panel (a), and then a single PP step in panel (b). We then need only two further steps (one PP, one measurement) to combine any number of such lattices into the full TPC state. This is comparable to the number of steps that would

4.6. Building the TPC state within the constraints of DQC-3

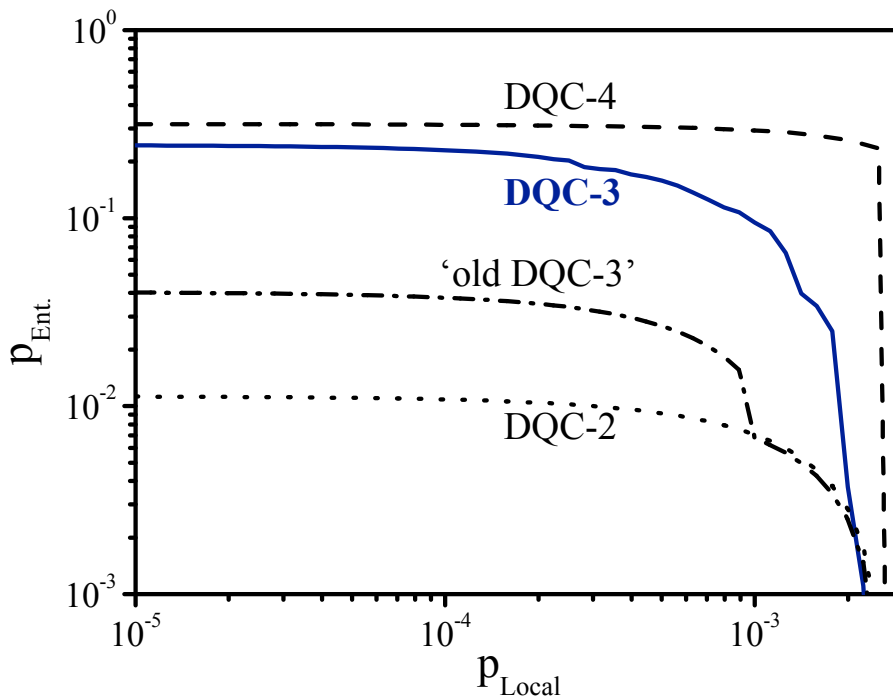


Figure 4.4: State of the art thresholds for fully fault tolerant distributed quantum computing. The probability of an error on the ‘raw’ network entangling operation is $p_{\text{Ent.}}$ and the equivalent probability for local operations within a node (rotations, two-qubit gates or measurements) is p_{Local} . The area to the lower left of any line represents the region in which fault tolerant QIP is possible. Here memory errors are neglected (c.f. Fig. 4.5). The DQC-3 performance (blue) is derived from the analysis in this paper. For comparison we plot also the DQC-4 performance which we reproduce from a graph in Ref. [118]. We note that very high rates of infidelity can be tolerated by DQC-3 although the additional qubit in DQC-4 does allow still greater tolerance (at local error rates of 10^{-3} tolerance of network infidelity approaches 10% for DQC-3 and 30% for the DQC-4). We also plot the ‘previous best’ protocol for DQC-3, as described in the text.

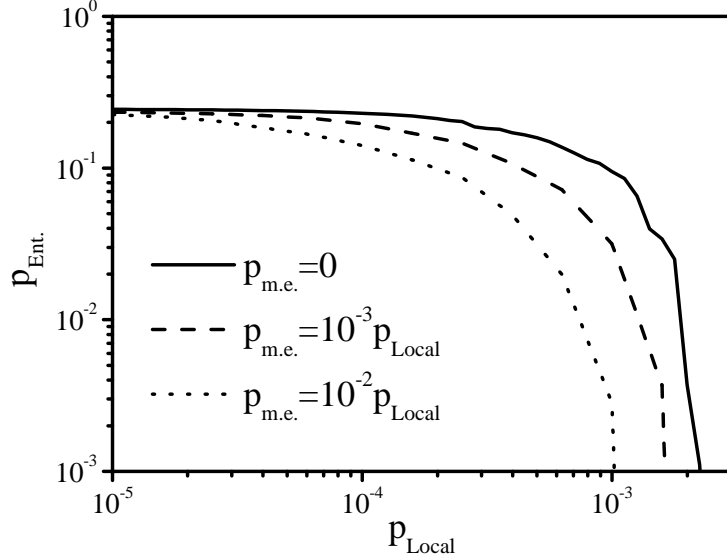


Figure 4.5: This plot indicated the impact of memory errors. p_{mem} is the probability that an errors occurs on an inactive qubit during one typical time step of the basic protocol. Rates are as given in the figure, but note that they are exacerbated by a 90% rate of heralded EO failure (see text).

be required to generate a TPC state by directly following the constructive definition, i.e. using controlled-phase gates (which require at least DQC-4 if purification is to be employed). Consequently the thresholds which we presently determine for DQC-3 are not very much lower than those that DQC-4 attains.

4.7 Results

Using the techniques described in the preceding sections, we obtain conditions for fault tolerant QIP in terms of the fundamental characteristics of the DQC-3 machine: the fidelity on the network EO, the fidelity of local operations, and the memory error rate (i.e. the rate at which errors occur even when no operations are applied). There are also parameters internal

4.7. Results

to the protocol, such as the choice of how many rounds to allow for distilling the parity projection before abandoning it – these parameters are selected by numerical optimisation.

Our results are shown in Figures 4.4 and 4.5. We make the simplification that all local errors, i.e. rotation, local entanglement and measurements, occur with the same probability. In Fig. 4.4 we plot the case where memory errors can be neglected, and for contrast in Fig. 4.5 we plot the case of significant memory errors. Note that the memory error rates chosen are more severe than in many real systems: for example it may take only tens of microseconds to rotate a nuclear spin, whereas the spin decoherence time can be of order minutes [121]. We also apply a very high outright (heralded) failure rate to the network EO of 90%. This means that each time the protocol requires a new ‘raw’ entangled pair to be generated, on average there will be 10 attempts required before the protocol can proceed. Even under these highly adverse conditions, the DQC-3 scheme still tolerates network EO infidelity of order 10% for local error rates well above 10^{-4} .

Long range failure-tolerant entanglement distribution

5.1 Introduction

Distributing an entangled state among remote quantum computers is one of the fundamental tasks of quantum information technologies. It is crucial for quantum teleportation, quantum cryptography and distributed quantum computing. Using direct transmission, the success probability of transmitting a qubit and the fidelity of the resulting quantum state decrease exponentially with distance. Therefore, one needs quantum repeaters to achieve long distance entanglement [29, 122]. A good quantum repeater protocol should be fault-tolerant and provided with a high communication rate. In this paper, we will propose a protocol to distribute entanglement between two remote quantum computers. We consider noise in quantum communication channels, and of course errors generated by operations within the repeaters. We assume that the repeater stations may employ non-deterministic EOs: that is, a means of entanglement, even within the a single repeater, that often fails but those failures are ‘heralded’. In addition there are is of course a finite error rate even for the operations that are deemed successful. Non-deterministic EOs can be implemented with small quantum registers networked by optical setups, i.e. qubits can be entangled

Chapter 5. Long range failure-tolerant entanglement distribution

by joint measurements on single photons emitted from these qubits rather than control of interactions [23, 24]. Such an architecture may be much easier to implement in a scalable way than e.g. large scale ion traps. We find that the rate of distributing entanglement decreases only logarithmically with the communication distance.

In our protocol, the task of distributing entanglement is done by single-qubit measurements on a TPC state [76, 77, 78] across the chain of repeater stations. The TPC state must first be grown via operations within repeaters together with quantum communication between pairs of neighbouring repeaters. These operations within repeaters are expected to have a much better performance than communications between repeaters. The protocol is valid if the probability of an error occurring in the communication channel is lower than a threshold, which is 15% when errors induced by operations within repeaters are negligible. With errors less than the threshold, entanglement can be established between two remote logical qubits encoded in two separated graph states, which may be used for further information processing via the topological measurement based quantum computing [76, 77, 78]. Alternatively one can also decode each logical qubit to a physical qubit via single-qubit measurements. Although we describe only the two-party protocol here, it should be straightforward to generalize for distributing multi-party entanglement.

In this protocol, the quality of the eventual entanglement between logical qubits is only limited by the number of qubits in each repeater. Therefore, our protocol effectively distills as well as distributes entanglement. The idea of using an error correction code with protected logical qubits for remote entanglement was firstly reported in Ref. [30], in which the Calderbank-Shor-Steane code is employed. Recently, in a protocol of

5.2. The scheme

quantum state transfer of a surface-code-encoded qubit, the efficiency of quantum communication is greatly improved by removing the necessity of two-way communication [31]. Compared with these protocols, ours is the first to consider a probabilistic architecture within each repeater station, so that the entanglement distribution can be efficient even if EOs are far from deterministic.

This Chapter is organized as the following. In Sec. 5.2, we describes the whole picture of our scheme. In Sec. 5.3, we illustrate how to grow the graph state across the quantum communication line using probabilistic operations. And in Sec. 5.4, errors on the graph state and error correction is discussed. In the Sec. 5.5, we discuss the scaling of local resources and the overall communication rate.

5.2 The scheme

In order to generate entanglements between two remote quantum computers Alice and Bob, the two computers are connected via a chain of quantum repeater stations. Two nearby repeaters are connected by optical quantum communication channels (Fig. 5.1(a)). To give an overview of the process: Firstly, a TPC state is grown across quantum repeater stations via probabilistic EOs and quantum communications between nearby stations. The TPC state contains two parallel empty tubes, which terminate in stations of Alice and Bob. Each empty tube is a part of the TPC state without any qubit, which has a line-like shape and shown as a blue rectangular cuboid in Fig. 5.1(b). Once the TPC state is generated, measurements in the X basis are performed on all qubits except two parts of the TPC state located in stations of Alice and Bob respectively (Fig. 5.1(c)). Each unmeasured part is called a plug, which are connected with empty tubes.

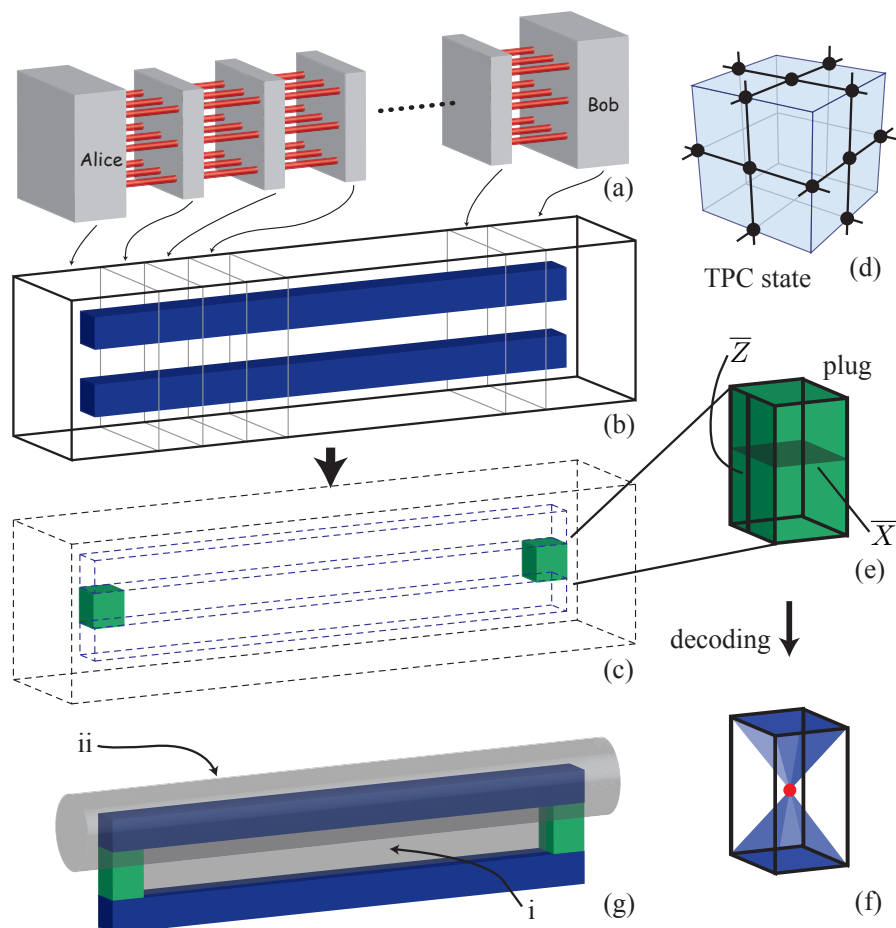


Figure 5.1: The scheme of quantum entanglement distribution protocol based on topologically protected cluster (TPC) state. (a) Alice and Bob can be entangled via a chain of quantum repeater stations, which are connected by optical quantum communication channels. (b) Each station contains a ‘slice’ of the TPC state which there exists across all repeater stations. The TPC state contains two empty tubes (blue) without any qubit. (c) All qubits are measured in X basis except two parts of the TPC state (green) in stations of Alice and Bob respectively, which are called plugs and contain the eventual encoded shared Bell pair. (d) The elementary cell of the TPC state. Each logical qubit is encoded as subfigure (e) and can be decoded as subfigure (f). (g) Two surfaces propagating correlations between two logical qubits.

5.2. The scheme

Two empty tubes and two plugs form a closed loop. There is one logical qubit encoded in each plug. All measurement outcomes are transmitted to Alice and Bob. Ultimately, two logical qubits are entangled as one of the Bell states (determined by measurement outcomes).

The logical qubit is encoded in a plug as $\bar{X} = \prod_{a \in section} X_a$ and $\bar{Z} = \prod_{b \in line} Z_b$, where \bar{X} and \bar{Z} are Pauli operators of the logical qubit. Here, *section* is a dual surface across the plug, and *line* is a primal chain on the surface of the plug and connecting two empty tubes (Fig. 5.1(e)). We consider two stabilizers according to the following surfaces: (i) c_i is a primal surface whose boundary is enclosed by the tube-plug loop, and (ii) c_{ii} is a closed dual surface enveloping one empty tube and crossing two plugs (Fig. 5.1(g)). These two stabilizers are $K(c_i) = \bar{Z}_A \bar{Z}_B \prod_{a \in c_i} X_a$ and $K(c_{ii}) = \bar{X}_A \bar{X}_B \prod_{a \in c'_{ii}} X_a$, where A, B denote Alice and Bob respectively, and c'_{ii} denotes the part of the surface c_{ii} outside two plugs. After measurements in the X basis, one can replace X_a with measurement outcomes. Then, we get two new stabilizers $\bar{Z}_A \bar{Z}_B = \pm 1$ and $\bar{X}_A \bar{X}_B = \pm 1$, i.e. two logical qubits are stabilized as one of Bell states. Here, two signs depend on measurement outcomes.

Noise in quantum communication channels and imperfections in operations will make some phase errors on the TPC state. In order to eliminate errors from the Bell state of two logical qubits, we monitor errors on the TPC state by parity check operators $K(c_c)$, where c_c are minimum closed surfaces. Usually, minimum closed surfaces are surfaces of elementary cubics. However, some qubits on the TPC state may be missing. The parity check operator of an elementary cube with missing qubits can not be used to detect errors. Then, one has to use products of parity check operators connected by missing qubits to get as a new set of parity check operators

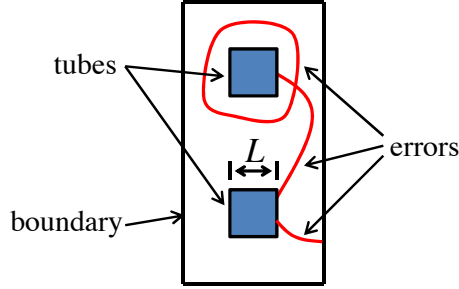


Figure 5.2: A section of the topological protected cluster state with non-trivial error rings and error chains which can induce an logical error.

[79]. Parity check operators reveal the endpoints of error chains, where an error chain (ring) is a sequence of phase errors. If the number of phase errors on the surface c_c is odd, the existence of errors can be identified by $K(c_c)$, which is called an error syndrome. Errors are not actively corrected, rather parities of $\prod_{a \in c_i} X_a$ and $\prod_{a \in c'_i} X_a$, are modified by knowledge of the total number of error chains crossing surfaces c_i and c'_i respectively. After the error correction, only error rings encircling with the tube-plug loop, error chains connecting two empty tubes and error chains connecting the loop with the boundary of the TPC state (see Fig. 5.2), may contribute an error on logical qubits. If noise and imperfections are less than a threshold, the probability of an error on logical qubits decreases exponentially with the minimum length of these error rings and error chains [76, 77, 78].

5.3 Cluster state growth

In order to grow the TPC state across quantum repeater stations, some ‘building-block’ graph states should be prepared first. The structure of these elementary graph states can be a star [100], a line [92, 99], a cross [101], or a tree [107, 103]. In this paper, we take the tree structure as an example, and the scheme can be adapted to other structures. The tree

5.3. Cluster state growth

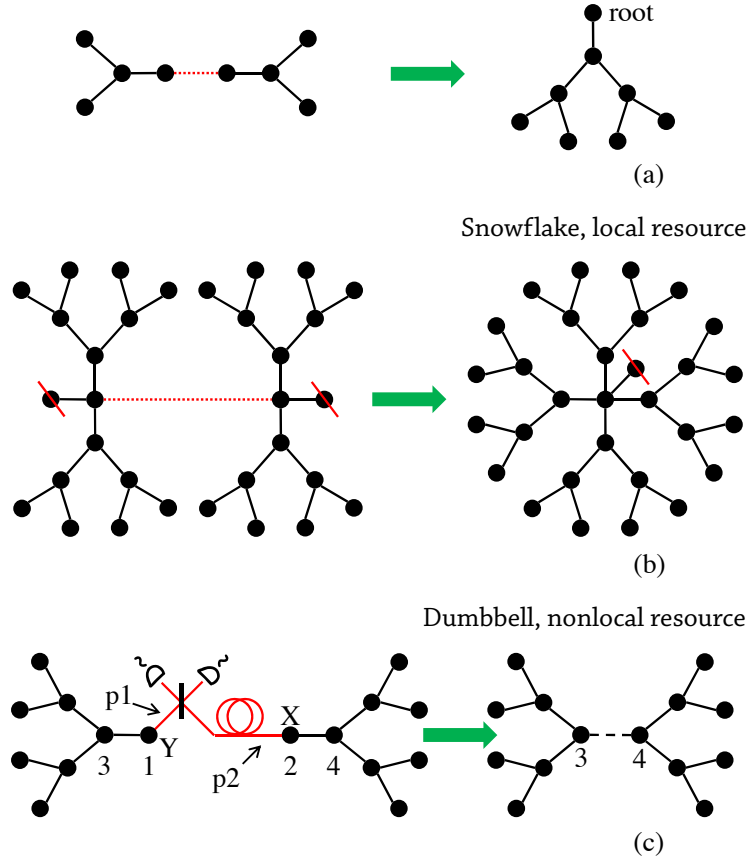


Figure 5.3: Resource graph states for growing the topologically protected cluster state. Each read dotted line denotes a parity projection (PP). (a) Tree graph states can be grown by PPs on roots of trees. (b) Four trees can be fused into a ‘snowflake’ graph state as the following: fusing each pair of trees into a bigger tree at first; cutting two roots by measurements in Z basis; fusing them into a snowflake and cut the unwanted qubit. (c) Two trees in different quantum repeater stations are fused into a dumbbell graph state by a Bell measurement on the photon-p1 and the photon-p2, each associated with a qubit in a different stations. One of the photons (p2) have to be transferred from one station to another. The Bell measurement is followed by a measurement in the Y basis on the qubit-1 and a measurement in the X basis on the qubit-2, in order to get the ‘dumbbell’ graph state.

Chapter 5. Long range failure-tolerant entanglement distribution

structure accumulates fewer errors than other structures when the success probability of EOs is low [103, 111]. Tree-structure graph states can be generated by using parity projections (PPs) [24]. A PP on roots of two individual trees can fuse them into a double-size tree (Fig. 5.3(a)). If all PPs are successful, after n steps, one can grow a tree with 2^n qubits from separated qubits, where the integer n is called the generation of the tree.

Trees are fused into two kinds of building-block graph states. *Snowflake* graph states are prepared by fusing four trees (Fig. 5.3(b)). Each snowflake will ultimately correspond to a specific qubit on the TPC state. Each quarter of a snowflake is used to establish a connection with a neighboring snowflake. We refer to the second kind of building-block as a *dumbbell*. These are nonlocal building blocks connecting two nearby quantum repeater stations (Fig. 5.3(c)). A dumbbell is formed by two trees located in different stations. For example, suppose that the basic qubits are optically active atoms: then in order to prepare a dumbbell, we cause each root qubit emit a single photon as $|\eta\rangle_j \rightarrow |\eta\rangle_j |\eta\rangle_{pj}$, where $j = 1, 2$ denotes a root qubit, ‘ pj ’ denotes the corresponding photonic qubit, $\eta = 0, 1$ is the label the state in the computational basis and the photonic qubit can be encoded in polarization, frequency [23] or time-bin [92]. One photon is transmitted from one station to another. After a Bell measurement on two photons and single-qubit measurements on roots, we obtain the dumbbell graph state.

The state of a tree together with the photon emitted from its root qubit- j ($j = 1, 2$) reads

$$|\Psi\rangle_{Tj} = \frac{1}{\sqrt{2}}(|0\rangle_{pj} |0\rangle_j |G\rangle_{tj} + Z_{j+2} |1\rangle_{pj} |1\rangle_j |G\rangle_{tj}), \quad (5.1)$$

where $|\eta\rangle_j$ is the state of the root qubit- j , $|\eta\rangle_{pj}$ is the state of the photon- j .

5.3. Cluster state growth

Here, $|G\rangle_{tj}$ is the graph state of the tree without its root but including the qubit- $(j + 2)$, and Z_{j+2} is the Pauli operation acting on the qubit- $(j + 2)$. Measurements are performed on photons and roots. As an example, we consider the case that the outcome of the Bell measurement on two photons is

$$|\Phi^+\rangle_{p1,p2} = \frac{1}{\sqrt{2}}(|0\rangle_{p1} |0\rangle_{p2} + |1\rangle_{p1} |1\rangle_{p2}), \quad (5.2)$$

while the outcome of the measurement in the Y basis on the qubit-1 is $|y+\rangle_1$ and the outcome of the measurement in the X basis on the qubit-2 is $|+\rangle_2$. After measurements, we get

$$\begin{aligned} |D'\rangle_{db} &\propto \langle +|_2 \langle y+|_1 \langle \Phi^+|_{p1,p2} |\Psi\rangle_{T1} |\Psi\rangle_{T2} \\ &= \frac{1}{4\sqrt{2}}(1 - iZ_3Z_4) |G\rangle_{t1} |G\rangle_{t2}. \end{aligned} \quad (5.3)$$

Then, we perform single-qubit operations $(1 + iZ_3)/\sqrt{2}$ and $(1 + iZ_4)/\sqrt{2}$. We get

$$|D\rangle_{db} = \frac{1}{2}(1 + Z_3 + Z_4 - Z_3Z_4) |G\rangle_{t1} |G\rangle_{t2}, \quad (5.4)$$

where $(1 + Z_3 + Z_4 - Z_3Z_4)/2$ is a control-phase gate on qubit-3 and qubit-4, and a overall phase has been ignored. Here, $|D\rangle_{db}$ is the dumbbell graph state. All sets of outcomes are equivalent to each other up to those two single-qubit operations, which can be substituted with updating Pauli frames, and postponed until they must eventually be accounted for.

Making a building-block graph state requires all operations to be successful, whose probability may be quite small. Therefore, building-block graph states are produced with a post selection strategy: if an operation is heralded as failed, the corresponding graph state is abandoned with the qubits reinitialized. One can always obtain enough building-block with enough trials.

Chapter 5. Long range failure-tolerant entanglement distribution

Snowflakes are assembled by PPs on leaves, which are qubits on the edge of a snowflake (Fig. 5.5). Two snowflakes in the same quantum repeater station can be connected directly, while two snowflakes in different stations are connected by bridging them with a dumbbell shared by these two stations. The number of leaf qubits on each quarter of a snowflake is 2^{n-1} . Therefore, the failure probability of connecting two snowflakes in the same station is $F_L = f^{2^{n-1}}$, and the failure probability of connecting two snowflakes in different stations is $F_{NL} \simeq 2F_L$, where f is the basic failure probability of EOs. After establishing connections between snowflakes, all qubits except those at the center of each snowflakes are removed by appropriate single-qubit measurements, so that the surviving qubits form the TPC state. Since some snowflakes have failed to be connected, this implies some missing connections on the TPC state. We presently describe simulations establishing that when connections are rarely missing, i.e. $F_L < 5\%$, the cluster state is well connected and it is easy to find surfaces propagating correlations between two logical qubits as long as it exists, which is guaranteed in the scaling limit (as expected from percolation theory) [123, 79].

In order to remove redundant qubits, we firstly chose a path between two center qubits. All qubits beside the chosen path are measured in the Z basis. For a nonlocal connection, all qubits on the path are measured in the X basis, as shown in Fig. 5.4(a). For a local connection, the three qubits in the middle of the chosen path are measured in the Y basis while others on the path are measured in the X basis, as shown in Fig. 5.4(b). If a connection is failed to be established between two snowflakes, all qubits between two two center qubits are measured in the Z basis. Qubits-3 and qubit-4 are always on the path between two successfully connected

5.3. Cluster state growth

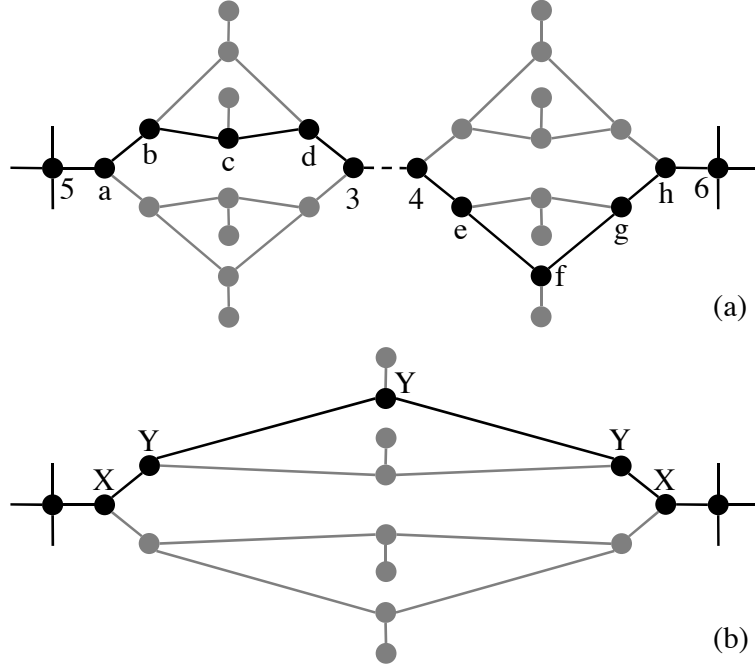


Figure 5.4: Measurement patterns for cleaning up redundant qubits. We illustrated the case that all parity projections on leaves all succeed as an example. Gray qubits are measured in the Z basis.

snowflakes. We consider two products of stabilizers on the path (qubits beside the path have been cleaned up) as shown in Fig. 5.4 (a), $\tilde{K}_5 = K_5 K_b K_d K_4 K_f K_h$ and $\tilde{K}_6 = K_6 K_g K_e K_3 K_c K_a$, where the stabilizer of graph states $K_i = X_i \prod_{j \in N(i)} Z_j$ and $N(i)$ denotes the set of neighbors of qubit- i . The two products are also stabilizers of the graph state, and

$$\tilde{K}_5 = X_5 X_b X_d X_4 X_f X_h Z_6 \prod_{j \in N(5) - \{a\}} Z_j, \quad (5.5)$$

$$\tilde{K}_6 = X_6 X_g X_e X_3 X_c X_a Z_5 \prod_{j \in N(6) - \{g\}} Z_j. \quad (5.6)$$

After measurements in X basis on the path, X operators except X_5 and X_6 in two products can be replaced by outcomes. Then, one can get two new stabilizers $X_5 Z_6 \prod_{j \in N(5) - \{a\}} Z_j$ and $X_6 Z_5 \prod_{j \in N(6) - \{g\}} Z_j$, which imply a direct connection between qubits 5 and 6. The conclusion is valid for

general-size trees.

The ‘building-block’ strategy is not always necessary. If the failure probability of EOs is low enough $f < 5\%$, one may generate the TPC state directly, for example, by using control phase gates [76, 77, 78], where control-phase gates on two qubits located in different quantum repeater stations can be simulated by consuming entanglements prepared via quantum communications [119].

5.4 Noise, Imperfections and Error Correction

Both noise in quantum communication channels and imperfections in operations can make errors on the TPC state. We assume communication noise is depolarized, and described by the superoperator $E = (1 - \varepsilon)[1_{p2}] + \varepsilon([X_{p2}] + [Y_{p2}] + [Z_{p2}])/3$ (Fig. 5.3(c)). We call qubits with nonlocal connections as joint qubits (Fig. 5.5(b)). Because the photon-2 may be affected by noises in the optical quantum channel, the state $|\Psi\rangle_{T2}$ affected by noises is transformed to

$$\begin{aligned} \rho_{T2} = & (1 - \varepsilon) |\Psi\rangle \langle \Psi|_{T2} + \frac{\varepsilon}{3} (X_{p2} |\Psi\rangle \langle \Psi|_{T2} X_{p2} \\ & + Y_{p2} |\Psi\rangle \langle \Psi|_{T2} Y_{p2} + Z_{p2} |\Psi\rangle \langle \Psi|_{T2} Z_{p2}). \end{aligned} \quad (5.7)$$

After measurements and single-qubit operations, we get a noisy dumbbell graph state

$$\begin{aligned} \rho_{db} = & (1 - \varepsilon) |D\rangle \langle D|_{db} + \frac{\varepsilon}{3} (Z_3 Z_4 |D\rangle \langle D|_{db} Z_3 Z_4 \\ & + Z_3 |D\rangle \langle D|_{db} Z_3 + Z_4 |D\rangle \langle D|_{db} Z_4). \end{aligned} \quad (5.8)$$

5.4. Noise, Imperfections and Error Correction

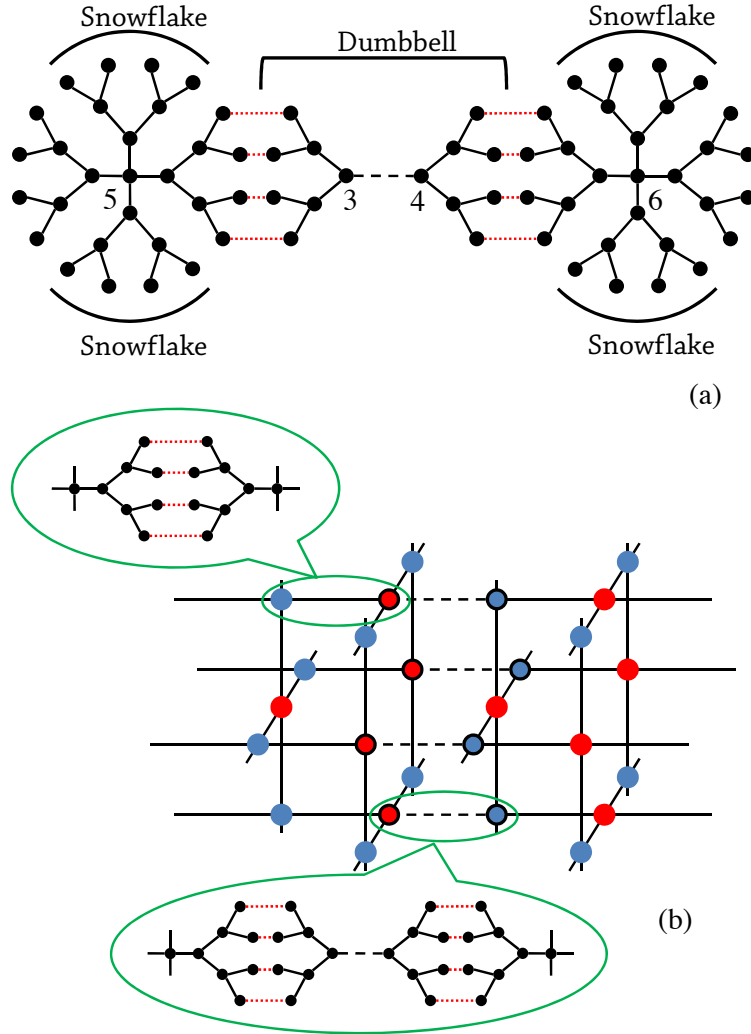


Figure 5.5: The strategy of assembling resource graph states into the topologically protected cluster (TPC) state across quantum repeater stations. (a) Snowflakes within the same station are connected directly to each other by parity projections (red dot lines) on leaves. Two snowflakes in different stations can be connected by connecting snowflakes with a dumbbell shared by these two stations. (b) Each qubit on the TPC state used to be the qubit on the center of a snowflake. The TPC state in different stations are connected via nonlocal connections (dash lines) on joint qubits (with black ring).

Here, the error $Z_3 Z_4$ (Z_3, Z_4) is propagated from the error X_{p2} (Y_{p2}, Z_{p2}). An error $[Z_3]$ ($[Z_4]$) can induce a wrong outcome of X_3 (X_4), which changes the sign of the corresponding stabilizer, i.e. induces an error $[Z_6]$ ($[Z_5]$). Therefore, errors induced by communication noise may make phase errors on corresponding joint qubits (qubits 5 and 6) with a probability $2\varepsilon/3$ for each of them.

If internal operations within stations are perfect (when heralded as successful), then only joint qubits have errors, and error correction can be performed independently on each joint layer. The error threshold of a two dimensional layer is about 10% for a perfectly connected lattice [81, 124]. Once operations are perfect, one can always grow a big tree to make F_L as low as possible. Therefore, with perfect operations, the condition of getting a correct correlation between two logical qubits faithfully is $2\varepsilon/3 \lesssim 10\%$, i.e. the error threshold of communication noise is $\varepsilon_t \simeq 15\%$.

With imperfect operations, all qubits on the TPC state may be affected by phase errors. If the distribution of phase errors is uniform, i.e. all qubits may have a phase error with the same probability, the error threshold of phase error is about 3% for perfectly connected TPC state [80]. However, in our case, the TPC state grown by probabilistic EOs is unlikely to be perfectly connected and there are more errors on joint qubits than others. We treat missing connections by transforming them to qubit loss, by means of deleting the qubits with missing connections using measurements in the Z basis. Therefore, the loss probability of joint qubits is $5F_L$, and the loss probability of other qubits is $4F_L$. We determine error thresholds for general cases numerically as shown in Fig. 5.6(a), using the method developed in Ref. [105, 79].

The error rate of imperfect operations must be lower than the thresh-

5.4. Noise, Imperfections and Error Correction

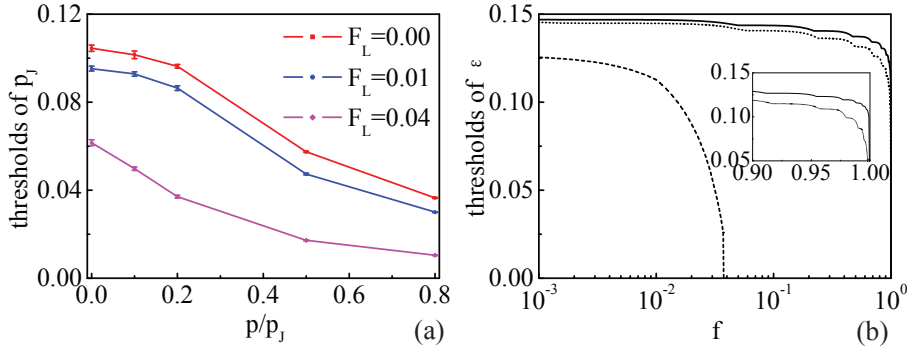


Figure 5.6: Thresholds of error correction on the topologically protected cluster (TPC) state. (a) Thresholds of phase errors on joint qubits, which is dependent on the ratio between the error probability on joint qubits (p_J) and the error probability on other qubits (p). (b) Thresholds of communication noise ε with operational error rate 10^{-4} (solid line), evaluated from the linear interpolation of data in subfigure (a). By using control-phase gates to generate the TPC state directly, the error rate can be much more higher (2×10^{-3}) but only a failure probability (f) lower than 4% is tolerable (dash line). Memory errors may happen at a lower rate than operational errors. Memory errors at 10% of the operational error rate can lower the threshold, but not dramatically (dotted line).

old of fault-tolerant quantum computing (FTQC). The threshold of FTQC on the TPC state with non-deterministic EOs (deterministic control-phase gates) is about 2×10^{-4} [111] (5×10^{-3} [76, 77, 78]). By optimizing the size of trees, (a bigger tree can reduce missing connections but generates more errors), we obtained thresholds of communication noise with the present of operational errors in Fig. 5.6(b). If the error rate of operations is 10^{-4} , the threshold of communication noise is about 11% when the success probability of entangling operations is 1%. In contrast, by using control-phase gates to generate the TPC state directly, the threshold of communication noise is still above 10% even if the error rate of operation is 2×10^{-3} , but the success probability must be higher than 98%.

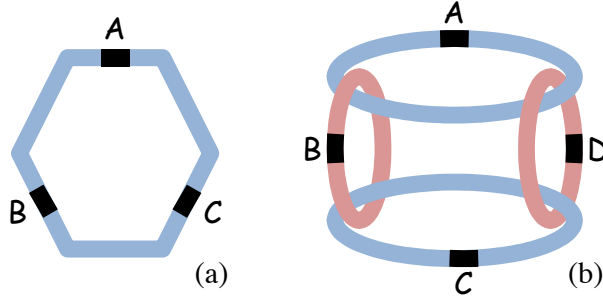


Figure 5.7: Topological structures of tubes (blue and red) and plugs (black) for distributing (a) 3-qubit GHZ states and (b) 4-qubit cluster states.

5.5 Performance

A logical qubit can be decoded into a physical qubit by measurements on the corresponding plug with one qubit unmeasured. The residual qubit carries the quantum state of the logical qubit. For decoding, two pyramids inside the plug, whose apexes hold the residual qubit and bases connect tubes, are measured in the Z basis, while other qubits are measured in the X basis (Fig. 5.1(f)). The residual qubit can acquire an error if there is an error chain connecting two pyramids. Therefore, the probability of an error on the residual qubit is $p + O(p^3)$ [76, 77, 78], where p is the probability of phase errors on the residual qubit, which is usually lower than 3%. Besides two-party entanglements, our scheme can be generalized to multi-party entanglements, e.g. three-party and four-party entanglements as shown in Fig. 5.7.

The probability of errors on two entangled logical qubits decreases exponentially with the minimum length of error rings and error chains. We design the TPC state as follows: the perimeters of two empty tubes, the distance between empty tubes and the distance between each empty tube and the boundary is proportional to the same length scale L . The length of the TPC state, i.e., the number of quantum repeater stations, can increase

5.5. Performance

the probability of error rings and error chains linearly. Therefore, the overall probability of errors on two entangled logical qubits is $\varepsilon_E \propto N e^{-\kappa L}$, where N is the number of stations, κ is a constant depending on p , p_J and F_L . Here, $\kappa \sim 1$ for the probability of errors that is one third of the threshold [78]. For achieving a given quality of entanglement, we need a TPC state with $L = O(\log(N/\varepsilon_E))$. The number of photonic qubits transferred between two nearby stations is proportional to L^2 . Therefore the overall entanglement distribution rate of our scheme is $R_N = O(\log^{-2}(N/\varepsilon_E))$. If entanglement can be established and distilled (e.g. $\varepsilon_E = 10^{-3}$) with a megahertz rate between two repeater stations, the bandwidth is one quarter of megahertz after 1000 times distance in our protocol.

Two dimensional scalable quantum network with general noise

6.1 Introduction

Creating entanglement over long distances is the main goal of quantum communication, with applications in quantum key distribution, fundamental tests of quantum mechanics, and distributed computing, among others [125]. However the fragility of entanglement to environmental noise limits the effective distance of direct quantum communication. One of the most celebrated solutions to this problem is the use of quantum-repeaters [29]. As a drawback, this strategy consumes an amount of quantum memories per repeater that grows rapidly with the distance for establishing entanglement, even when error-correction is used [30, 31].

The distribution of entanglement in quantum networks has been the focus of intense research. Non-trivial geometry of the quantum network can be used, for instance, in entanglement percolation [32] or error correction strategies [33, 34, 35, 36]. However, all the known results in this direction rely on unrealistic quantum states [32, 37, 38, 39, 40, 41, 42] or networks with an impractical geometry (e.g. three-dimensional) [33, 35, 36] or the

consumption of a growing amount of local resources [34, 43]. Entanglement distribution in a noisy two-dimensional network with a fixed local resources is believed to be possible through one-dimensional fault-tolerant quantum computation schemes [34, 36]. However such a scheme often require quantum communications and operations with a very small error rate (approximately 10^{-5}) [87, 45]. Thus, the problem of designing a realistic scalable quantum network remains largely unresolved.

In this Chapter, we show that it is possible to entangle two distant sites in a two-dimensional network involving realistic quantum channels. In the present proposal, the number of quantum memories per node needed is fixed and does not scale with the communication distance. Also, the scalability of the two-dimensional quantum network does not rely on the scalability of quantum processors. Moreover quantum communication error rates of up to 1.67% can be tolerated.

6.2 Scheme

Our starting point is a quantum network on the square lattice (see Fig.6.1). Each node in the network is connected to its neighbours through a quantum channel that distribute two-qubit Werner states ρ given by

$$\rho = (1 - q)|\Phi_+\rangle\langle\Phi_+| + q\frac{\mathbf{I}}{4}, \quad (6.1)$$

where $|\Phi_+\rangle = (|00\rangle + |11\rangle)/\sqrt{2}$ is a maximally entangled state, $\frac{\mathbf{I}}{4}$ is the maximally mixed state, and $0 \leq q \leq 1$ is a noisy parameter. This state can be understood as the result of the following process: a maximally entanglement state $|\Phi_+\rangle$ is produced and sent to a neighbouring site through a depolarizing channel. This channel leaves the state untouched with prob-

6.2. Scheme

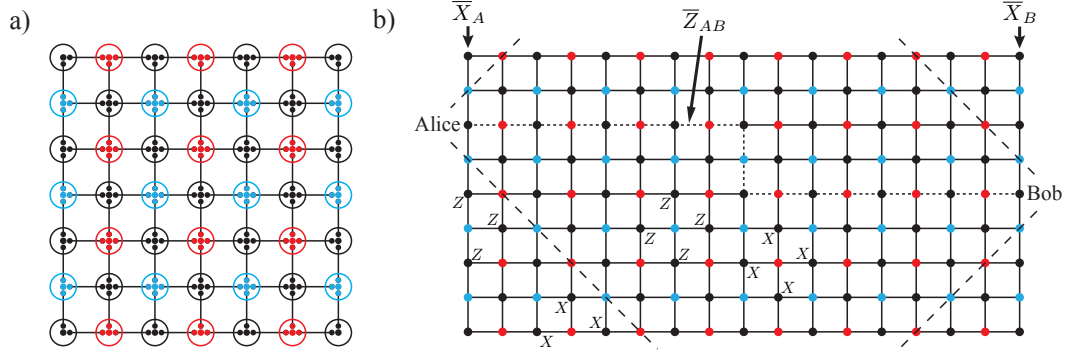


Figure 6.1: (a) Quantum network on the square lattice. Each node has four linking qubits, which can be entangled with neighbouring nodes, while the fifth one is used to process the surface code. The colors are used to label the nodes according to the operations to be realized during the protocol. (b) A rectangular part of the quantum network is used to create entanglement between qubits in Alice and Bob's sites (see text).

ability $F = \langle \Phi_+ | \rho | \Phi_+ \rangle = 1 - 3q/4$ (i.e. the fidelity between ρ and $|\Phi_+\rangle$) and causes an error with probability $1 - F$, which we call the channel error rate. Note that since any two-qubit state can be put into the form Eq. 6.1 by local operations and classical communication [126], our results can also cover other cases of quantum states. The main goal in our scheme is to entangle two arbitrarily distant nodes, labelled by Alice and Bob, using quantum channels connecting neighbouring nodes, local operations at each node and one-way classical communication among them. Here we will consider, apart from the communication noise, possible errors in these operations. Our protocol is based on the surface code [127] and could be generalized to other geometries [128, 129]. Apart from the four qubits in each node composing the network, we need one more qubit in each node for processing the surface code.

To generate remote entanglement between Alice and Bob, we consider a section of the rectangular network as shown Fig. 6.1 (b). We divide the nodes within this section of the network into three groups, marked in

black, *blue* and *red* in the figure. Each *blue* (*red*) node is surrounded by four *black* nodes (or three, if it is along a border of the rectangle). Alice and Bob are both placed in the *black* group and located on two edges in this rectangular network, e.g two vertical sides composed of *black* nodes and *blue* nodes. The other two sides are composed of *black* nodes and *red* nodes. At the start of the protocol, we initialize all processing qubits in *black* nodes to the state $|0\rangle$. We then use the entanglements shared between neighbours to perform stabilizer measurements $ZZZZ$ (ZZZ) and $XXXX$ (XXX) of four (three) *black* processing qubits around each *blue* and *red* node respectively. Here, Z and X are Pauli operators. A circuit describing these measurements is shown in Fig. 6.2. As soon as these stabilizer measurements are performed, the state of *black* processing qubits becomes an eigenstate of the stabilizers of the surface code [127]. Finally, all *black* processing qubits except Alice and Bob's qubits are measured in the following way:

- all *black* processing qubits along the two vertical sides are measured in the X basis;
- all *black* processing qubits along the dot line composed of *black* and *red* nodes connecting Alice and Bob (see Fig. 6.1b) are measured in the Z basis;
- Qubits in the region defined within the dash lines in Fig 6.1b are measured in the Z basis and the ones outside are measured in the X basis.

Here, we choose the dotted line so that it is in the middle of two corresponding dashed lines when it is near Alice and Bob or two horizontal lines when it is far away from Alice and Bob. We argue that, after these

6.2. Scheme

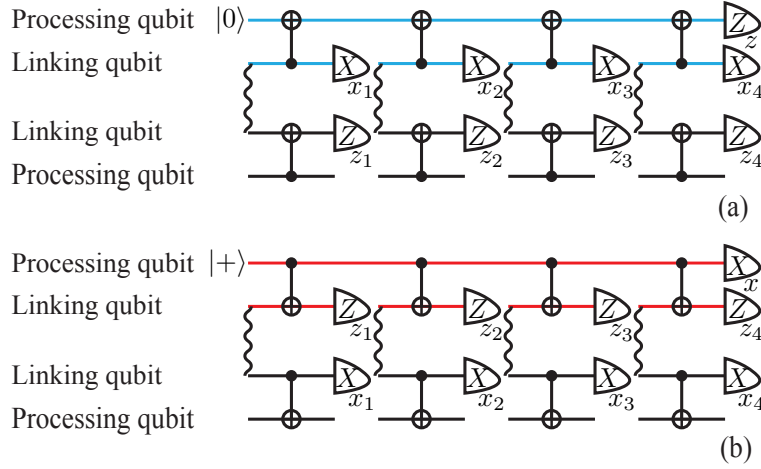


Figure 6.2: Circuits for stabilizer measurements (a) $ZZZZ$ and (b) $XXXX$. Circuits for stabilizer measurements ZZZ and XXX are similar. On each subfigure, the upper two lines are the processing qubit and linking qubits of a *blue* or *red* node, while the lower two lines are processing qubits and linking qubits of four neighboring *black* nodes. Each wave line represents a Bell state $|\Phi^+\rangle$ of two corresponding linking qubits. The measurement outcome of $ZZZZ$ ($XXXX$) is $zz_1z_2z_3z_4$ ($xx_1x_2x_3x_4$), where z and z_i (x and x_i) are outcomes of measurements in the Z (X) basis of the *blue* (*red*) processing qubit and the i th black linking qubit respectively. Each *blue* (*red*) node interacts with its four neighbouring *black* nodes in the order: left, up, right, down. After interacting with a *blue* (*red*) node, a *black* processing qubit need a phase (flip) gate Z^{x_i} (X^{z_i}), where x_i (z_i) is the measurement outcome of the corresponding *blue* (*red*) linking qubit.

measurements, the processing qubits of Alice and Bob are entangled.

In order to see that, let us first consider the perfect case, i.e. when $q = 0$ and all operation are perfect. The initial state of *black* processing qubits, which are all initialized in the state $|0\rangle$, is the eigenstate of \bar{Z}_{AB} with the eigenvalue $+1$. Here, \bar{Z}_{AB} is the product $\prod Z$ of *black* processing qubits on the line connecting Alice and Bob (the dot line in Fig. 6.1 (b)). The operator \bar{Z}_{AB} commutes with the stabilizer operators. Therefore, the stabilizer state is still an eigenstate of \bar{Z}_{AB} with the eigenvalue $+1$. The stabilizer state is also an eigenstate of the product of all $XXXX$ and XXX , which is $\bar{X}_A\bar{X}_B$, where \bar{X}_A (\bar{X}_B) is the product $\prod X$ of *black* processing qubits

on the vertical side with Alice (Bob) (see Fig. 6.1 (b)). One can obtain the eigenvalue of $\bar{X}_A\bar{X}_B$ by multiplying measurement outcomes of all $XXXX$ and $XX\bar{X}$. After measuring out *black* processing qubits except the processing qubits in Alice and Bob (i.e. the qubit A and the qubit B), we can replace Z and X in \bar{Z}_{AB} and $\bar{X}_A\bar{X}_B$ with the respective measurement outcomes. Finally, we see that the state of qubits A and B are “stabilized”, i.e., they become an eigenstate of Z_AZ_B and X_AX_B , where eigenvalues depend on measurement outcomes. In this way, the qubit A and the qubit B are entangled as one of Bell states.

Imperfections in quantum channels and in local operations can result in incorrect stabilizer-measurement outcomes. In order to obtain a set of faithful stabilizer-measurement outcomes, the stabilizer measurements must be repeated N times before final single-qubit measurements on *black* processing qubits. For each stabilizer measurement, the entanglement between neighbouring sites needs to be regenerated. Thus the overall time cost of our scheme is NT , where T is the communication time for generating neighbouring entanglements.

It is crucial to realize that *black* processing qubits may be affected by errors during the stabilizer measurements. However these errors can be detected: if any of the stabilizer-measurement outcomes are different from each other in the previous time step, we have an error syndromes and we immediately conclude that incorrect stabilizer-measurement outcomes and errors on *black* processing qubits have happened. Moreover, it is possible that some qubits are initialized wrongly states other than the state $|0\rangle$ at the very beginning. We can detect such initialization errors based on measurement outcomes of $ZZZZ$ stabilizers, i.e. all $ZZZZ$ should be $+1$ if the qubits are initialized correctly. Errors occurring after the last stabilizer

6.2. Scheme

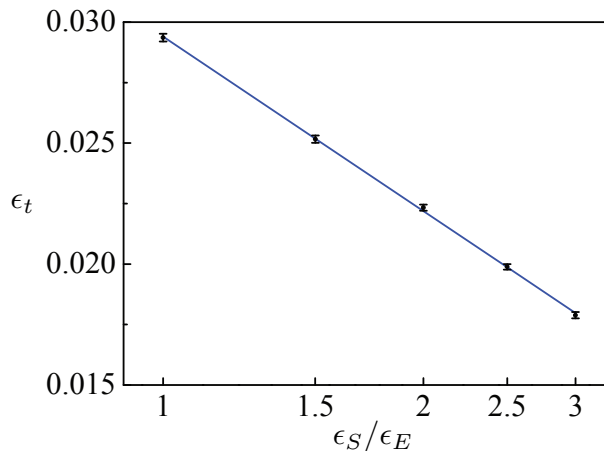


Figure 6.3: Error thresholds for a variety of ratios between ϵ_S and ϵ_E for independent errors. Here, ϵ_t is the threshold of ϵ_E , i.e., errors are correctable if $\epsilon_E < \epsilon_t$. Squares represent thresholds for $\epsilon_S/\epsilon_E = 1, 1.5, 2, 2.5, 3$ without correlations. These thresholds are obtained numerically by pairing error syndromes with the minimum-weight perfect-matching algorithm [81, 79]. The line is obtained by fitting thresholds with the function $\epsilon_t = \epsilon_0 - k \log(\epsilon_S/\epsilon_E)$.

measurement, including errors induced by the last stabilizer measurement and subsequent operations, cannot be detected by further stabilizer measurements. Thus, we may need to measure more *black* processing qubits rather than only qubits included in \overline{Z}_{AB} and $\overline{X}_A \overline{X}_B$ (see the measurement pattern defined by the dash lines in Fig. 6.1). We then detect these errors that occur after the last stabilizer measurements through a comparison of the outcomes of single-qubit measurements with outcomes of stabilizers, i.e. the outcome of a stabilizer should be the same as the product of outcomes of individual qubits in the stabilizer. One corrects stabilizer-measurement outcomes and all other errors by pairing error syndromes [130], as in the typical surface-code error correction.

6.3 Error thresholds

The surface code works if the probability of errors is lower than a certain threshold. The outcome of a $XXXX$ or $ZZZZ$ measurement may be wrong with a probability ε_S . Between two time steps of stabilizer measurements, phase errors $[Z]$ (flip errors $[X]$) may happen on each *black* processing qubit with a probability ε_E . Here and throughout we use the form $[U]$ to denote the superoperator $[U](\rho) = U\rho U^\dagger$. By considering only the errors coming from quantum channels that occur "independently" and by considering the limit where q is small, $\varepsilon_S = 2q$, and $\varepsilon_E = q$. In fact, errors corresponding to $XXXX$ and $ZZZZ$ stabilizers are correlated. However, these two kinds of errors can be corrected separately. Thus, correlations between them can be ignored. Under these conditions, we find numerically that the error threshold depends on the ratio $\varepsilon_S/\varepsilon_E$ as $\varepsilon_t = \varepsilon_0 - k \log(\varepsilon_S/\varepsilon_E)$ (see Fig. 6.3), where $\varepsilon_0 = 0.0294$ and $k = 0.0072$ are constants and ε_{th} is the threshold of ε_E (i.e. errors are correctable if $\varepsilon_E < \varepsilon_{th}$). In our case in which $\varepsilon_S/\varepsilon_E = 2$, the noise in quantum channels is correctable if $q = \varepsilon_E < 2.23\%$, corresponding to an error rate of 1.67%.

Imperfect operations, including the initialization of qubits, measurements, and controlled-NOT gates, may also result in errors, reducing the tolerable error rate of quantum channels. Without loss of generality, we may assume that errors in operations are depolarized with the same rate p . Erroneous operations are modelled by perfect operations preceded or followed by an erroneous superoperation $E_1 = (1-p)[I] + (1/3)([X] + [Y] + [Z])$ for single-qubit operations or $E_2 = (1-p)[I] + (1/15)([I_1X_2] + \dots + [Z_1I_2] + \dots + [X_1Y_2] + \dots)$ for two-qubit operations. Moreover, imperfect two-qubit gates may give rise to correlations between phase errors on *black* processing qubits, which take place in the form $[Z_{red}Z_{right}]$, $[Z_{red}Z_{down}]$,

6.4. Final remote entangled state

and $[Z_{right}Z_{down}]$ with the same probability ε_C between two time steps of stabilizer measurements. Here, $[Z_{red}]$ is a phase error on a *red* processing qubit, which can induce an incorrect outcome of the stabilizer measurement, and $[Z_{right}]$ ($[Z_{down}]$) is a phase error on the *black* processing qubit to the right (downward direction) of the *red* processing qubit. All other phase errors are independent, i.e. $[Z_{red}]$, $[Z_{right}]$, and $[Z_{down}]$ happen with the probabilities $\varepsilon_S - 2\varepsilon_C$, $\varepsilon_E - 2\varepsilon_C$, and $\varepsilon_E - 2\varepsilon_C$, respectively. Flip errors corresponding to stabilizers $ZZZZ$ are also similar. By counting these errors, we find $\varepsilon_S = 2q + 124p/15$, $\varepsilon_E = q + 76p/15$, and $\varepsilon_C = 8p/15$. Then, we evaluate the thresholds of quantum channels with imperfect operations as shown in Fig. 6.4 and show that if the error rate of operations is 10^{-3} , the threshold of q is about 1.69%, corresponding to an error rate of 1.27%.

Memory errors can occur in our scheme while we are generating neighboring entanglements. Fortunately, these memory errors can also be detected by stabilizer measurements, and the decoherence time does not have to be comparable to the overall time cost NT but does for the communication time for generating neighboring entanglements T . We suppose memory errors are given by depolarization and occur with the rate p_m during the time T , which can increase ε_E by $2p_m/3$. Thus, memory errors on processing qubits can lower the threshold but not dramatically with $p_m = 10^{-2}$ as shown in Fig. 6.4.

6.4 Final remote entangled state

Even within the threshold, error correction may fail, because a chain of errors connecting boundaries (error chain) may not be detected through error syndromes. There are two kinds of nontrivial error chains that can affect the final entanglement between Alice and Bob: (i) error chains that

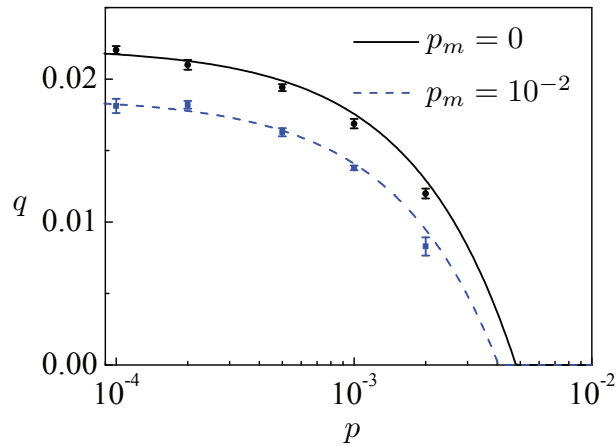


Figure 6.4: Thresholds of the communication-noise parameter q where p is the error rate of local operations. Memory errors can lower the threshold but not dramatically with the error rate $p_m = 10^{-2}$. Two curves are obtained by neglecting correlations and using the linear fitting in Fig. 6.3, which are good approximations of thresholds (rounds and squares for $p_m = 0$ and $p_m = 10^{-2}$, respectively) obtained numerically by pairing error syndromes with the minimum-weight perfect-matching algorithm [81, 79]. Thresholds of the communication noise parameter q , where p is the error rate of local operations. Memory errors can lower the threshold, but not dramatically with the error rate $p_m = 10^{-2}$.

6.5. Efficiency

flip qubits in \bar{Z}_{AB} for an odd number of times; and (ii) error chains that resulted in an odd total number of incorrect measurement outcomes of $XXXX$ stabilizers and phase errors on *black* processing qubits along two vertical sides after the last stabilizer measurement. In order to reduce the first kind of nontrivial error chains, the network for entangling Alice and Bob is designed so that the minimum distance between two horizontal sides and the line connecting Alice and Bob (the dot line in Fig. 6.1) is also N . Upon error correction, the total probability of long nontrivial error chains with the minimum length N decreases exponentially with N but increases polynomially with the distance between Alice and Bob [33]. Therefore, N scales only logarithmically with the communication distance, and thus these long error chains can then be neglected. Short nontrivial error chains with length shorter than N are all distributed in regions around Alice and Bob, whose probability also decrease exponentially with their length. More generally, noise in the final remote entanglement can be described by the superoperator $E_{AB} = F[1] + \varepsilon_X[X_A] + \varepsilon_Y[Y_A] + \varepsilon_Z[Z_A]$, where the fidelity $F = 1 - \varepsilon_X - \varepsilon_Y - \varepsilon_Z$. Assuming the last stabilizer measurement is $XXXX$, by only considering short error chains, we have $\varepsilon_X = q/2 + 2p_m/3 + 44p/15 + O(q^2, p_m^2, p^2)$, $\varepsilon_Y = 4p/15 + O(q^2, p_m^2, p^2)$ and $\varepsilon_Z = 4p/3 + O(q^2, p_m^2, p^2)$ [76, 35].

6.5 Efficiency

The communication time for generating neighboring entanglements T relies on the distance between two nearest-neighbor nodes. For example, for nearest-neighbor distance of 10 km, a neighboring entanglement can be generated with a probability $\sim 99.75\%$ in $T \sim 0.2$ ms. Here, we have supposed a repeat of the entanglement generation in order to reach this

high success probability, and the failure of generating entanglements is due to photon loss in fibers, whose attenuation is supposed to be 0.2 dB/km in this example. Failures of generating entanglements give rise to failures of stabilizer measurements, which are tolerable in surface codes. The presence of these failures can reduce the threshold of noises, but only slightly if the success probability is near 1 [79]. With L the distance between two vertical lines and $\sim N$ the distance between two horizontal lines, the probability of errors induced by long error chains scales as $\varepsilon_{\text{long}} \sim L e^{-\kappa N}$. Here, κ depends on the probability of errors, and $\kappa \sim 1$ for the probability of errors that is one-third of the threshold [78]. Therefore, entanglements can be generated rapidly over a long distance, e.g. with $N = 25$, resulting in 200 ebits/s, and $\varepsilon_{\text{long}}$ is still negligible if $L > 10^5$, i.e. an overall distance of 10^6 km.

Photonic multiqubit entangled states from a single atom

7.1 Introduction

The experimental effort devoted worldwide to the production and coherent manipulation of genuinely multiparticle-entangled states over the last decade has been tremendous [9, 46, 131, 132, 133, 134, 135, 136, 137, 138, 139, 140, 141, 142]. The main motivations behind this effort are arguably the potential applications of the GHZ [53] and cluster [19] states. The former can be considered as simple models of the celebrated *gedanken* Schrödinger-cat states [135, 138], are crucial for quantum communication and cryptography problems [143, 144, 145], and have been found useful in metrology [146] as well as in high-precision spectroscopy [147]. The latter are massively-entangled states that make one of the main paradigms of quantum computation possible, namely, the measurement-based one-way approach [19]. There, computation proceeds by a sequence of adaptive one-qubit measurements on the cluster, consuming cluster-state entanglement as the main resource.

As a physical platform for the transmission of quantum information without significant noise, photons are the natural choice. In addition, photonic platforms have potential for quantum information processing

since all-optical models for quantum computing using only linear-optical devices, single-photon sources and detectors exist [148]. Furthermore, in linear-optical setups, both photonic GHZ [131, 132, 138] and cluster [136, 137, 138, 139, 140, 141, 142] states have been demonstrated in proof-of-principle experiments with up to six photons. However, in these setups, photon-pair generation is highly inefficient, and the entangling gates necessary to fuse these pairs into larger multi-qubit states are in addition intrinsically probabilistic. This poses a fundamental obstacle to the scaling to large numbers of particles.

On the other hand, atom-cavity systems make excellent single-photon-single-atom interfaces [46, 47, 48, 49, 50, 51, 52]. High-efficiency single photons emitted in a predetermined spatiotemporal mode, from single neutral Rb [49] and Cs [47] atoms, and even trapped Ca^+ ions [48, 52], inside an optical cavity, have been realized. Furthermore, with similar experimental setups, single-photon-single-atom and single-photon-single-photon entanglements have been successfully demonstrated [149, 150, 50, 51].

In this chapter, we propose a family of protocols for the creation of photonic GHZ and linear cluster states emitted from a single atom – or ion – coupled to an optical cavity field. These protocols are based on laser pulses with different polarizations and exploit the atomic natural dipole-transition elements to state-selectively achieve the desired transitions. The methods are in principle deterministic. However, in practice the overall efficiency is never unity. We provide a detailed analysis of the sources of imperfections and show that cavity photon-emission efficiencies close to 70% per photon are feasible. The procedures are illustrated with ^{87}Rb and ^{40}Ca atoms as examples, respectively with and without hyperfine structure, and for whom the state-of-the-art technology is in an extremely advanced

7.2. The protocol

stage [134, 9, 48, 52, 150, 49, 50, 51]. Their extensions to other alkali-metal or alkaline-earth-metal species are straightforward.

This chapter is organized as follows. In Sec. 7.2 we present our ideas in abstract terms. In Secs. 7.3 and 7.4 we describe concrete experimental procedures to implement the proposed ideas with ^{40}Ca and ^{87}Rb atoms, respectively. We leave an analysis of the technical details common to both implementations for Sec. 7.5, and we devote Sec. 7.6 for an assessment of the experimental feasibility with current technology and some discussions. Finally, efficiencies and fidelities are discussed in Sec. 7.7.

7.2 The protocol

A neutral (or ionized) atom is optically (electrically) confined inside a high-finesse optical cavity [47, 48, 52, 49, 50, 51], with whose field the atom is strongly coupled. The atom is excited by laser-pulse sequences that propagate perpendicularly to the cavity axis. One of the cavity mirrors is partially transmissive and the well-defined photonic output mode through it provides the dominant channel of atomic decay. Repeated application of these pump sequences produces trains of photons that are collected at the cavity output by an optical fiber, through which they propagate with the desired multiqubit states in their polarization degree of freedom.

Each of the above-mentioned pulse sequences is designed to drive either of the following state-transformations on the atom-cavity system:

$$T_{GHZ} : |\pm\rangle \rightarrow \pm|\pm\rangle|\sigma^\pm\rangle, \quad \text{or} \quad (7.1a)$$

$$T_{LC} : |\pm\rangle \rightarrow \frac{1}{\sqrt{2}}(\pm|+\rangle|\sigma^+\rangle - |-\rangle|\sigma^-\rangle). \quad (7.1b)$$

and

$$T_{LCa} : |\pm\rangle \rightarrow \frac{1}{\sqrt{2}}(\pm|+\rangle|\sigma^+\rangle - |-\rangle|\sigma^-\rangle), \quad (7.2a)$$

$$\text{or } T_{LCb} : |\pm\rangle \rightarrow \frac{1}{\sqrt{2}}(\pm|+\rangle|\sigma^-\rangle + |-\rangle|\sigma^+\rangle). \quad (7.2b)$$

Here, kets $|+\rangle$ and $|-\rangle$ stand for two long-lived atomic states in which the atomic z computational basis is encoded. $|\sigma^+\rangle$ and $|\sigma^-\rangle$ in turn denote the right and left circularly-polarized states, respectively, of the photon emitted in each sequence, which constitute the photonic z computational states. Transformations 7.1 are called isometries, mapping the atomic-qubit Hilbert space into the two-qubit atomic-photonic one. Isometries for the sequential creation of multiqubit states were studied in Ref. [151] in general terms.

In the following, we show explicitly how the repeated application of transformations 7.1a or 7.1b, respectively, lead to N -photonic-qubit GHZ [53] or linear cluster [19] states. In both cases the protocol consists first of the successive application of transformations 7.1a or 7.1b, respectively, N times. This already generates the desired multiqubit states but in the hybrid atom- N -emitted-photons system. Then, to decouple the atom from the state, a projective measurement is applied to it. Naturally, such measurement is most efficiently done by taking advantage of the atomic coupling with the cavity photons. So, in both cases the atom is finally measured in the corresponding appropriate basis via a further excitation and subsequent measurement of the last emitted photon.

7.2. The protocol

7.2.1 GHZ and linear cluster states

We show here how the repeated application of transformations 7.1 leads to the generation of the desired multi-qubit states. Let us begin by the linear cluster state. The atom is initialized in—say—state $|\varphi_0\rangle \equiv |+\rangle$. Application of transformation 7.1b $N + 1$ times delivers the state

$$\begin{aligned} |\varphi_{N+1}\rangle &\equiv T_{LC}^{N+1}|\varphi_0\rangle & (7.3) \\ &\equiv \frac{1}{\sqrt{2^{N+1}}} \sum_{i_1 \dots i_{N+1} = \pm} (-1)^{i'_1 i'_2 + \dots i'_N i'_{N+1} + i'_{N+1}} |i_{N+1}\rangle |\sigma_{N+1}^{i_{N+1}} \dots \sigma_1^{i_1}\rangle, \end{aligned}$$

where we have explicitly subindexed each photon's polarization according to its order of emission. The summation goes over all possible polarization configurations. The primed indexes in the exponent in turn denote the mapping $+ \equiv 0$ and $- \equiv 1$. Also, notice that the atomic state i_{N+1} is locked to the polarization $\sigma_{N+1}^{i_{N+1}}$ of the last emitted photon. In fact, if we group the atom and the $(N + 1)$ -th photon together into a single effective qubit, state $|\varphi_{N+1}\rangle$ is already an $(N + 1)$ -qubit linear cluster state [19], but shared among the atom and the $N + 1$ photons. To disconnect the atom from the state, we simply measure it in its computational z basis. Naturally, this is most efficiently done by taking advantage of its coupling with the cavity photons: A projective measurement on the $(N + 1)$ -th photon in the computational basis $\{|\sigma_{N+1}^+\rangle, |\sigma_{N+1}^-\rangle\}$, with outcomes $\mu = 0$, for σ_{N+1}^+ , or $\mu = 1$, for σ_{N+1}^- , disconnects the effective atom-last-photon qubit from the rest of the cluster. The final state of the remaining N photons is – up to an innocuous, μ -dependent local unitary – nothing but the desired, fully-photonic 1D cluster state [19] (omitting normalization):

$$|\Phi_N\rangle = \sum_{i_1 \dots i_N = \pm} (-1)^{i'_1 i'_2 + \dots i'_{N-1} i'_N + i'_N \mu} |\sigma_N^{i_N} \dots \sigma_1^{i_1}\rangle. \quad (7.4)$$

For the case of the GHZ state, let us take the initial atom's state as $|\psi_0\rangle \equiv \frac{1}{\sqrt{2}}(|+\rangle + |-\rangle)$, for instance. We apply now transformation 7.1a N times to obtain

$$|\psi_{aN}\rangle \equiv T_{GHZa}^N |\psi_0\rangle \equiv \frac{1}{\sqrt{2}}[|+\rangle|\sigma_N^+ \dots \sigma_1^+\rangle + (-1)^N |-\rangle|\sigma_N^- \dots \sigma_1^-\rangle]. \quad (7.5)$$

As above, state $|\psi_{aN}\rangle$ is already an $N + 1$ -qubit atomic-photonic GHZ state. To decouple the atom we now measure it in its x basis, again via a photonic measurement. For this, we first apply transformation 7.1b once, which adds a further emitted photon with polarization locked to the atomic state as above. Next we measure this photon in its computational basis also as above. This projects the other N photons onto

$$|\Psi_{aN}\rangle = (-1)^\mu |\sigma_N^+ \dots \sigma_1^+\rangle - (-1)^N |\sigma_N^- \dots \sigma_1^-\rangle, \quad (7.6)$$

which is – up to a μ -dependent local unitary – the desired photonic GHZ state [53] (normalization omitted again). Notice finally that the initial atomic state here can also be taken as $|\varphi_0\rangle \equiv |+\rangle$. In this case the protocol is the same except for the first of the $N + 1$ required transformations, which is of the type 7.1b instead of [53]. The resulting state is – up to a minus sign – also given by 7.6.

7.3 Implementation with ^{40}Ca

This isotope does not feature hyperfine structure (see Fig. 7.1). The Zeeman sublevels of the $S_{1/2}$ ground state encode the atomic qubit: $|\pm\rangle \equiv |4S_{1/2}, m_J = \pm 1/2\rangle$, where the quantization direction is that of the cavity axis. Both the cavity mode and a monochromatic pump laser are in

7.3. Implementation with ^{40}Ca

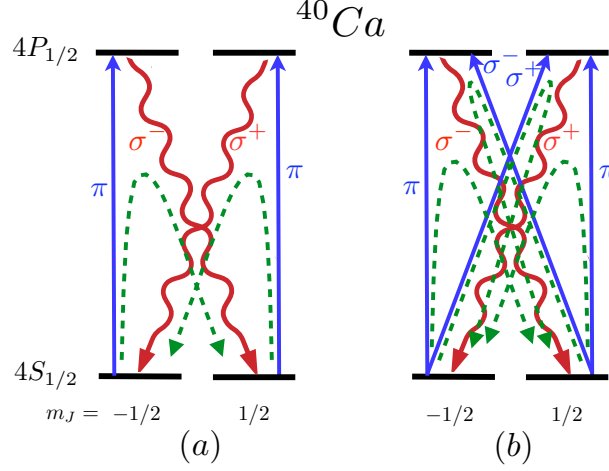


Figure 7.1: Relevant fine level structure of ^{40}Ca ion. Only photons (red wavy lines) with σ^+ or σ^- circular polarizations can decay into the cavity (resonant with $4S_{1/2} \leftrightarrow 4P_{1/2}$). (a) A π -polarized laser (blue lines) resonantly excites both ground-state sublevels $|4S_{1/2}, m_J = \pm 1/2\rangle$ to the $4P_{1/2}$ manifold. The total effective process including spontaneous photon emission is represented by green dashed lines, and its successive repetition creates a GHZ state. (b) Same as (a) but with the laser possessing also a σ^+/σ^- -polarization component. Two effective processes are driven simultaneously by the same pulse, and its repetition generates a linear cluster state.

resonance with the dipole transition $4S_{1/2} \leftrightarrow 4P_{1/2}$. The laser is linearly-polarized either perpendicular to the cavity axis, decomposing into two equal components of σ^+ and σ^- polarizations, or parallel to it. Photons with the former polarization, σ^+/σ^- , can only either absorb from or deliver to the atom one quantum m_J of angular momentum. Photons with the latter polarization, π , necessarily maintain m_J unchanged. Transformations 7.1 can both be realized with a single laser pulse.

For the case of 7.1a, the pump laser is π -polarized and drives the excitations $|S_{1/2}, m_J = \pm 1/2\rangle \rightarrow |P_{1/2}, m_J = \pm 1/2\rangle$. The cavity in turn supports only σ^+/σ^- polarizations, because photons propagating along the cavity axis cannot carry π polarization. Thus atomic decay takes place only through the transitions $|P_{1/2}, m_J = \pm 1/2\rangle \rightarrow \pm |S_{1/2}, m_J = \mp 1/2\rangle$

(the sign factor coming from the Clebsch-Gordan coefficients), accompanied by the corresponding emission of a σ^\pm photon into the cavity. Altogether, the ground-state sublevels transform as $|S_{1/2}, m_J = \pm 1/2\rangle \rightarrow \pm |S_{1/2}, m_J = \mp 1/2\rangle |\sigma^\pm\rangle$. Considering the qubit encoding, this transformation is—up to an atomic qubit-flip—precisely 7.1a. Since a qubit-flip is nothing but an innocuous local unitary operation, the resulting state is just the desired GHZ state but in a different local (qubit-flipped) basis.

In the case of 7.1b, we set the laser polarization forming an angle α with the cavity axis. That is, both components, π polarization, with weight $\cos(\alpha)$, and σ^+/σ^- polarization, with weight $\sin(\alpha)$, are now present in the polarization vector of the pump. Therefore, the following excitations can be driven [see Fig. 7.1 (b)]: $|S_{1/2}, m_J = \pm 1/2\rangle \rightarrow \cos(\alpha) |P_{1/2}, m_J = \pm 1/2\rangle \mp \sin(\alpha) |P_{1/2}, m_J = \mp 1/2\rangle$. These excitations decay via photon emission into the cavity exactly as before, yielding $|S_{1/2}, m_J = \pm 1/2\rangle \rightarrow \sin(\alpha) |S_{1/2}, m_J = \pm 1/2\rangle |\sigma_1^\mp\rangle \pm \cos(\alpha) |S_{1/2}, m_J = \mp 1/2\rangle |\sigma_1^\pm\rangle$) as the total transformation for the ground states. Once again taking into account the qubit encoding, we see that if $\alpha = \pi/4$ the latter is – up to local unitary qubit-flips – identical with transformation 7.1b.

7.4 Implementation with ^{87}Rb

This species possesses a rich hyperfine structure, schematically represented in Fig. 7.2. We use sublevels $|5^2S_{1/2}, F = 1, m_F = \pm 1\rangle \equiv |\pm\rangle$ of the ground-state hyperfine manifold as the atomic qubit. The short-hand notation

$$|5^2S_{1/2}, F = i\rangle \rightarrow |i\rangle$$

7.4. Implementation with ^{87}Rb

and

$$“5^2P_{1/2}, F = i” \rightarrow “i’”$$

is used throughout. The cavity mode is now in resonance with the $1 \leftrightarrow 2'$ transition.

We begin by the implementation of 7.1a, which requires two pulses. In the first one, sketched in Fig 7.2 (a), a two-photon Raman process resonant with the transition $1 \leftrightarrow 2$ partially transfers population from $|1, \pm 1\rangle$ to $|2, \pm 1\rangle$. This is performed with a conventional stimulated Raman adiabatic passage (STIRAP), very similar to the one used in Ref. [150]. Two π -polarized smooth laser pulses are used. One of them is resonant with the $2 \leftrightarrow 1'$ transition and is switched on first. The other one is resonant with $1 \leftrightarrow 1'$ and is switched on (reaches peak intensity) exactly when the first one reaches peak intensity (is completely switched off). This procedure allows for the use of a zero Raman-detuning at the same time keeping spontaneous emission negligible, for the entire evolution remains in a (adiabatically-varying) dark-state. The STIRAP-pulse area is such that $|1, \pm 1\rangle \rightarrow 1/2(\mp\sqrt{3}|1, \pm 1\rangle + |2, \pm 1\rangle) \equiv \pm|\eta^\pm\rangle$. States $|1, 1\rangle$ and $|1, -1\rangle$ rotate in opposite angles because of the relative signs between the Clebsch-Gordan coefficients (not shown) of the transitions involved.

In the second step [Fig. 7.2 (b)] a bichromatic laser pulse excites the atom to the $2'$ sublevels. Both laser-frequency components are σ^+/σ^- -polarized and have the same amplitude (with zero optical phase, for simplicity). One of them is resonant with $1 \leftrightarrow 2'$ and the other one with $2 \leftrightarrow 2'$. Taking into account the couplings shown in Fig. 7.2 (c), one sees that the interaction Hamiltonian is proportional to $H = |2', 2\rangle\langle\eta^+| + |2', -2\rangle\langle\eta^-| + |2', 0\rangle\langle\eta^\perp| + \text{h. c.}$, where $|\eta^\perp\rangle$ is a state orthogonal

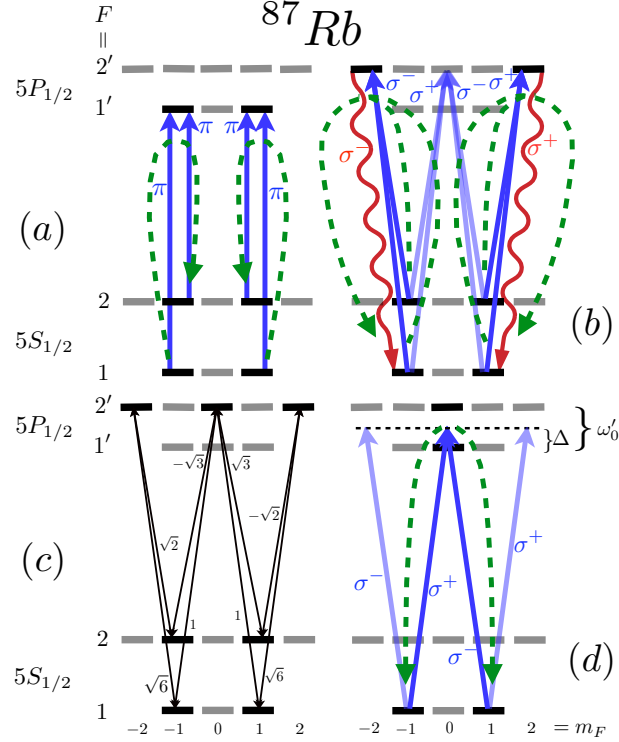


Figure 7.2: Relevant hyperfine level structure of ^{87}Rb . The cavity is resonant with the $1 \leftrightarrow 2'$ transition. (a) Two π -polarized lasers (blue lines), respectively in resonance with $2 \leftrightarrow 1'$ and $1 \leftrightarrow 1'$, drive a STIRAP (green dashed lines) that partially transfers population from $|1, \pm 1\rangle$ to $|2, \pm 1\rangle$. (b) A bichromatic σ^+/σ^- -polarized laser, with color components respectively in resonance with $1 \leftrightarrow 2'$ and $2 \leftrightarrow 2'$, state-selectively excites the atom to the $2'$ manifold. State-selection is achieved exploiting the dipole matrix elements, indicated in panel (c) in arbitrary units, and is such that excitations to the $|2, 0\rangle$ state are blocked. Thus, photon emissions (red wavy lines) only from levels $|2', \pm 2\rangle$ occur, giving rise to the effective process shown in green-dashed lines. The composed action of (a) and (b) implements transformation 7.1a. (d) If these processes are in turn preceded by a $\pi/2$ rotation between states $|1, \pm 1\rangle$, transformation 7.1b is obtained. Such rotation is driven by a Raman transition induced by a σ^+/σ^- -polarized monochromatic laser Δ -detuned from $1 \leftrightarrow 1'$. The optimal detuning is $\Delta = \omega'_0/2$, with ω'_0 being the frequency difference between $1'$ and $2'$.

7.5. Technical details

to both $|\eta^+\rangle$ and $|\eta^-\rangle$. This implies that the latter are both dark states with respect to transitions to $|2', 0\rangle$ and can therefore only be excited to $|2', \pm 2\rangle$, with the subsequent emission of a σ^\pm photon. The pulse area is π , so that the excitations $|\eta^\pm\rangle \rightarrow |2', \pm 2\rangle$ are carried out. Altogether, the mapping $|1, \pm 1\rangle \rightarrow \pm|1, \pm 1\rangle|\sigma^\pm\rangle$ is completed: transformation 7.1a in the chosen qubit encoding.

To end up with, transformation 7.1b requires the same two pulses just described but preceded by an extra one, sketched in Fig. 7.2 (d). This consists of a monochromatic σ^+/σ^- -polarized Raman laser, whose frequency is exactly halfway between the $1 \leftrightarrow 1'$ and $1' \leftrightarrow 2'$ transition frequencies. The Raman pulse area is $\pi/2$, yielding the rotation $|1, \pm 1\rangle \rightarrow \frac{1}{\sqrt{2}}(\pm|1, 1\rangle + |1, -1\rangle)$. With this, the total transformation is $|1, \pm 1\rangle \rightarrow \frac{1}{\sqrt{2}}(\pm|1, 1\rangle|\sigma^+\rangle - |1, -1\rangle|\sigma^-\rangle)$, the desired operation 7.1b.

In the latter, the choice of Raman detuning is not at all casual. For arbitrary detunings Δ , the effective Rabi frequency is proportional to $\frac{1}{\Delta} - \frac{1}{\Delta + \omega'_0}$, that is, with the contributions from the virtual mediator levels $|1', 0\rangle$ and $|2', 0\rangle$ canceling out in the large-detuning limit. On the other hand, small detunings tend to increase the risk of undesired photon-scattering events. Nevertheless, $\Delta = \omega'_0/2$ maximizes the Rabi frequency and at the same time keeps spontaneous emission within negligible levels [152].

7.5 Technical details

To minimize the chance that more than one photon is produced per sequence, excitations can be done with fast-excitation pulses, shorter than all other relevant time scales [149, 153, 23, 49]. These pulses last so short that the atom hardly has time either to decay or to transfer its excitation to the cavity before the pulse is already finished. This way the probability

of multiple excitations during the same pulse can be strongly suppressed to levels as low as 0.01% (pulse durations of 3 ns) [49], so as not to constitute a significant error source. A potential drawback could in principle be the broadening of the laser linewidth. In fact, the linewidth can become comparable to the hyperfine splitting between the $2'$ and $1'$ manifolds of ^{87}Rb , $\omega'_0 \approx 814$ MHz, making it inviable to address one without addressing the other. Therefore, unwanted transitions to $|1', 0\rangle$ could in principle occur in the excitation pulse of Fig. 7.2 (b), imposing a fundamental limitation. However, the relevant dipole matrix elements are such that $|\eta^\pm\rangle$ are dark states with respect to sublevel $|1', 0\rangle$ too. The protocol's performance is thus not affected by the broadening of the frequency spectrum.

We have presented the scheme for ^{40}Ca with the strong dipole transition $4S_{1/2} \leftrightarrow 4P_{1/2}$. Notice however that the same procedure can actually also be applied to weak quadrupole transitions, such as $4S_{1/2} \leftrightarrow 3D_{3/2}$, connected by Raman processes via $4P_{1/2}$ driven jointly by the cavity and a Raman laser [48, 52]. In such a case, the Raman detuning can be increased so as to drastically reduce the effective spontaneous-emission rate; so that – even though excitation pulses take longer – extremely high overall efficiencies are attained [52].

In turn, for both exemplary atomic species, the extremely long coherence times (seconds) of the long-lived sublevels considered allow in principle for the production of states with several photons. For ^{87}Rb , the pulses required apart from the fast-excitation pulses – Raman rotation and STIRAP – can be done altogether in a few microseconds [152, 150]. For ^{40}Ca , even in the slowest case of Raman processes mentioned above, excitation pulses are carried out with durations of the order of 120 μs .

Note also that the “disconnection” measurement on the atom via the

7.6. Feasibility

last emitted photon needs often not be done before the previously emitted N photons arrive at destination. In such cases, the $(N + 1)$ th photon is measured only upon arrival and its measurement outcome is used as a feedback to post-process the previous N measurement outcomes (provided of course that the atomic coherence is still intact). For situations where the N -qubit photonic state must be prepared before propagation, the disconnection measurement can be done with a circularly-polarized beam-splitter mounted on a movable structure. This must be introduced in the photons' path after the N th photon's passage and before the last one's. For repetition rates of up to MHz and beam waists of micrometers, a piezoelectric device coordinated with the last laser pulse can do the job.

7.6 Feasibility

Even though the protocol is in principle deterministic, the overall efficiency is in practice never unity. The total probability of emission of an entangled photon pair through the cavity output observed in Refs. [50, 154] is of 1.3%. Nevertheless, overall efficiencies of intracavity photon generation and cavity photon emission of 88% and 16.7%, respectively, per photon have been demonstrated in more recent experiments [52]. Furthermore, exhaustive simulations show that cavity photon-emission probabilities of up to 74% per photon can be reached [154].

All in all, even modest success probabilities of about 1.3% per photon pair such as the one demonstrated in Ref. [50] readily lie about 4 orders of magnitude above the typical efficiency (10^{-6}) of parametric downconversions through nonlinear crystals, used to produce entangled photon pairs in linear-optical experiments [131, 132, 136, 137, 138, 139, 140, 141, 142]. There, such low conversion efficiencies are overcome with pulsed sources of

extremely high repetition rates and laser power. In terms of net output of entangled pairs these sources comfortably beat any cavity-based method. This changes though in the multi-partite scenario. The creation of genuine multiphoton entangled states in linear-optical settings typically requires synchronized encounters of multiple entangled photons at beam splitters, where fusions into larger multi-photon pieces take place. For any fixed pulse rate and laser power, the probability of having simultaneous pairs per shot decreases exponentially with their number. To this, one must add that every beam splitter succeeds to fuse the incoming photons only half the time, yielding an extra factor of 2 in the exponent of the net decrease. This cannot be circumvented with a tour de force increase with N of the shot repetition rate and the power, for the former increases the frequency bandwidth and the latter represents an extremely unpractical experimental overhead. The cavity-based method proposed here does not bear these particular scaling limitations and may provide a relevant alternative as one increases N .

We notice further that our methods complement studies based on quantum dots [155], which feature very promising scalability properties. However, in the short term the present methods seem considerably more feasible, because – as said – the experimental platform they require has already repeatedly proved successful for the basic entanglement demonstrations. Finally, violations of multiqubit Bell inequalities of up to 10 photons are also viable with the current technology.

7.7 Efficiencies and fidelities

The main sources of inefficiencies in the emission of photons from the cavity are nonperfect intracavity photon generation and photon losses. The

7.7. Efficiencies and fidelities

former is essentially due to atomic motion (which introduces uncontrolled variations in the atom-cavity coupling) and imperfections in the pump. The latter is mostly dominated by atomic spontaneous emission and absorption or scattering from the cavity mirrors. One alternative to dominate atomic motion is to consider ionized specimens and exploit the strong electrical confinement available in ion traps. For $^{40}\text{Ca}^+$, overall efficiencies per photon of intracavity photon generation and cavity photon emission of 88% and 16.7%, respectively, have been recently demonstrated [52]. There, advantage was also taken of the reduced effective spontaneous emission rate due to large Raman detunings and the use of weak transitions. Cavity-photon loss was mostly due to mirror scattering. Another possibility for tight confinement is strong cooling and optical dipole traps [51]. Indeed, for ^{87}Rb , with appropriate cavity-atom and cavity-pump detunings, simulations show that, for realistic cavity-atom couplings such as $g/2\pi = 6.7$ MHz, the overall probability of photonic emission from the cavity can be enhanced up to 74% per photon when the atomic motion is neglected (see Chapt. 3 of Ref. [154]). These simulations take into account spontaneous emission, undesired off-resonant excitations to other levels and magnetic fields, and yield total photon losses due to atomic spontaneous emission below 15%. It is interesting to notice that such high efficiency is above the threshold—50%—of loss-tolerant photonic one-way quantum computing [156].

It is also important however to keep in mind that detection efficiencies (including non-perfect mode-matching into the fiber, transmission losses through the fiber and detector efficiencies) are usually no more than 30%. Nevertheless, non-perfect detection is inherent to any photonic-state manipulation scheme and is therefore not a figure of merit for the efficiency

of photonic-state generation schemes, such as the one proposed here.

Finally, we notice that fidelities of 86%, 87% and 93% for two-qubit maximally-entangled states have been reported (see [50, 154], [149] and [51], respectively). In turn, the minimal fidelities required for the demonstration of genuine multipartite entanglement using graph-state entanglement witnesses, or for the violation of genuine multipartite Bell inequalities, go from 75%, for 3 qubits, to approximately 53% and 35%, for GHZ and linear cluster states, respectively, for 10 qubits [157]. Thus the methods proposed here open a realistic venue for photonic multiqubit entanglement and non-locality experiments with high efficiency.

Robust-fidelity atom-photon entangling gates in the weak-coupling regime

8.1 Introduction

Optical-to-near-infrared photons constitute the most natural system to transport qubits (quantum bits) [158]. They have been dubbed “flying qubits” for the ease with which they can be sent to distant locations. On the other hand, due to their stability and relatively-long coherence properties, atoms readily offer an excellent physical realization of “stationary qubits”. Controlled interactions between photons and atoms are thus crucial for long-distance quantum communication (QC) or, more generically, quantum networking [159]. In this respect, maximally entangling gates play a special role: They are used for state-transfer from atoms to photons [160, 48, 161], or vice versa [162]; to entangle distant atoms via flying photons [96], or different flying photons via atoms [50, 51, 155, 163]; and, ultimately, for measurement-based quantum computations sequentially distributed among hybrid atomic-photonic systems [164].

The dominant approach in atom-photon interaction has focused mainly on the *strong-coupling regime*, in particular for atoms in high-finesse optical

Chapter 8. Robust-fidelity atom-photon entangling gates in the weak-coupling regime

cavities [159, 160, 48, 161, 162, 50, 51, 155, 163]. In this regime, the coherent interaction between the atom and the cavity mode strongly dominates over all other processes, including cavity leakage and atomic decay. However, despite the remarkable progress [159, 160, 48, 161, 96, 50, 51, 155, 163], the strong-coupling regime remains challenging for single cavity-emitter setups and poses a formidable challenge for cascaded arrangements, as would be required in quantum networks. An alternative approach consists of exploiting the so-called *Purcell regime* [165, 166, 167], where the cavity-atom coupling is much stronger than the atomic decay rate, but not the cavity-loss rate. The cavity is then typically referred to as a *bad cavity*, with an enhancement of the atomic spontaneous-emission rate into the cavity-output mode as the main effect (the Purcell effect), instead of coherent interactions. This particular form of *weak-coupling regime* is less technically demanding than the strong-coupling regime and can still allow for interesting state-manipulations [165, 166, 167].

In fact, this is exploited in a recent proposal [54] where an optical emitter is coupled to a one-dimensional (1D) waveguide, which can be thought of as a cavity the limit of infinite losses. The tight transversal confinement of the field by the waveguide induces a strong emitter-field coupling, which, it turns out, can yield very high Purcell factors P –indicating the system operates deep in the Purcell regime– [54]. With this, entanglement between flying photons and stationary emitters can in principle be created via resonant 1D scattering [168, 169] in the waveguide. This promising idea has several potential implementations, including atoms coupled to microscopic hollow fiber cores [170, 171] or ultra-thin optical nanofibers [172, 173], or artificial solid-state emitters, such as quantum dots [174, 175] or nitrogen-vacancy centers [176], coupled to photonic nanowires or waveg-

8.1. Introduction

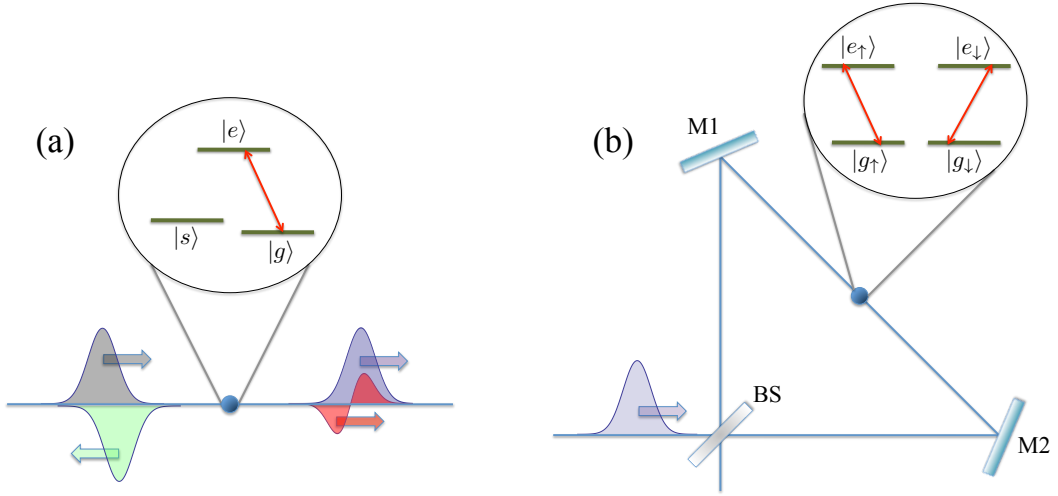


Figure 8.1: Different 1D scattering setups. (a) The original arrangement [54] uses a three-level emitter, with levels $|g\rangle$ and $|e\rangle$ coupled via the waveguide, and a third metastable level $|s\rangle$ coupled to $|e\rangle$ only via classical fields. In an ideal situation, an incident photon (black) is fully reflected (green), for $|g\rangle$, or goes freely through (blue), for decoupled state $|s\rangle$. In a faulty scattering though, there is a transmitted component (red) even for $|g\rangle$. (b) In the present setup the scatterer has two-fold degenerate ground and excited states $|g_\pm\rangle$ and $|e_\pm\rangle$, respectively, coupled by parallel transitions through orthogonally polarized waveguide photons. Even for imperfect scattering processes, if the photon is output with the correct polarization, a high-fidelity phase gate is successfully applied on the emitter. A detection of an incorrectly polarized output, on the other hand, heralds a failure. A 50/50 beam-splitter (BS) and two mirrors (M1 and M2) maximize the probability of success (see text).

uides in photonic crystals. Nonetheless, due to emitter decay and finite coupling strengths, all physical setups are restricted to finite P . Moreover, the scattering quality is in addition affected by non-zero photonic bandwidths or detunings, and so is the absorption probability, so that the scattering event may not even take place at all. These imperfections impose fundamental limitations to 1D-scattering-based approaches.

In this Chapter, we propose a practical scheme for single-emitter-single-photon interfacing that circumvents these limitations. The dominant physical errors are mapped into heralded photon losses instead of computational

errors. This is achieved with a particular scattering process that changes the polarization of photons, so that non-scattered photons are automatically discarded through polarization filtering. Furthermore, even for faulty processes, e.g. operating at low P , we find that the correct-polarization output photons imprint a phase in the internal state of the emitter. We show how to exploit this for maximally-entangling gates between stationary qubits encoded in the ground states of optical emitters in 1D waveguides and flying qubits encoded either in the polarization or the time-of-arrival (time-bin [177]) of photons. In addition, the gates allow for the storage or retrieval of flying-qubit states, as well as for measurement-based quantum computations sequentially distributed among the single-emitter quantum memories.

8.2 Photons scattering off two-level emitters in 1D

A two-level emitter, with ground and excited states $|g\rangle$ and $|e\rangle$, respectively, dipole-coupled to a 1D continuum of electromagnetic modes can, ideally, act as a perfect mirror for resonant single photons [169]. The photons are fully reflected as a result of the destructive interference between the reemitted and the (non-absorbed) incident wavefunctions. More technically, we say that for an incident photon in a state $|\Psi_i\rangle = \int dz\psi(z,t)|z\rangle$, a perfect reflection leads to $|\Psi_r\rangle = -\int dz\psi(-z,t)|z\rangle$. On the other hand, a perfectly transmitted (freely propagating) photon remains in $|\Psi\rangle = \int dz\psi(z,t)|z\rangle$. Here, z is the spatial coordinate along the waveguide, conventionally taken as positive to the right, negative to the left, and with the origin $z = 0$ at the atom's position; t is the time, with the origin $t = 0$ at the scattering

8.2. Photons scattering off two-level emitters in 1D

instant; $|z\rangle$ is the state of a photon localized at z ; and $\psi(z, t) \equiv \psi(t - z/c)$ is a normalized wave function, where parameter c is the photonic group velocity inside the waveguide ($c > 0$ for photons propagating from left to right, and $c < 0$ otherwise). The global minus sign in the definition of $|\Psi_r\rangle$ comes from the absorption and subsequent reemission.

Perfect 1D scattering can be used to create emitter-photon qubit entanglement: Consider an extra metastable level $|s\rangle$ decoupled from the waveguide light [54] [see Fig. 8.1 (a)]. A stationary qubit can then be encoded in the stable atomic manifold, $\{|0\rangle_a \doteq |s\rangle, |1\rangle_a \doteq |g\rangle\}$, and a flying qubit in the spatial wavefunction of single photons, $\{|0\rangle_p \doteq |\Psi^R\rangle, |1\rangle_p \doteq |\Psi^L\rangle\}$, where $|\Psi^R\rangle$ and $|\Psi^L\rangle$ represent incident wavepackets with the same waveform but propagating from left to right and viceversa, respectively. For the emitter in $|1\rangle_a$, a perfect reflection causes $|\Psi^{R(L)}\rangle \rightarrow -|\Psi^{L(R)}\rangle$. Therefore, since $|0\rangle_a$ is decoupled, a perfect process executes the maximally-entangling gate $|\mu\rangle_a |\varphi\rangle_p \rightarrow (-X_a)^\mu |\mu\rangle_a |\varphi\rangle_p$, where $|\varphi\rangle_p$ is any photonic-qubit state, X_p the corresponding first Pauli matrix and $\mu = 0$ or 1 .

In practice however, the reemitted amplitude is weaker than the incident one and cannot cancel it. There is always a transmitted part [54]. For incident state $|\Psi_i\rangle$, the photon comes out in $|\Psi_f\rangle = |\Phi_t\rangle + |\Phi_r\rangle$, with transmitted and reflected components $|\Phi_t\rangle = \int dz \phi_t(z, t) |z\rangle$ and $|\Phi_r\rangle = \int dz \phi_r(-z, t) |z\rangle$, respectively, with [168, 169, 54]

$$\phi_t(z, t) = \psi(z, t) + \phi_r(z, t), \quad (8.1a)$$

$$\begin{aligned} \phi_r(z, t) = & -\frac{\Gamma_{1D}}{2} \int_0^{t-z/c} dt' \\ & \times e^{-i(\omega_0 - i\Gamma/2)(t-z/c-t')} \psi(0, t'). \end{aligned} \quad (8.1b)$$

Here, $\Gamma \doteq \Gamma_{1D} + \Gamma'$ is the total atomic decay rate, with Γ_{1D} (Γ') the rate

Chapter 8. Robust-fidelity atom-photon entangling gates in the weak-coupling regime

of atomic decay into the waveguide (all channels but the waveguide, e.g., emission into free space, or non-radiative dissipation), and ω_0 is the atomic transition frequency. $|\Psi_f\rangle$ refers to the state-component left in the waveguide, so it is normalized only when the Purcell factor $P \doteq \Gamma_{1D}/\Gamma'$ is infinite. In particular, for finite Γ' and $\Gamma_{1D} \rightarrow \infty$, a Dirac delta appears in the integrand of 8.1b, so that $\phi_r(z, t) = -\psi(0, t - z/c) \equiv -\psi(t - z/c) \equiv -\psi(z, t)$ and one has a perfect reflection: $|\Psi_f\rangle = |\Phi_r\rangle = |\Psi_r\rangle$. Accordingly, the probability of photon loss is $\kappa \doteq 1 - \langle \Psi_f | \Psi_f \rangle$.

Apart from P , another relevant figure of merit is the reflection fidelity $f \doteq -\langle \Psi_r | \Phi_r \rangle$, which measures how close to a perfect reflection the process is and can also be affected by frequency detunings or non-zero photonic bandwidths. In terms of P and f , the probability of photon transmission and reflection are given respectively by [168, 169, 54] the transmittance $\mathcal{T} \doteq \langle \Phi_t | \Phi_t \rangle = 1 - \Re f [2 - 1/(1 + P^{-1})]$ and the reflectance $\mathcal{R} \doteq \langle \Phi_r | \Phi_r \rangle = \Re f / (1 + P^{-1})$. A maximally-entangling gate can only be obtained for $P \rightarrow \infty$ and $f = 1$, because only then does one have $\mathcal{R} = 1$ (so that $|\Psi^{R(L)}\rangle \rightarrow -|\Psi^{L(R)}\rangle$). The lower \mathcal{R} is, the lower the fidelity of the resulting gate is.

As a simple example, imagine an incident photon spontaneously emitted, at rate γ , by a distant emitter. In this case the photon has a half-exponential waveform of bandwidth γ . Eq. 8.1b is then immediately integrated to yield $f = (1 + P^{-1} + \gamma/\Gamma_{1D} - i2\delta/\Gamma_{1D})^{-1}$, where δ is the detuning from ω_0 . Notice that even if $P \rightarrow \infty$ and $\delta \approx 0$, already for $\gamma \approx \Gamma_{1D}$, f (and therefore also \mathcal{R}) decreases to 1/2. This would indeed be the case when emitter and scatterer are of the same species. More generally, this limitation is a serious drawback for short pulses, as those used for instance in time-bin qubits [158, 177].

8.3 High-fidelity interaction from imperfect processes

Consider now a four-level emitter, with degenerate ground and excited states $|g_{\pm}\rangle$ and $|e_{\pm}\rangle$, as depicted in Fig. 8.1 (b). These are coupled via parallel dipole transitions $|g_{\pm}\rangle \leftrightarrow |e_{\pm}\rangle$, associated to the absorption from, or emission to, the waveguide of σ^{\pm} -polarized photons. σ^+ and σ^- denote two orthogonal polarizations, as for instance the right- and left-handed circular polarizations along the waveguide. The waveguide is taken as the atomic quantization axis. An incident photon of spatial wavefunction $|\Psi_i\rangle$ and polarization σ^{\pm} scatters as

$$|g_{\pm}\rangle|\Psi_i\rangle|\sigma^{\pm}\rangle \rightarrow |g_{\pm}\rangle|\Psi_f\rangle|\sigma^{\pm}\rangle, \quad (8.2a)$$

$$|g_{\mp}\rangle|\Psi_i\rangle|\sigma^{\pm}\rangle \rightarrow |g_{\mp}\rangle|\Psi_i\rangle|\sigma^{\pm}\rangle. \quad (8.2b)$$

If, instead, the photon is in the linear-polarization state $|h\rangle \doteq (|\sigma^+\rangle + |\sigma^-\rangle)/\sqrt{2}$, transformations 8.2 yield

$$|g_{\pm}\rangle|\Psi_i\rangle|h\rangle \rightarrow \frac{1}{2}|g_{\pm}\rangle[(|\Psi_f\rangle + |\Psi_i\rangle)|h\rangle \pm (|\Psi_f\rangle - |\Psi_i\rangle)|v\rangle], \quad (8.3)$$

where $|v\rangle \doteq (|\sigma^+\rangle - |\sigma^-\rangle)/\sqrt{2}$ is the vertical linear-polarization state. The scattering generates now a v -polarized component. More importantly, while for h -polarized outgoing photons nothing happens to the emitter, a state-dependent π -phase shift on the emitter accompanies the v -polarized component of 8.3. This phase shift will be the basis of our entangling gates.

To maximize the v -polarized component, the input photon is coherently split into two halves that simultaneously scatter off the emitter, incident

Chapter 8. Robust-fidelity atom-photon entangling gates in the weak-coupling regime

from a different side each, as shown in Fig. 8.1 (b). Then, the reflected and transmitted components of each half are coherently joined all back into a single packet, which exits the BS through the same output mode it was input. Then, $(|\Psi_i\rangle - |\Psi_f\rangle)/2 = -|\Phi_r\rangle$, and discarding the h -polarized output from 8.3, one gets

$$|\varphi\rangle_a |\Psi_i\rangle |h\rangle \rightarrow -Z_a |\varphi\rangle_a |\Phi_r\rangle |v\rangle, \quad (8.4)$$

where $|\varphi\rangle_a$ is any atomic-qubit state in the basis $\{|0\rangle_a \doteq |g_-\rangle, |1\rangle_a \doteq |g_+\rangle\}$. For perfect scattering processes $|\Phi_r\rangle = -|\Psi_i\rangle$ and therefore the success probability $p \doteq \langle \Phi_r | \Phi_r \rangle$ is 1. No photon is lost then. On the other hand, for imperfect processes, with $P < \infty$, $|\Phi_r\rangle \neq -|\Psi_i\rangle$ and output photons with h polarization are detected. These are discarded and the corresponding gate runs fail. However, the important thing is that the fidelity of gate 8.4 is not altered, only p is. We show next how to exploit successful Z_a gates for high-fidelity entangling schemes.

8.4 Entangling gate for time-bin flying qubits

The first photonic-qubit encoding we consider is the time of arrival [177], consisting of incident pulses that arrive either at some “early” scattering time t_e , defining the state $|\Psi_{t_e}\rangle$, at some “later” time $t_l > t_e$ [177], defining $|\Psi_{t_l}\rangle$, or in any superposition of the latter two states. The qubit basis is $\{|0\rangle_p \doteq |\Psi_{t_e}\rangle, |1\rangle_p \doteq |\Psi_{t_l}\rangle\}$. The final ingredient of the protocol is the application of a Hadamard gate H_a to the atomic qubit between t_e and t_l : If the photon arrives at t_e , the emitter undergoes first the Z_a and then H_a , whereas if it arrives at t_l , the order of the gates is reversed. Thus, since Z_a and H_a do not commute, the overall stationary-qubit gate is controlled by

8.5. Entangling gate for polarization flying qubits

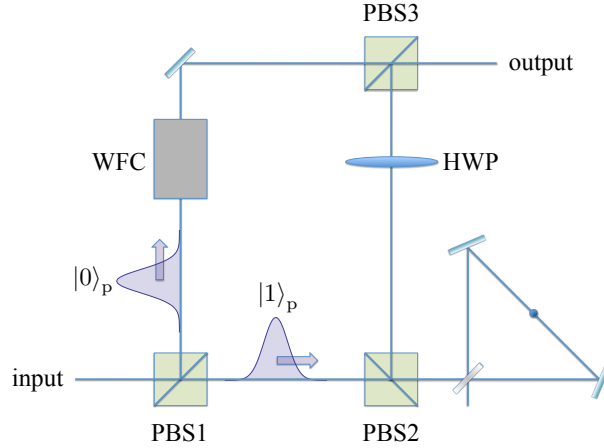


Figure 8.2: Interferometric setup for polarization flying-qubits. Only component $|1\rangle_p$ interacts with the scatterer. For successful interactions, $|1\rangle_p$ is reflected up the interferometer by PBS2 and joins $|0\rangle_p$ at PBS3. At the output, maximally entangling gate 8.6 between the flying and the stationary qubits is implemented. For unsuccessful interactions, $|1\rangle_p$ comes back out through PBS2 and PBS1, which heralds a gate failure. Legends: PBS: polarizing BS; HWP: half-wave plate; WFC: waveform corrector. See text.

the flying qubit's state. The composite unitary transformation is

$$U_{ap} = |0\rangle_p \langle 0| \otimes H_a Z_a + |1\rangle_p \langle 1| \otimes Z_a H_a \quad (8.5)$$

is local-unitarily equivalent to the well-known controlled-phase gate 8.6, defined below, and is therefore also a maximally-entangling gate.

8.5 Entangling gate for polarization flying qubits

The other encoding considered is photon polarization. We define it by $\{|0\rangle_p \doteq |v\rangle, |1\rangle_p \doteq |h\rangle\}$. In this case, the active application of H_a is replaced with the passive interferometer shown in Fig. 8.2. First, the $|0\rangle_p$ and $|1\rangle_p$ components of an incident photon are spatially split by a polarizing

Chapter 8. Robust-fidelity atom-photon entangling gates in the weak-coupling regime

beam splitter (PBS). $|1\rangle_p$ goes through both PBSs 1 and 2 towards the scattering setup, whereas component $|0\rangle_p$ is reflected up the other arm of the interferometer by PBSs 1. For unsuccessful events, $|1\rangle_p$ exits the scattering setup with the same polarization, h . It is therefore transmitted back through PBSs 2 and 1 and detected in h as before, heralding the failure of the gate run. On the other hand, for successful Z_a gates the polarization is flipped. Since it is then v -polarized, the pulse is reflected up by PBS2, after which it is rotated back to $|h\rangle$ by a half-wave plate (HWP). Finally, $|0\rangle_p$ and $|1\rangle_p$ are rejoined by PBS3. At the output of PBS3, the total composite unitary transformation is the controlled-phase gate

$$U_{ap} = |0\rangle_p \langle 0| \otimes 1_a + |1\rangle_p \langle 1| \otimes Z_a. \quad (8.6)$$

For successful events of imperfect processes, i.e. where the polarization is flipped but $|\Phi_r\rangle \neq -|\Psi_i\rangle$ in 8.4, the spatial wave functions of the packets meeting at PBS3 no longer coincide. So, unless the waveforms are matched, the output polarization qubit may be correlated with different spatial states. An experimentally relevant situation where this can be easily overcome is for incident photons with bandwidth much narrower than Γ_{1D} , so that $\psi(z, t)$ can be approximated in 8.1b by a plane wave. In this case the spatial waveform associated to $|1\rangle_p$ is $|\Phi_r\rangle \approx -k|\Psi_i\rangle$, with $|k| < 1$. To compensate for this, a waveform corrector (WFC) in the $|0\rangle_p$ arm maps $|\Psi_i\rangle$ to $k|\Psi_i\rangle$. This slightly further decreases the overall success probability, but leaves the fidelity intact. When the photon-atom detuning δ is zero, $k \in [0, 1)$ and the WFC consists of an attenuator (e.g., a BS) of transmissivity k . If $\delta \neq 0$, $k \in \mathbb{C}$ and WFC simply includes also a phase modulator. In addition, the WFC may also include a delay to make $|0\rangle_p$ arrive simultaneously with $|1\rangle_p$ at PBS3. In the general situation $|\Phi_r\rangle \neq |\Psi_i\rangle$, WFC

8.6. Single-emitter quantum memories and sequential measurement-based quantum computations

can be realized by a second scattering block, identical to that of Fig. 8.1 b), but with the emitter permanently in state $|g_+\rangle$ (or $|g_-\rangle$), preceded by a quarter waveplate to rotate $|0\rangle_p$ to $|\sigma^+\rangle$ (or $|\sigma^-\rangle$). With this, the associated wavepacket is mapped from $|\Psi_i\rangle$ to $|\Phi_r\rangle$ without becoming entangled with the second scatterer, achieving the desired waveforms matching.

8.6 Single-emitter quantum memories and sequential measurement-based quantum computations

The present maximally entangling gates, together with single-qubit gates and measurements, allow for efficient measurement-based quantum computations sequentially distributed (by the flying qubits) among different stationary qubits of a quantum network [164, 178]. The underlying model is the seminal one-way quantum computer [19], but the approaches of [164, 178] have the advantages that (i) only the pieces of the cluster relevant for the particular computation are created (and almost immediately consumed) [178], (ii) the number of required stationary qubits is drastically smaller than in the one-way model [178], and (iii) every flying qubit needs interact with at most two stationary ones and typically with only one [164, 178].

Since these models are universal [164, 178], they include for instance the preparation of multipartite entangled states shared among different scatterers, or simply the storage, and later retrieval, of flying-qubit states, so that each emitter works as a quantum memory. The storage procedure consists essentially of maximally entangling the incident photon with the emitter, with a subsequent measurement on the outgoing photon. The

retrieval, in turn, is done by maximally entangling a second photon with the emitter-qubit, in the stored state, followed by a measurement on the emitter. As a result, the second photon takes the stored state away with it.

8.7 Feasibility

For quantum dots coupled to photonic-crystal waveguides, $P > 20$ has been demonstrated [174]. This corresponds to success probabilities $p > 0.95$, providing thus a candidate for the implementation of the proposed schemes. Another potential setup is given by atoms coupled to ultra-thin tapered optical nanofibers [172, 173]. The modest Purcell factors ($P \lesssim 1$) available there already yield $p \lesssim 0.5$. On the other hand, even though plasmons in metallic nanowires can render very high P , they do not bear two orthogonal polarizations, and are therefore not optimal for our aims. The decay rates observed in [174] are such that $\Gamma_{1D} > 1\text{GHz}$, so that photons with pulse durations around tens of ns can scatter off quantum dots with excellent reflection fidelities.

These durations are longer than those of typical time-bin encodings [177]. However, the required time delays can be achieved either with longer interferometers or with an empty cavity in one of the interferometric arms, for instance. In addition, the Hadamard gate needed between the two time-bin components can be implemented in just picoseconds [179]. Then, the total duration of the scattering gate would be comparable to the coherence time of bare quantum dots [180, 179]. Nevertheless, experiments have already demonstrated that this can be enhanced by up to two orders of magnitude with quantum control of the surrounding nuclear-spin bath [181, 182].

8.8. Heralded losses versus infidelities

Finally, coupling single atoms to nanofibers stably is still challenging, but the required techniques display a remarkably fast progress [172, 173]. Besides, in return, atoms readily provide coherence times as high as seconds.

8.8 Heralded losses versus infidelities

The proposed gates apply directly to the storage or retrieval of flying-qubit states, and to measurement-based multipartite-state preparations, or generic quantum computations, sequentially distributed among distant emitters [164, 178]. As a matter of fact, for quantum information and communication applications, turning computational errors into losses is an extremely advantageous property. While the formers reduce the fidelity, the latter reduce only the efficiency, which is easier to circumvent. For example, the most optimistic thresholds of error rate per gate tolerable for fault-tolerant quantum computing are below 3% [148]. In contrast, remarkably, the one-way model [19] for quantum computation, as well [178] as the sequential counterparts considered here, can cope with particle loss rates of close to 50% [156] and heralded gate-failure rates exceeding 90% [111, 116].

Conclusions and Outlook

In this thesis, we investigated how to process quantum information without precise manipulations of interactions over a large number of qubits and a couple of schemes for photonic-qubit-materiel-qubit interfaces.

In Chapter 2, we proposed a 2D and a 3D gapped system, whose ground state is entangled based on a factorized Hamiltonian. It is useful to find other practical systems can offer same figures. With a factorized Hamiltonian, quantum computing can be performed without the need to switch off interactions. The ground state can be reduced to a deterministic cluster state, in contrast to AKLT like systems where cluster states are obtained with stochastic structures. Errors induced by thermal fluctuations can be corrected as long as the temperature is below a critical threshold. There are other choices of $A_{\mathbf{b}}^{\alpha}$ and $B_{\mathbf{b}}^{\alpha}$ that satisfy conditions of spin-1/2 operators. By replacing the center particle with different spin systems, i.e. spin- $m/2$ particles, one can get different spatial connectivities that each qubit is connected to m other qubits in the cluster state. Thereby, it can be generalized to 3D and more complicated configurations.

The MBQC predicts a new phase of matters, in which states have the ability of universal quantum computing in the manner of measuring individual particles. In previous studies, the transition of the quantum-computing ability depends on the error-correction code that is used for eliminating errors induced by parameter misalignments and thermal fluctuations. Using

the theory of matrix product states [183], it may be possible to determine the intrinsic transition between the universal resource phase and the normal phase. Most of known two-body-interaction Hamiltonians, whose unique ground states are universal resources of the MBQC, are models of multi-state particles rather than two-state particles (qubits), while the latter one is more easy to be manipulated. Hence, it would be interesting to reduce the complexity of particle internal states and find realistic two-qubit interactions for the ground-code MBQC. An example of the two-qubit-interaction Hamiltonian is proposed in Ref. [56], in which the five-body interaction for the cluster state can be obtained effectively from two-body interactions via perturbations. This perturbation must however be weak to get an approximate cluster state. However, a weak perturbation implies a small energy gap between the ground state and the first excited state. This means that the system should be cooled to a sufficiently low temperature according to the small perturbative energy gap. By investigating the intrinsic transition, it may be possible to boost the tolerable perturbation strength, i.e., the energy gap, to a more realistic value.

In Chapter 3, we determined the threshold for quantum computation when two-qubit gates are non-deterministic. A specific case is that of a fully distributed machine, i.e. a network of components each of which contains only a single qubit. We find that it is tolerable if entanglement operations over the network fail with a rate exceeding 90%, provided that such failures are heralded. The tolerable rate of un-heralded errors is 2×10^{-4} . Our analysis should allow experimentalists to determine if single-qubit components are feasible with their particular approach, or if instead multi-qubit components must be adopted. In Chapter 4, we described an approach to distributed quantum computing using a machine with three qubits in

each of its nodes. We showed that even such a limited system can offer robustness through the process of purifying the infidelity on the network (i.e. internode) entangling operation. While our DQC-3 protocol cannot quite match the performance of the recently described DQC-4 procedure [118], the significant saving in node complexity may be attractive to experimentalists. For example, an NV- centre with an optically active electron state and two coupled nuclear spins (say, one nitrogen and one carbon-13 nucleus) can suffice to realise the protocol described here.

For the distributed quantum computing, while the fidelity requirement of probabilistic EOs has approached the realistic level, the requirement of local deterministic operations are at least one order of magnitude higher than it of the quantum computing based on a deterministic architecture. So, the next effort would be boosting the fidelity requirement of local operations by considering multi-qubit parity projection distillations. Throughout previous studies, it is assumed that all forms of error are equally likely; in reality, in a given physical system some errors may be more prevalent. For example phase errors on the network channel might be more common than flip errors, and similarly the local gates within cells may suffer specific kinds of noise, e.g. correlated noise. Any such bias in error occurrences is ‘good news’ in that it can potentially be exploited by adapting the protocols, and in this way the error thresholds might be further increased.

In Chapter 5, we described an advanced protocol for distributing entanglement through the use of repeater stations which together generate a topologically protected cluster state. We find that the approach is remarkably robust to errors, while the resource cost within each repeater scales only logarithmically with the total distance over which entanglement is to be shared. In Chapter 6, we proposed a protocol for entangling

remote qubits on a two-dimensional noisy quantum network, which is scalable when the number of quantum memories in each node of the network is fixed. In our protocol, the communication rate decreases only logarithmically with the distance. The tolerable errors in the protocol presented here are three orders of magnitude better than possible protocols based on one-dimensional fault-tolerant quantum-computation schemes. In this paper, we investigated the case in which each node has a five-qubit quantum memory. Because every node is interacting with only one other node at one time, memory qubits can be reused, and indeed, two qubits per node is sufficient. With more memories, entanglement distillation protocols can be used to improve the effective fidelity of quantum channels [184], i.e. increase the error-rate threshold.

In Chapter 7, we proposed a family of protocols for the creation of photonic GHZ and linear cluster states emitted from a single atom – or ion – coupled to an optical cavity field. These protocols are based on laser pulses with different polarizations and exploit the atomic natural dipole-transition elements to state-selectively achieve the desired transitions. The methods are in principle deterministic.

In Chapter 8, We proposed a simple scattering configuration for photons and optical emitters in 1D waveguides. This allows for probabilistic maximally entangling gates between stationary qubits encoded in the emitters' ground states and flying qubits encoded in photonic polarization or time-bin. The scattering process tags faulty interactions with an orthogonal output polarization, which can be immediately detected and discarded, rendering a built-in error-heralding mechanism. This turns gate infidelities from weak couplings, atomic decay into undesired modes, frequency mismatches, or finite photon-pulse bandwidths, into heralded losses. The

resulting gates then either succeed with perfect fidelity, or fail in a heralded manner, but are in principle never faulty. We have estimated success probabilities for realistic current-technology setups that range from $\lesssim 50\%$ to as high as 95% .

The hybrid gate via scattering has been demonstrated with a quantum dot coupled to a photonic crystal cavity [185]. However, the fidelity in the current experiment is only about 60% . It may be possible to improve the fidelity by using my protocol in cavity-QED setups. My present protocol of the hybrid gate can detect and correct errors induced by inefficient couplings and spontaneous emissions of atoms. Another important source of errors is the pure dephasing of atoms, which is more crucial for solid-state artificial atoms, e.g., quantum dots, nitrogen-vacancy centres, and superconducting qubits. To investigate the effect of the pure dephasing, I am developing a method to analyse the atom-photon scattering in a waveguide, where the atomic state undergoes a relaxation process driven by a master equation describing the pure dephasing.

Bibliography

- [1] Michael A. Nielsen and Isaac L. Chuang. *Quantum Computation and Quantum Information*. Cambridge University Press; 1 edition (January 1, 2004), 2004.
- [2] David Beckman, Amalavoyal N. Chari, Srikrishna Devabhaktuni, and John Preskill. Efficient networks for quantum factoring. *Phys. Rev. A*, 54:1034, 1996.
- [3] Wolfgang Paul. Electromagnetic traps for charged and neutral particles. *Rev. Mod. Phys.*, 62:531, 1990.
- [4] D. J. Wineland, C. Monroe, W. M. Itano, D. Leibfried, B. E. King, and D. M. Meekhof. Experimental issues in coherent quantum-state manipulation of trapped atomic ions. *J. Res. Natl. Inst. Stand. Technol.*, 103:259, 1998.
- [5] Rainer Blatt and David Wineland. Entangled states of trapped atomic ions. *Nature*, 453:1008, 2008.
- [6] J. I. Cirac and P. Zoller. Quantum computations with cold trapped ions. *Phys. Rev. Lett.*, 74:4091, 1995.
- [7] C. Monroe, D. M. Meekhof, B. E. King, W. M. Itano, and D. J. Wineland. Demonstration of a fundamental quantum logic gate. *Phys. Rev. Lett.*, 75:4714, 1995.
- [8] J. I. Cirac and P. Zoller. A scalable quantum computer with ions in an array of microtraps. *Nature*, 404:6778, 2000.
- [9] H. Häffner, W. Hänsel, C. F. Roos, J. Benhelm, D. Chek al kar, M. Chwalla, T. Körber, U. D. Rapol, M. Riebe, P. O. Schmidt, C. Becher, O. Gühne, W. Dür, and R. Blatt. Scalable multiparticle entanglement of trapped ions. *Nature*, 438:643, 2005.
- [10] J. Chiaverini, J. Britton, D. Leibfried, E. Knill, M. D. Barrett, R. B. Blakestad, W. M. Itano, J. D. Jost, C. Langer, R. Ozeri, T. Schaetz, and D. J. Wineland. Implementation of the semiclassical quantum fourier transform in a scalable system. *Science*, 308:997, 2005.
- [11] B. E. Kane. A silicon-based nuclear spin quantum computer. *Nature*, 393:133, 1998.
- [12] R. Hanson, L. P. Kouwenhoven, J. R. Petta, S. Tarucha, and L. M. K. Vandersypen. Spins in few-electron quantum dots. *Rev. Mod. Phys.*, 79:1217, 2007.
- [13] Y. Nakamura, Yu Pashkin, and J. S. Tsai. Coherent control of macroscopic quantum states in a single-cooper-pair box. *Nature*, 398:786, 1999.
- [14] I. Chiorescu, Y. Nakamura, C. J. P. M. Harmans, and J. E. Mooij. Coherent quantum dynamics of a superconducting flux qubit. *Science*, 229:1869, 2003.

- [15] Adam Gali, Maria Fyta, and Efthimios Kaxiras. *Ab initio* supercell calculations on nitrogen-vacancy center in diamond: Electronic structure and hyperfine tensors. *Phys. Rev. B*, 77:155206, 2008.
- [16] Gopalakrishnan Balasubramanian, Philipp Neumann, Daniel Twitchen, Matthew Markham, Roman Kolesov, Norikazu Mizuochi, Junichi Isoya, Jocelyn Achard, Johannes Beck, Julia Tissler, Vincent Jacques, Philip R. Hemmer, Fedor Jelezko, and Jörg Wrachtrup. Ultralong spin coherence time in isotopically engineered diamond. *Nature Mater*, 8:383, 2009.
- [17] L. Childress, M. V. Gurudev Dutt, J. M. Taylor, A. S. Zibrov, F. Jelezko, J. Wrachtrup, P. R. Hemmer, and M. D. Lukin. Coherent dynamics of coupled electron and nuclear spin qubits in diamond. *Science*, 314:5797, 2006.
- [18] P. Neumann, R. Kolesov, B. Naydenov, J. Beck, F. Rempp, M. Steiner, V. Jacques, G. Balasubramanian, M. L. Markham, D. J. Twitchen, S. Pezzagna, J. Meijer, J. Twamley, F. Jelezko, and J. Wrachtrup. Quantum register based on coupled electron spins in a room-temperature solid. *Nature Physics*, 6:249, 2010.
- [19] Robert Raussendorf and Hans J. Briegel. A one-way quantum computer. *Phys. Rev. Lett.*, 86:5188, 2001.
- [20] Robert Raussendorf, Daniel E. Browne, and Hans J. Briegel. Measurement-based quantum computation on cluster states. *Phys. Rev. A*, 68:022312, 2003.
- [21] H. J. Briegel, D. E. Browne, W. Dür, R. Raussendorf, and M. Van den Nest. Measurement-based quantum computation. *Nature Physics*, 5:19, 2009.
- [22] Maarten Van den Nest, Akimasa Miyake, Wolfgang Dür, and Hans J. Briegel. Universal resources for measurement-based quantum computation. *Phys. Rev. Lett.*, 97:150504, 2006.
- [23] D. L. Moehring, M. J. Madsen, K. C. Younge, R. N. Kohn, Jr., P. Maunz, L.-M. Duan, C. Monroe, and B. B. Blinov. Quantum networking with photons and trapped atoms. *J. Opt. Soc. Am. B*, 24:300, 2007.
- [24] S. C. Benjamin, B. W. Lovett, and J. M. Smith. Prospects for measurement-based quantum computing with solid state spins. *Laser & Photonics Reviews*, 3:556, 2009.
- [25] P. A. Hiskett, D. Rosenberg, C. G. Peterson, R. J. Hughes, S. Nam, A. E. Lita, A. J. Miller, and J. E. Nordholt. Long-distance quantum key distribution in optical fibre. *New J. Phys.*, 8:193, 2006.
- [26] Tobias S. Manderbach, Henning Weier, Martin Fürst, Rupert Ursin, Felix Tiefenbacher, Thomas Scheidl, Josep Perdigues, Zoran Sodnik, Christian Kurtsiefer, John G. Rarity, Anton Zeilinger, and Harald Weinfurter. Experimental demonstration of free-space decoy-state quantum key distribution over 144km. *Phys. Rev. Lett.*, 98:010504, 2007.

Bibliography

- [27] R. Ursin, F. Tiefenbacher, T. Schmitt-Manderbach, H. Weier, T. Scheidl, M. Lindenthal, B. Blauensteiner, T. Jennewein, J. Perdigues, P. Trojek, B. Ömer, M. Fürst, M. Meyenburg, J. Rarity, Z. Sodnik, C. Barbieri, H. Weinfurter, and A. Zeilinger. Entanglement-based quantum communication over 144km. *Nature Physics*, 3:481, 2007.
- [28] A. R. Dixon, Z. L. Yuan, J. F. Dynes, A. W. Sharpe, and A. J. Shields. Gigahertz decoy quantum key distribution with 1 mbit/s secure key rate. *Opt. Express*, 16:18790, 2008.
- [29] H. J. Briegel, W. Dür, J. I. Cirac, and P. Zoller. Quantum repeaters: The role of imperfect local operations in quantum communication. *Phys. Rev. Lett.*, 81:5932, 1998.
- [30] Liang Jiang, J. M. Taylor, Kae Nemoto, W. J. Munro, Rodney Van Meter, and M. D. Lukin. Quantum repeater with encoding. *Phys. Rev. A*, 79:032325, 2009.
- [31] Austin G. Fowler, David S. Wang, Charles D. Hill, Thaddeus D. Ladd, Rodney Van Meter, and Lloyd C. L. Hollenberg. Surface code quantum communication. *Phys. Rev. Lett.*, 104:180503, 2010.
- [32] Antonio Acín, J. Ignacio Cirac, and Maciej Lewenstein. Entanglement percolation in quantum networks. *Nature Physics*, 3:256, 2007.
- [33] Robert Raussendorf, Sergey Bravyi, and Jim Harrington. Long-range quantum entanglement in noisy cluster states. *Phys. Rev. A*, 71:062313, 2005.
- [34] S. Perseguers, L. Jiang, N. Schuch, F. Verstraete, M. D. Lukin, J. I. Cirac, and K. G. H. Vollbrecht. One-shot entanglement generation over long distances in noisy quantum networks. *Phys. Rev. A*, 78:062324, 2008.
- [35] Sébastien Perseguers. Fidelity threshold for long-range entanglement in quantum networks. *Phys. Rev. A*, 81:012310, 2010.
- [36] Andrzej Grudka, Michal Horodecki, Pawel Horodecki, Pawel Mazurek, Lukasz Pankowski, and Anna Przysieszna. Long distance quantum communication over noisy networks. arXiv:1202.1016, 2012.
- [37] G. John Lapeyre Jr., Jan Wehr, and Maciej Lewenstein. Enhancement of entanglement percolation in quantum networks via lattice transformations. *Phys. Rev. A*, 79:042324, 2009.
- [38] Sébastien Perseguers, J. Ignacio Cirac, Antonio Acín, Maciej Lewenstein, and Jan Wehr. Entanglement distribution in pure-state quantum networks. *Phys. Rev. A*, 77:022308, 2008.
- [39] S. Perseguers, D. Cavalcanti, G. J. Lapeyre, Jr., M. Lewenstein, and A. Acín. Multipartite entanglement percolation. *Phys. Rev. A*, 81:032327, 2010.
- [40] S. Broadfoot, U. Dorner, and D. Jaksch. Entanglement percolation with bipartite mixed states. *EuroPhys. Lett.*, 88:50002, 2009.

- [41] S. Broadfoot, U. Dorner, and D. Jaksch. Singlet generation in mixed-state quantum networks. *Phys. Rev. A*, 81:042316, 2010.
- [42] S. Broadfoot, U. Dorner, and D. Jaksch. Long distance entanglement generation in 2d networks. arXiv:1008.3584, 2010.
- [43] G. J. Lapeyre Jr., S. Perseguers, M. Lewenstein, and A. Acín. Distribution of entanglement in networks of bi-partite full-rank mixed states. arXiv:1108.5833, 2011.
- [44] A. M. Stephens, A. G. Fowler, and L. C. L. Hollenberg. Universal fault tolerant quantum computation on bilinear nearest neighbor arrays. arXiv:0702201, 2007.
- [45] Ashley M. Stephens and Zachary W. E. Evans. Accuracy threshold for concatenated error detection in one dimension. *Phys. Rev. A*, 80:022313, 2009.
- [46] Arno Rauschenbeutel, Gilles Nogues, Stefano Osnaghi, Patrice Bertet, Michel Brune, Jean-Michel Raimond, and Serge Haroche. Step-by-step engineered multiparticle entanglement. *Science*, 288:2024, 2000.
- [47] J. McKeever, A. Boca, A. D. Boozer, J. R. Buck, and H. J. Kimble. Experimental realization of a one-atom laser in the regime of strong coupling. *Nature*, 425:268, 2004.
- [48] Matthias Keller, Birgit Lange, Kazuhiro Hayasaka, Wolfgang Lange, and Herbert Walther. Continuous generation of single photons with controlled waveform in an ion-trap cavity system. *Nature*, 431:1075, 2004.
- [49] J. Bochmann, M. Mücke, G. Langfahl-Klabes, C. Erbel, B. Weber, H. P. Specht, D. L. Moehring, and G. Rempe. Fast excitation and photon emission of a single-atom-cavity system. *Phys. Rev. Lett.*, 101:223601, 2008.
- [50] Tatjana Wilk, Simon C. Webster, Axel Kuhn, and Gerhard Rempe. Single-atom single-photon quantum interface. *Science*, 317:488, 2007.
- [51] B. Weber, H. P. Specht, T. Müller, J. Bochmann, M. Mücke, D. L. Moehring, and G. Rempe. Photon-photon entanglement with a single trapped atom. *Phys. Rev. Lett.*, 102:030501, 2009.
- [52] H. G. Barros, A. Stute, T. E. Northup, C. Russo, P. O. Schmidt, and R. Blatt. Deterministic single-photon source from a single ion. *New J. Phys.*, 11:103004, 2009.
- [53] D. M. Greenberger, M. A. Horne, and A. Zeilinger. *Bell's Theorem, Quantum Theory and Conceptions of the Universe*. Springer; 1 edition (October 31, 1989), 1989.
- [54] Darrick E. Chang, Anders S. Sørensen, Eugene A. Demler, and Mikhail D. Lukin. A single-photon transistor using nanoscale surface plasmons. *Nature Physics*, 3:807, 2007.

Bibliography

- [55] Hans J. Briegel and Robert Raussendorf. Persistent entanglement in arrays of interacting particles. *Phys. Rev. Lett.*, 86:910, 2001.
- [56] Stephen D. Bartlett and Terry Rudolph. Simple nearest-neighbor two-body hamiltonian system for which the ground state is a universal resource for quantum computation. *Phys. Rev. A*, 74:040302, 2006.
- [57] David Jennings, Andrzej Dragan, Sean D. Barrett, Stephen D. Bartlett, and Terry Rudolph. Quantum computation via measurements on the low-temperature state of a many-body system. *Phys. Rev. A*, 80:032328, 2009.
- [58] Michael A. Nielsen. Cluster-state quantum computation. *Rep. Math. Phys.*, 57:147, 2005.
- [59] Xie Chen, Bei Zeng, Zheng-Cheng Gu, Beni Yoshida, and Isaac L. Chuang. Gapped two-body hamiltonian whose unique ground state is universal for one-way quantum computation. *Phys. Rev. Lett.*, 102:220501, 2009.
- [60] Jianming Cai, Akimasa Miyake, Wolfgang Dür, and Hans J. Briegel. Universal quantum computer from a quantum magnet. *Phys. Rev. A*, 82:052309, 2010.
- [61] Ian Affleck, Tom Kennedy, Elliott H. Lieb, and Hal Tasaki. Rigorous results on valence-bond ground states in antiferromagnets. *Phys. Rev. Lett.*, 59:799, 1987.
- [62] Tzu-Chieh Wei, Ian Affleck, and Robert Raussendorf. Affleck-kennedy-lieb-tasaki state on a honeycomb lattice is a universal quantum computational resource. *Phys. Rev. Lett.*, 106:070501, 2011.
- [63] Akimasa Miyake. Quantum computational capability of a 2d valence bond solid phase. *Ann. Phys.*, 326:1656, 2011.
- [64] Leandro Aolita, Augusto J. Roncaglia, Alessandro Ferraro, and Antonio Acín. Gapped two-body hamiltonian for continuous-variable quantum computation. *Phys. Rev. Lett.*, 106:090501, 2011.
- [65] Gavin K. Brennen and Akimasa Miyake. Measurement-based quantum computer in the gapped ground state of a two-body hamiltonian. *Phys. Rev. Lett.*, 101:010502, 2008.
- [66] Maciej Lewenstein, Anna Sanpera, Veronica Ahufinger, Bogdan Damskic, Aditi Sen(De), and Ujjwal Sen. Ultracold atomic gases in optical lattices: mimicking condensed matter physics and beyond. *Adv. Phys.*, 56:243, 2007.
- [67] Immanuel Bloch, Jean Dalibard, and Wilhelm Zwerger. Many-body physics with ultracold gases. *Rev. Mod. Phys.*, 80:885, 2008.
- [68] L.-M. Duan, E. Demler, and M. D. Lukin. Controlling spin exchange interactions of ultracold atoms in optical lattices. *Phys. Rev. Lett.*, 91:090402, 2003.

-
- [69] A. Micheli, G. K. Brennen, and P. Zoller. A toolbox for lattice-spin models with polar molecules. *Nature Physics*, 2:341, 2006.
- [70] K. Kim, M.-S. Chang, S. Korenblit, R. Islam, E. E. Edwards, J. K. Freericks, G.-D. Lin, L.-M. Duan, and C. Monroe. Quantum simulation of frustrated ising spins with trapped ions. *Nature*, 465:590, 2010.
- [71] Julio T. Barreiro, Markus Müller, Philipp Schindler, Daniel Nigg, Thomas Monz, Michael Chwalla, Markus Hennrich, Christian F. Roos, Peter Zoller, and Rainer Blatt. An open-system quantum simulator with trapped ions. *Nature*, 470:486, 2011.
- [72] L. B. Ioffe, M. V. Feigel'man, A. Ioselevich, D. Ivanov, M. Troyer, and G. Blatter. Topologically protected quantum bits using josephson junction arrays. *Nature*, 415:503, 2002.
- [73] J.-M. Cai, W. Dür, M. Van den Nest, A. Miyake, and H. J. Briegel. Quantum computation in correlation space and extremal entanglement. *Phys. Rev. Lett.*, 103:050503, 2009.
- [74] Xie Chen, Runyao Duan, Zhengfeng Ji, and Bei Zeng. Quantum state reduction for universal measurement based computation. *Phys. Rev. Lett.*, 105:020502, 2010.
- [75] M. Hein, J. Eisert, and H. J. Briegel. Multiparty entanglement in graph states. *Phys. Rev. A*, 69:062311, 2004.
- [76] R. Raussendorf, J. Harrington, and K. Goyal. A fault-tolerant one-way quantum computer. *Ann. Phys.*, 321:2242, 2006.
- [77] Robert Raussendorf and Jim Harrington. Fault-tolerant quantum computation with high threshold in two dimensions. *Phys. Rev. Lett.*, 98:190504, 2007.
- [78] R. Raussendorf, J. Harrington, and K. Goyal. Topological fault-tolerance in cluster state quantum computation. *New J. Phys.*, 9:199, 2007.
- [79] Sean D. Barrett and Thomas M. Stace. Fault tolerant quantum computation with very high threshold for loss errors. *Phys. Rev. Lett.*, 105:200502, 2010.
- [80] Takuya Ohno, Gaku Arakawa, Ikuo Ichinose, and Tetsuo Matsui. Phase structure of the random-plaquette z_2 gauge model: accuracy threshold for a toric quantum memory. *Nucl. Phys. B*, 697:462, 2004.
- [81] Chenyang Wang, Jim Harrington, and John Preskill. Confinement-higgs transition in a disordered gauge theory and the accuracy threshold for quantum memory. *Annals of Physics*, 303:31, 2003.
- [82] Daniel Gottesman and Isaac L. Chuang. Demonstrating the viability of universal quantum computation using teleportation and single-qubit operations. *Nature*, 402:390, 1999.
- [83] Daniel E. Browne and Terry Rudolph. Resource-efficient linear optical quantum computation. *Phys. Rev. Lett.*, 95:010501, 2005.

Bibliography

- [84] F. Verstraete and J. I. Cirac. Valence-bond states for quantum computation. *Phys. Rev. A*, 70:060302, 2004.
- [85] Robert Raussendorf. Measurement-based quantum computation with cluster states. *IJQI*, 7:1053, 2009.
- [86] Michael A. Nielsen and Christopher M. Dawson. Fault-tolerant quantum computation with cluster states. *Phys. Rev. A*, 71:042323, 2005.
- [87] A. M. Stephens, A. G. Fowler, and L. C. L. Hollenberg. Universal fault tolerant quantum computation on bilinear nearest neighbor arrays. *Quantum Inf. Comput.*, 8:330, 2008.
- [88] T. M. Stace, S. D. Barrett, H-S. Goan, and G. J. Milburn. Parity measurement of one- and two-electron double well systems. *Phys. Rev. B*, 70:205342, 2004.
- [89] Avinash Kolli, Brendon W. Lovett, Simon C. Benjamin, and Thomas M. Stace. All-optical measurement-based quantum-information processing in quantum dots. *Phys. Rev. Lett.*, 97:250504, 2006.
- [90] C. Cabrillo, J. I. Cirac, P. García-Fernández, and P. Zoller. Creation of entangled states of distant atoms by interference. *Phys. Rev. A*, 59:1025, 1999.
- [91] S. Bose, P. L. Knight, M. B. Plenio, and V. Vedral. Proposal for teleportation of an atomic state via cavity decay. *Phys. Rev. Lett.*, 83:5158, 1999.
- [92] Sean D. Barrett and Pieter Kok. Efficient high-fidelity quantum computation using matter qubits and linear optics. *Phys. Rev. A*, 71:060310, 2005.
- [93] Yuan Liang Lim, Almut Beige, and Leong Chuan Kwek. Repeat-until-success linear optics distributed quantum computing. *Phys. Rev. Lett.*, 95:030505, 2005.
- [94] S. C. Benjamin, J. Eisert, and T. M. Stace. Optical generation of matter qubit graph states. *New J. Phys.*, 7:194, 2005.
- [95] C. W. Chou, H. de Riedmatten, D. Felinto, S. V. Polyakov, S. J. van Enk, and H. J. Kimble. Measurement-induced entanglement for excitation stored in remote atomic ensembles. *Nature*, 438:828, 2005.
- [96] D. L. Moehring, P. Maunz, S. Olmschenk, K. C. Younge, D. N. Matsukevich, L.-M. Duan, and C. Monroe. Entanglement of single-atom quantum bits at a distance. *Nature*, 449:68, 2007.
- [97] W. Dür and H.-J. Briegel. Entanglement purification for quantum computation. *Phys. Rev. Lett.*, 90:067901, 2003.
- [98] Simon C. Benjamin, Daniel E. Browne, Joe Fitzsimons, and John J. L. Morton. Brokered graph-state quantum computation. *New J. Phys.*, 8:141, 2006.

- [99] Simon Charles Benjamin. Comment on “efficient high-fidelity quantum computation using matter qubits and linear optics”. *Phys. Rev. A*, 72:056302, 2005.
- [100] Michael A. Nielsen. Optical quantum computation using cluster states. *Phys. Rev. Lett.*, 93:040503, 2004.
- [101] L.-M. Duan and R. Raussendorf. Efficient quantum computation with probabilistic quantum gates. *Phys. Rev. Lett.*, 95:080503, 2005.
- [102] Peter P. Rohde and Sean D. Barrett. Strategies for the preparation of large cluster states using non-deterministic gates. *New J. Phys.*, 9:198, 2007.
- [103] Yuichiro Matsuzaki, Simon C. Benjamin, and Joseph Fitzsimons. Probabilistic growth of large entangled states with low error accumulation. *Phys. Rev. Lett.*, 104:050501, 2010.
- [104] N. Yoran and B. Reznik. Deterministic linear optics quantum computation with single photon qubits. *Phys. Rev. Lett.*, 91:037903, 2003.
- [105] Thomas M. Stace, Sean D. Barrett, and Andrew C. Doherty. Thresholds for topological codes in the presence of loss. *Phys. Rev. Lett.*, 102:200501, 2009.
- [106] Thomas M. Stace and Sean D. Barrett. Error correction and degeneracy in surface codes suffering loss. *Phys. Rev. A*, 81:022317, 2010.
- [107] T. P. Bodiya and L.-M. Duan. Scalable generation of graph-state entanglement through realistic linear optics. *Phys. Rev. Lett.*, 97:143601, 2006.
- [108] J. Calsamiglia and N. Lütkenhaus. Maximum efficiency of a linear-optical bell-state analyzer. *Appl. Phys. B*, 72:67, 2001.
- [109] K. Kieling, T. Rudolph, and J. Eisert. Percolation, renormalization, and quantum computing with nondeterministic gates. *Phys. Rev. Lett.*, 99:130501, 2007.
- [110] Daniel E. Browne, Matthew B. Elliott, Steven T. Flammia, Seth T. Merkel, Akimasa Miyake, and Anthony J. Short. Phase transition of computational power in the resource states for one-way quantum computation. *New J. Phys.*, 10:023010, 2008.
- [111] Ying Li, Sean D. Barrett, Thomas M. Stace, and Simon C. Benjamin. Fault tolerant quantum computation with nondeterministic gates. *Phys. Rev. Lett.*, 105:250502, 2010.
- [112] A. H. Burrell, D. J. Szwer, S. C. Webster, and D. M. Lucas. Scalable simultaneous multiqubit readout with 99.99% single-shot fidelity. *Phys. Rev. A*, 81:040302, 2010.
- [113] Hannes Bernien, Lilian Childress, Lucio Robledo, Matthew Markham, Daniel Twitchen, and Ronald Hanson. Two-photon quantum interference from separate nitrogen vacancy centers in diamond. *Phys. Rev. Lett.*, 108:043604, 2012.

Bibliography

- [114] Keisuke Fujii, Haruki Maeda, and Katsuji Yamamoto. Robust and scalable scheme to generate large-scale entanglement webs. *Phys. Rev. A*, 83:050303, 2011.
- [115] Katherine L. Brown, Clare Horsman, Viv Kendon, and William J. Munro. Layer by layer generation of cluster states. arXiv:1111.1774, 2011.
- [116] Keisuke Fujii and Yuuki Tokunaga. Fault-tolerant topological one-way quantum computation with probabilistic two-qubit gates. *Phys. Rev. Lett.*, 105:250503, 2010.
- [117] Liang Jiang, Jacob M. Taylor, Anders S. Sørensen, and Mikhail D. Lukin. Distributed quantum computation based on small quantum registers. *Phys. Rev. A*, 76:062323, 2007.
- [118] Keisuke Fujii, Takashi Yamamoto, Masato Koashi, and Nobuyuki Imoto. A distributed architecture for scalable quantum computation with realistically noisy devices. arXiv:1202.6588, 2012.
- [119] J. Eisert, K. Jacobs, P. Papadopoulos, and M. B. Plenio. Optimal local implementation of nonlocal quantum gates. *Phys. Rev. A*, 62:052317, 2000.
- [120] Earl T. Campbell. Distributed quantum-information processing with minimal local resources. *Phys. Rev. A*, 76:040302, 2007.
- [121] John J. L. Morton, Alexei M. Tyryshkin, Richard M. Brown, Shyam Shankar, Brendon W. Lovett, Arzhang Ardavan, Thomas Schenkel, Eugene E. Haller, Joel W. Ager, and S. A. Lyon. Solid-state quantum memory using the 31p nuclear spin. *Nature*, 455:1085, 2008.
- [122] L. M. Duan, M. D. Lukin, J. I. Cirac, and P. Zoller. Long-distance quantum communication with atomic ensembles and linear optics. *Nature*, 414:413, 2001.
- [123] Christian D. Lorenz and Robert M. Ziff. Precise determination of the bond percolation thresholds and finite-size scaling corrections for the sc, fcc, and bcc lattices. *Phys. Rev. E*, 57:230, 1998.
- [124] F. Merz and J. T. Chalker. Two-dimensional random-bond ising model, free fermions, and the network model. *Phys. Rev. E*, 65:054425, 2002.
- [125] Nicolas Gisin and Rob Thew. Quantum communication. *Nature Photonics*, 1:165, 2007.
- [126] Charles H. Bennett, David P. DiVincenzo, John A. Smolin, and William K. Wootters. Mixed-state entanglement and quantum error correction. *Phys. Rev. A*, 54:3824, 1996.
- [127] A.Yu. Kitaev. Fault-tolerant quantum computation by anyons. *Ann. Phys.*, 303:2, 2003.
- [128] H. Bombin and Martin A. M. Delgado. Topological quantum distillation. *Phys. Rev. Lett.*, 97:180501, 2006.

- [129] H. Bombin and Martin A. M. Delgado. Topological computation without braiding. *Phys. Rev. Lett.*, 98:160502, 2007.
- [130] Austin G. Fowler, Ashley M. Stephens, and Peter Groszkowski. High-threshold universal quantum computation on the surface code. *Phys. Rev. A*, 80:052312, 2009.
- [131] Jian-Wei Pan, Dik Bouwmeester, Matthew Daniell, Harald Weinfurter, and Anton Zeilinger. Experimental test of quantum nonlocality in three-photon greenberger-horne-zeilinger entanglement. *Nature*, 403:515, 2000.
- [132] Zhi Zhao, Yu-Ao Chen, An-Ning Zhang, Tao Yang, Hans J. Briegel, and Jian-Wei Pan. Experimental demonstration of five-photon entanglement and open-destination teleportation. *Nature*, 430:54, 2004.
- [133] C. A. Sackett, D. Kielpinski, B. E. King, C. Langer, V. Meyer, C. J. Myatt, M. Rowe, Q. A. Turchette, W. M. Itano, D. J. Wineland, and C. Monroe. Experimental entanglement of four particles. *Nature*, 404:256, 2000.
- [134] Christian F. Roos, Mark Riebe, Hartmut Häffner, Wolfgang Hänsel, Jan Benhelm, Gavin P. T. Lancaster, Christoph Becher, Ferdinand Schmidt-Kaler, and Rainer Blatt. Control and measurement of three-qubit entangled states. *Science*, 304:1478, 2004.
- [135] D. Leibfried, E. Knill, S. Seidelin, J. Britton, R. B. Blakestad, J. Chiaverini, D. B. Hume, W. M. Itano, J. D. Jost, C. Langer, R. Ozeri, R. Reichle, and D. J. Wineland. Creation of a six-atom ‘schrodinger cat state’. *Nature*, 438:639, 2005.
- [136] Nikolai Kiesel, Christian Schmid, Ulrich Weber, Géza Tóth, Otfried Gühne, Rupert Ursin, and Harald Weinfurter. Experimental analysis of a four-qubit photon cluster state. *Phys. Rev. Lett.*, 95:210502, 2005.
- [137] P. Walther, K. J. Resch, T. Rudolph, E. Schenck, H. Weinfurter, V. Vedral, M. Aspelmeyer, and A. Zeilinger. Experimental one-way quantum computing. *Nature*, 434:169, 2005.
- [138] Chao-Yang Lu, Xiao-Qi Zhou, Otfried Gühne, Wei-Bo Gao, Jin Zhang, Zhen-Sheng Yuan, Alexander Goebel, Tao Yang, and Jian-Wei Pan. Experimental entanglement of six photons in graph states. *Nature Physics*, 3:91, 2007.
- [139] Kai Chen, Che-Ming Li, Qiang Zhang, Yu-Ao Chen, Alexander Goebel, Shuai Chen, Alois Mair, and Jian-Wei Pan. Experimental realization of one-way quantum computing with two-photon four-qubit cluster states. *Phys. Rev. Lett.*, 99:120503, 2007.
- [140] Robert Prevedel, Philip Walther, Felix Tiefenbacher, Pascal Böhi, Rainer Kaltenbaek, Thomas Jennewein, and Anton Zeilinger. High-speed linear optics quantum computing using active feed-forward. *Nature*, 445:65, 2007.

Bibliography

- [141] Giuseppe Vallone, Enrico Pomarico, Francesco De Martini, and Paolo Mataloni. Active one-way quantum computation with two-photon four-qubit cluster states. *Phys. Rev. Lett.*, 100:160502, 2008.
- [142] Raino Ceccarelli, Giuseppe Vallone, Francesco De Martini, Paolo Mataloni, and Adán Cabello. Experimental entanglement and non-locality of a two-photon six-qubit cluster state. *Phys. Rev. Lett.*, 103:160401, 2009.
- [143] S. Bose, V. Vedral, and P. L. Knight. Multiparticle generalization of entanglement swapping. *Phys. Rev. A*, 57:822, 1998.
- [144] Mark Hillery, Vladimír Bužek, and André Berthiaume. Quantum secret sharing. *Phys. Rev. A*, 59:1829, 1999.
- [145] Ellie D’Hondt and Prakash Panangaden. The computational power of the w and ghz states. *Journ. Quantum Inf. and Comp.*, 6:173, 2006.
- [146] Vittorio Giovannetti, Seth Lloyd, and Lorenzo Maccone. Quantum-enhanced measurements: Beating the standard quantum limit. *Science*, 306:1330, 2004.
- [147] J. J. Bollinger, Wayne M. Itano, and D. J. Wineland. Optimal frequency measurements with maximally correlated states. *Phys. Rev. A*, 54:4649, 1996.
- [148] E. Knill, R. Laflamme, and G. J. Milburn. A scheme for efficient quantum computation with linear optics. *Nature*, 409:46, 2001.
- [149] B. B. Blinov, D. L. Moehring, L.-M. Duan, and C. Monroe. Observation of entanglement between a single trapped atom and a single photon. *Nature*, 428:153, 2004.
- [150] Jürgen Volz, Markus Weber, Daniel Schlenk, Wenjamin Rosenfeld, Johannes Vrana, Karen Saucke, Christian Kurtsiefer, and Harald Weinfurter. Observation of entanglement of a single photon with a trapped atom. *Phys. Rev. Lett.*, 96:030404, 2006.
- [151] C. Schön, E. Solano, F. Verstraete, J. I. Cirac, and M. M. Wolf. Sequential generation of entangled multiqubit states. *Phys. Rev. Lett.*, 95:110503, 2005.
- [152] K. C. Wright, L. S. Leslie, and N. P. Bigelow. Raman coupling of zeeman sublevels in an alkali-metal bose-einstein condensate. *Phys. Rev. A*, 78:053412, 2008.
- [153] B. Darquié, M. P. A. Jones, J. Dingjan, J. Beugnon, S. Bergamini, Y. Sortais, G. Messin, A. Browaeys, and P. Grangier. Controlled single-photon emission from a single trapped two-level atom. *Science*, 309:454, 2005.
- [154] Tatjana Wilk. *Quantum Interface between an Atom and a Photon*. PhD thesis, TU München, 2008.

- [155] Netanel H. Lindner and Terry Rudolph. Proposal for pulsed on-demand sources of photonic cluster state strings. *Phys. Rev. Lett.*, 103:113602, 2009.
- [156] Michael Varnava, Daniel E. Browne, and Terry Rudolph. Loss tolerance in one-way quantum computation via counterfactual error correction. *Phys. Rev. Lett.*, 97:120501, 2006.
- [157] Otfried Gühne, Géza Tóth, Philipp Hyllus, and Hans J. Briegel. Bell inequalities for graph states. *Phys. Rev. Lett.*, 95:120405, 2005.
- [158] Nicolas Gisin, Grégoire Ribordy, Wolfgang Tittel, and Hugo Zbinden. Quantum cryptography. *Rev. Mod. Phys.*, 74:145, 2002.
- [159] H. J. Kimble. The quantum internet. *Nature*, 453:1023, 2008.
- [160] J. McKeever, A. Boca, A. D. Boozer, J. R. Buck, and H. J. Kimble. Experimental realization of a one-atom laser in the regime of strong coupling. *Nature*, 425:268, 2003.
- [161] T. Wilk, S. C. Webster, H. P. Specht, G. Rempe, and A. Kuhn. Polarization-controlled single photons. *Phys. Rev. Lett.*, 98:063601, 2007.
- [162] J. I. Cirac, P. Zoller, H. J. Kimble, and H. Mabuchi. Quantum state transfer and entanglement distribution among distant nodes in a quantum network. *Phys. Rev. Lett.*, 78:3221, 1997.
- [163] Ying Li, Leandro Aolita, and L. C. Kwek. Photonic multiqubit states from a single atom. *Phys. Rev. A*, 83:032313, 2011.
- [164] Janet Anders, Daniel K. L. Oi, Elham Kashefi, Dan E. Browne, and Erika Andersson. Ancilla-driven universal quantum computation. *Phys. Rev. A*, 82:020301, 2010.
- [165] Edo Waks and Jelena Vuckovic. Dipole induced transparency in drop-filter cavity-waveguide systems. *Phys. Rev. Lett.*, 96:153601, 2006.
- [166] Alexia Auffèves-Garnier, Christoph Simon, and Jean-Philippe Poizat Jean-Michel Gérard. Giant optical nonlinearity induced by a single two-level system interacting with a cavity in the purcell regime. *Phys. Rev. A*, 75:053823, 2007.
- [167] Cristian Bonato, Florian Haupt, Sumant S. R. Oemrawsingh, Jan Gudat, Dapeng Ding, Martin P. van Exter, and Dirk Bouwmeester. Cnot and bell-state analysis in the weak-coupling cavity qed regime. *Phys. Rev. Lett.*, 104:160503, 2010.
- [168] Kunihiro Kojima, Holger F. Hofmann, Shigeki Takeuchi, and Keiji Sasaki. Nonlinear interaction of two photons with a one-dimensional atom: Spatiotemporal quantum coherence in the emitted field. *Phys. Rev. A*, 68:013803, 2003.
- [169] J. T. Shen and Shanhui Fan. Coherent photon transport from spontaneous emission in one-dimensional waveguides. *Opt. Lett.*, 30:2001, 2005.

Bibliography

- [170] Caleb A. Christensen, Sebastian Will, Michele Saba, Gyu-Boong Jo, Yong-Il Shin, Wolfgang Ketterle, and David Pritchard. Trapping of ultracold atoms in a hollow-core photonic crystal fiber. *Phys. Rev. A*, 78:033429, 2008.
- [171] M. Bajcsy, S. Hofferberth, V. Balic, T. Peyronel, M. Hafezi, A. S. Zibrov, V. Vuletic, and M. D. Lukin. Efficient all-optical switching using slow light within a hollow fiber. *Phys. Rev. Lett.*, 102:203902, 2009.
- [172] G. Sagué, E. Vetsch, W. Alt, D. Meschede, and A. Rauschenbeutel. Cold-atom physics using ultrathin optical fibers: Light-induced dipole forces and surface interactions. *Phys. Rev. Lett.*, 99:163602, 2007.
- [173] E. Vetsch, D. Reitz, G. Sagué, R. Schmidt, S. T. Dawkins, and A. Rauschenbeutel. Optical interface created by laser-cooled atoms trapped in the evanescent field surrounding an optical nanofiber. *Phys. Rev. Lett.*, 104:203603, 2010.
- [174] Julien Claudon, Joël Bleuse, Nitin Singh Malik, Maela Bazin, Périne Jaffrennou, Niels Gregersen, Christophe Sauvan, Philippe Lalanne, and Jean-Michel Gérard. A highly efficient single-photon source based on a quantum dot in a photonic nanowire. *Nature Photonics*, 4:174, 2010.
- [175] T. Lund-Hansen, S. Stobbe, B. Julsgaard, H. Thyrrstrup, T. Süner, M. Kamp, A. Forchel, and P. Lodahl. Experimental realization of highly efficient broadband coupling of single quantum dots to a photonic crystal waveguide. *Phys. Rev. Lett.*, 101:113903, 2008.
- [176] Thomas M. Babinec, Birgit J. M. Hausmann, Mughees Khan, Yinan Zhang, Jeronimo R. Maze, Philip R. Hemmer, and Marko Lončar. A diamond nanowire single-photon source. *Nature Nanotechnology*, 5:195, 2010.
- [177] J. Brendel, N. Gisin, W. Tittel, and H. Zbinden. Pulsed energy-time entangled twin-photon source for quantum communication. *Phys. Rev. Lett.*, 82:2594, 1999.
- [178] Augusto J. Roncaglia, Leandro Aolita, Alessandro Ferraro, and Antonio Acín. Sequential measurement-based quantum computing with memories. *Phys. Rev. A*, 83:062332, 2011.
- [179] J. Berezovsky, M. H. Mikkelsen, N. G. Stoltz, L. A. Coldren, and D. D. Awschalom. Picosecond coherent optical manipulation of a single electron spin in a quantum dot. *Science*, 320:349, 2008.
- [180] J. R. Petta, A. C. Johnson, J. M. Taylor, E. A. Laird, A. Yacoby, M. D. Lukin, C. M. Marcus, M. P. Hanson, and A. C. Gossard. Coherent manipulation of coupled electron spins in semiconductor quantum dots. *Science*, 309:2180, 2005.
- [181] D. J. Reilly, J. M. Taylor, J. R. Petta, C. M. Marcus, M. P. Hanson, and A. C. Gossard. Suppressing spin qubit dephasing by nuclear state preparation. *Science*, 321:5890, 2008.

- [182] Gijs de Lange, Toeno van der Sar, Machiel Blok, Zhi-Hui Wang, Viatcheslav Dobrovitski, and Ronald Hanson. Controlling the quantum dynamics of a mesoscopic spin bath in diamond. *Science Reports*, 2:382, 2012.
- [183] D. Perez-Garcia, F. Verstraete, M.M. Wolf, and J.I. Cirac. Matrix product state representations. *Quantum Inf. Comput.*, 7:401, 2007.
- [184] David Deutsch, Artur Ekert, Richard Jozsa, Chiara Macchiavello, Sandu Popescu, and Anna Sanpera. Quantum privacy amplification and the security of quantum cryptography over noisy channels. *Phys. Rev. Lett.*, 77:2818, 1996.
- [185] H. Kim, R. Bose, T. C. Shen, G. S. Solomon, and E. Waks. A quantum logic gate between a solid-state quantum bit and a photon. *Nature Photonics*, 7:373, 2013.

Bibliography
